MSc Thesis

Morphodynamics of De Slufter

Morphodynamical processes in a small tidal inlet in the Netherlands

Stijn van Puijvelde

Supervisors:
- prof. dr. P. Hoekstra
- dr. M. van der Vegt

Department of Physical Geography
Faculty of Geosciences
Utrecht University
December 2009

Preface

This MSc thesis focuses on the morphodynamics of De Slufter, Texel. This thesis concludes the MSc *Physical Geography*; track *Coastal Dynamics and Fluvial Systems*, at the Faculty of Geosciences at Utrecht University. The MSc thesis is based on a combination of a desk study and a field campaign, executed in the autumn of 2008. This field work was carried out together with fellow students Ralf Klein Breteler and Wiebe Kramer. Each one focussed on a different aspect of the behaviour of De Slufter. Klein Breteler studied the influence of waves on sediment transport in the breaker zone and on the spit-like beach flat during storm events. Kramer concentrated on sediment transport patterns in the main tidal channel to distinguish between the impact of tide- and wave-driven processes on sediment transport.

Contents

List of figures

Figure 5.4: longitudinal profile of Slufter channel with mean low water on the North Sea. Maximum channel depths are plotted against distance starting at the most seaward part of the inlet towards the location of the main frame.

Figure 5.5: water levels at the North Sea and at the channel at the location of the main frame for neap tide (left) and spring tide conditions (right).

Figure 5.6: relation between surface area covered with water (m2) and water level (m +NAP) for De Slufter (hypsometric curve).

Figure 5.7: volume of water (m3) inside the system at different water levels (m +NAP).

Figure 5.8: rate of change in surface area covered by water and volume (for example: the values at 1.2 m indicate the percentual change from 1.1 m to 1.2 m +NAP).

Figure 5.9: hypsometric map of De Slufter with different colors indicating several stages of the flooding process and the relevant surface area covered by water at this particular stage.

Figure 5.10: Axy/Ac for different water levels.

Figure 5.11: hypsometric curves for three large tidal basins (Texel Inlet, Vlie Inlet and Ameland Inlet) of the Wadden Sea at different periods and for De Slufter (right, lower). Hypsometry of the Wadden basins after Dronkers (2005).

Figure 5.12: several parameters for neap tidal conditions including Ac (m2), Vb (m3), Hw (m NAP), dh/dt (m/s) and measured velocities (m/s).

Figure 5.13: several parameters for spring tidal conditions including Ac (m2), Vb (m3), Hw (m NAP), dh/dt (m/s) and measured velocities (m/s).

Figure 5.14: several parameters for storm conditions including Ac (m2), Vb (m3), Hw (m NAP), dh/dt (m/s) and measured velocities (m/s).

Figure 5.15: comparison between Hw and velocities (10 min. averages) at the channel (main frame) and at the beach flat for three tidal cycles during storm conditions.

Figure 5.16: bed load transport fraction f, where f is defined as the net bed load transport during each tidal cycle (ebb phase and subsequent flood phase) divided by the maximum value reached during this period (equation 5.2). f Is plotted against the maximum water level reached during the associated flood phase.

Figure 5.17: modeled and measured velocities during neap tidal conditions.

Figure 5.18: modeled and measured velocities during spring tidal conditions.

Figure 5.19: modeled and measured velocities during storm conditions.

Figure 6.1: relation between tidal prism and cross-sectional area for De Slufter against UK, US, New Zealand, and Dutch data (after Townend, 2005).

Figure 6.2: relation between tidal prism and cross-sectional area during MSL for De Slufter against data from stable inlets of van der Kreeke (1990) and Lam (2003).

Figure 6.3: Cross-sectional areas of the inlet of De Slufter from the dd-profile, for 29-09 (pre-storm), 02-10 (between two storms) and 11-10 (post-storm) at different water levels.

Figure 6.4: wave angle (degrees), offshore significant wave height Hs (cm) and water level above NAP in the channel (cm) plotted against time during the two storm periods.

Figure 6.5: maximum water levels reached during all the tidal cycles of a period before the storm (day 262-275) and a period after the storm (day 285-291) plotted against maximum velocities reached during the associated tidal cycle (both maximum ebb- and flood-velocities). Ebb-velocities are negative. The figure also includes linear regression lines for both pre-storm and post-storm maximum velocities.

Figure 6.6: panorama of the Slufter channel showing its flow path. The channel reaches the sea in the far right of the picture. The water flows nearly parallel to the coast line for a distance of several hundreds of metres.

Figure 6.7: cliffs on 01/10 formed during the first storm-event at the eastern channel side.

Figure 6.8: percentage of water transport plotted against the water level. Until a water level of 1.35 m +NAP most water is transported through the channel, while at the higher water levels, the beach flat becomes the most important area over which transport takes place.

Figure 6.9: simplified example of a real morphology and a TIN model.

Figure 6.10: profiles for both the DGPS measurements and the TIN model, showing a large correspondence, with distance ranging from 0m at the dunes south of the Slufter mouth to 600m at at the dunes north of the mouth.

Figure 6.11: longitudinal profile of the deepest part of the channel of the DEM in metres. Transition from DGPS to LiDAR measurements occurs near point 80. LiDAR underestimates bed height by up to 60 cm.

List of tables

Summary

De Slufter is a small tidal inlet located on Texel, The Netherlands. From 8 September to 17 October 2008, a field work was carried out in De Slufter measuring the morphological development of the mouth area and water levels and flow velocities in the main channel. The aim of this report is to study the interaction between basin morphology and the hydrodynamics of the system and its implications for the long term stability and evolution of De Slufter. In a stable inlet there is a balance between the import of sediment during the flood phase and the export of sediment during the ebb phase, by which the inlet remains connected to the sea. The tide is however deformed when it enters the inlet. The most important mechanisms causing this deformation include tidal truncation and a hypsometry effect. Tidal deformation results in duration asymmetries, causing differences in peak flood- and ebb-velocities. A deformed velocity signal leads to a net sediment transport. This determines the stability of the inlet. Not much is known about the stability of small tidal inlets. This is related to the distinct morphology of De Slufter, with its small amount of intertidal flats and large surface area between 1.1-1.5 m +NAP.

Analyzing yearly aerial photographs, a channel migration cycle of 3-7 years is observed in the mouth area. Migration occurs from the southwest to the northeast and the channel curvature increases at the end of the cycle. The cycle ends with channel relocation by man. During the initial calm weather period of the field campaign, no channel migration was observed. During the two storm events a channel migration was observed in the most seaward section of the channel. The narrowest section of the channel migrated approximately 10 metres. The curvature of the channel also increased and the channel slightly changed its orientation. Most channel profiles reveal a storm-induced widening of the channel. This resulted in an increase of the cross-sectional area up to 22.1% in the seaward section of the channel. This enlargement was accompanied by slightly lower peak ebb- and flood-velocities. During fair weather conditions in the final phase of the field work, equilibrium was partly restored by decreasing the cross section again. Migration of the channel is possibly related to the combined effect of wave-impact, the longshore current and a circulation pattern developing during storms. This circulation imports water over the beach flat, due to submergence and overwash, and exports it again through the channel. The accretion on the beach flat and retreat of the beach face as a result of storm-conditions are probably related to the same circulation pattern. The storm events enlarged inlet cross sections.

During fair weather conditions a large tidal deformation was measured in De Slufter. The amplitudes of M_2 and M_4 and the M_4/M_2-ratio all decreased compared to the North Sea. A phase relationship $(2M_2-M_4)_{sea}$ of 270-360 degrees was measured, indicating a longer ebb

than flood duration. Compared to the North Sea (where the tide is already slightly deformed) ebb-duration in De Slufter increases with 53.5 minutes. This asymmetry is caused by a truncation of the tide. The channel bed has an elevation of -0.5 m NAP at the mouth, while the mean low water is -0.89m NAP. This indicates that most of the times during ebb, drainage still occurs while the tide at the North Sea already starts to rise. Tidal asymmetry is further caused by the hypsometry of the basin. At water levels over 1.1 m +NAP, the surface area covered with water increases rapidly. This mechanism causes large differences between normal and storm conditions. During normal conditions water is confined to the channel. The wet surface area (A_{xy}) increases proportional with the cross-sectional area (A_c). Peak flood velocities are slightly larger than peak ebb velocities. Differences in ebb- and flood-velocities are very small. During storm events A_{xy} increases much faster than A_c. Peak ebb velocities are twice as large as peak flood velocities. Based on the measured velocity signal, the net bed load transport appears to occur in the ebb-direction. The net suspended load transport occurs in the flood-direction, because the duration of the high water slack is much larger than the duration of the low water slack. A simple model was used to simulate flow velocities. The order of magnitude and phases of the simulated velocities agree with measurements, but deviations arise due to inaccuracy of the measurements and over-simplicity of the model. Flood velocities during normal conditions are overestimated, while ebb velocities during storm conditions are underestimated.

Based on modeled bed load transport ratios and slack durations, the system appears to be ebb-dominant, both during normal and storm conditions. The system appears to be in equilibrium. This also follows from the fact that the system already exists for 150 years and from several (semi)-empirical relationships derived for stable inlets all over the world. The present configuration of De Slufter in its stable situation is however artificially maintained, because the channel is relocated every 3-7 years.

1. Introduction

1.1 Problem definition

De Slufter, located at the North Sea coast of Texel, The Netherlands, is a small tidal inlet system. Its total surface area comprises more than 400ha, with artificial dikes at the landward boundary (figure 1.1). Slufter systems are characterized by:

- A channel connecting a small tidal basin with the open sea. Water is imported into the basin during flood and exported again during the ebb phase.
- In the tidal basin several tidal creeks dissect a salt marsh, which is generally located at a much higher level compared with the channel bottoms. Therefore the salt marshes are only flooded during storm conditions.
- The amount of intertidal areas covering the basins of slufter systems is commonly small compared to larger tidal basins. In the large Wadden Sea tidal basins extensive areas exist that are flooded during the flood stage and emerge again during the ebb stage.
- Slufter systems have much smaller dimensions compared with larger tidal basins. The large basins of the western Wadden Sea have an average surface area of $6.7 \cdot 10^4$ ha. Whereas the Slufter inlet channel has a width of approximately 30/35 m, the inlets of the western Wadden Sea have widths ranging between 2.0 and 2.5 km. Tidal prisms of slufters are much smaller.

Besides De Slufter the only other slufter system in The Netherlands that satisfies the characteristics mentioned above is Het Zwin (Zeeland). Other systems like De Zwarte Polder have a comparable morphology and ecology but are not (partly) flooded every tidal cycle.

The Slufter mouth is a very dynamic area. Even during the six weeks of the field campaign large changes in morphology were observed. The tidal basin with its salt marshes is much less dynamic, because it is only flooded during storm conditions and wave influence is very small here.

A lot of research is done about large tidal basins and the mechanisms that determine the stability of the associated tidal inlets. Several stability relationships have been derived for these large systems (Escoffier, 1940; Bruun and Gerritsen, 1960; O'Brien, 1969; Van de Kreeke, 1985), where cross sectional area is related to the mean tidal prism. Similar mechanisms play a role in smaller scale systems, but the stability principles mentioned above are probably not applicable for slufter systems, since these theories predict a closure of the inlet, whereas De Slufter already exists since its formation in 1858. Not very much is known about the mechanisms determining the stability and evolution of small tidal inlets. A general understanding is lacking. This is probably related to the distinct morphology of the De Slufter. De Slufter has a very large surface area elevated between 1.0 and 1.5 m +NAP.

This results in a rapid increase of the wet surface area and water volume during storm surges. This makes De Slufter unique. The main aim of this thesis is to determine the interaction between basin morphology and the hydrodynamics of De Slufter and its implications for the evolution and long term stability of the system.
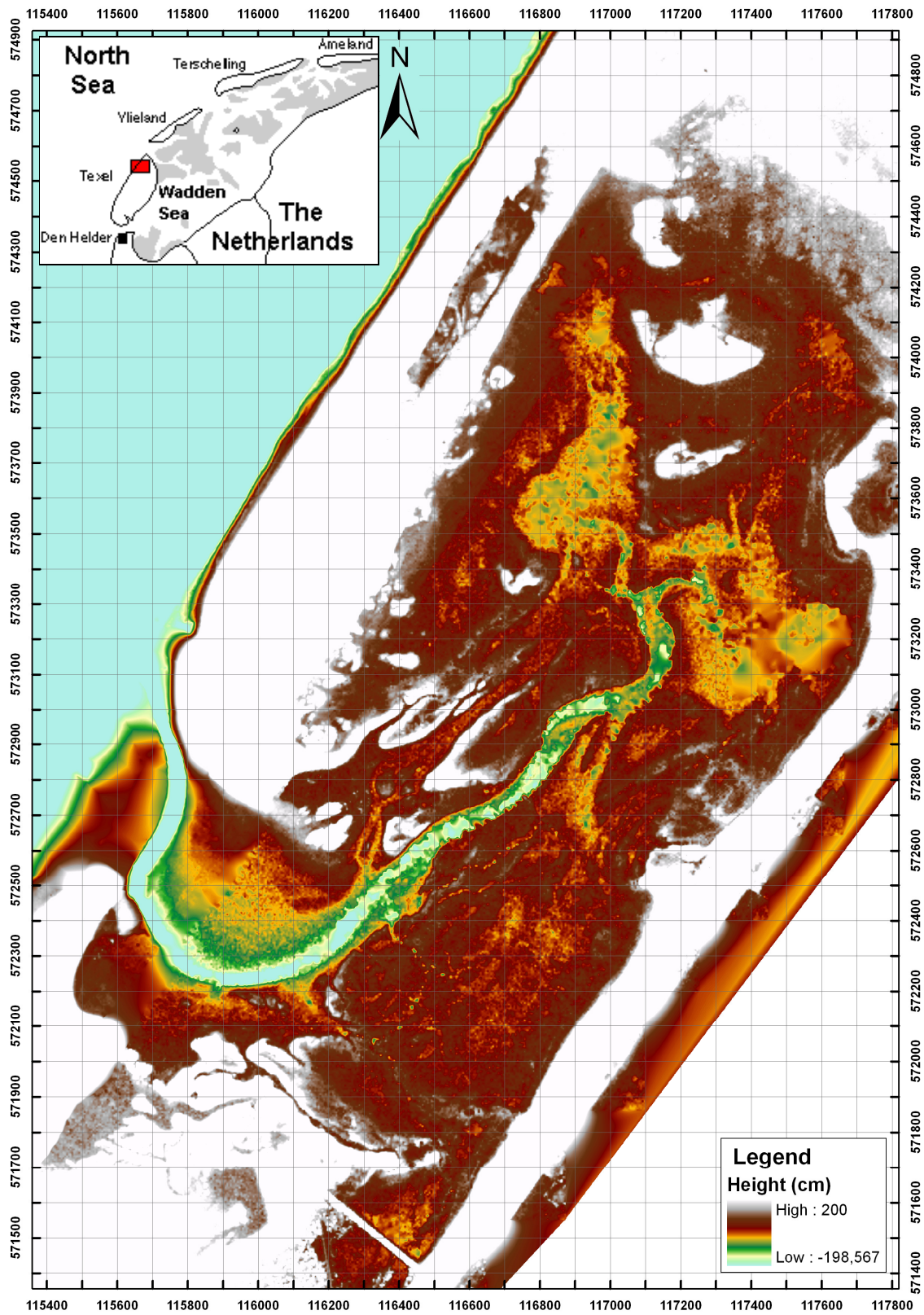
Figure 1.1: morphology of the De Slufter, located in the north of Texel, the Netherlands with a height range from -2 to 2m NAP. Locations with elevations over +2m NAP are indicated in white and under -2m NAP in light blue. The location of De Slufter on the island of Texel is indicated in the small map above (red square).

1.2 Inlet stability

1.2.1 Geological approach

Tidal inlets form when weak parts of a barrier breach during a storm event. De Slufter originated during such a breach in 1858. A narrow channel forms, importing and exporting water during a tidal cycle. Eysink (1993) recognized several factors influencing the large-scale development of tidal basins on longer time scales. These factors include the tidal range, the wave climate and a relative sea level rise. Hayes (1979) classified the tidal range and wave climate in order to study its relative influence on basin morphology. The classification ranges from tide-dominated (high) coasts to tide-dominated (low), mixed-energy (tide-dominated), mixed energy (wave-dominated) and wave-dominated coasts. Wave-dominated barrier islands are generally elongated, while mixed energy barrier islands are shorter. They are often characterized by a "drumstick"-like shape. Barrier islands do not form at tide-dominated coastal areas. The "mixed energy (tide-dominated)" class is seen as the upper limit of barrier islands to develop.

During normal conditions the influence of waves on the morphology of tidal basins is generally restricted to the inlet area. Only during storm conditions, a limited amount of waves can penetrate into the basin. Waves generated inside the basin play however a more important role in influencing the morphology of the basin, but because of the limited size of the basin this effect will still be insignificant.

Sea level rise can influence the evolution of tidal basins. Equilibrium is reached when sea level rise is compensated by sediment accumulation. When the rate of sea level rise increases and this is accompanied by an increase of the tidal prism, the system will become out of equilibrium. Water depths in the tidal basin and discharges through the inlet increase. The increased water depths lead to slightly lower current velocities. As will be explained later on in paragraph 1.2.3 sediment transport is very sensitive for changes in flow velocities. This will cause a significant decrease of the sediment transport capacity, stimulating the accumulation of sediment inside the basin. The system tries to restore its dynamic equilibrium. However when the sea level rise is too fast for accumulation to keep pace and a certain threshold value is exceeded, equilibrium can not be reached. The tidal basin will drown (figure 1.2; van Goor et al., 2001).
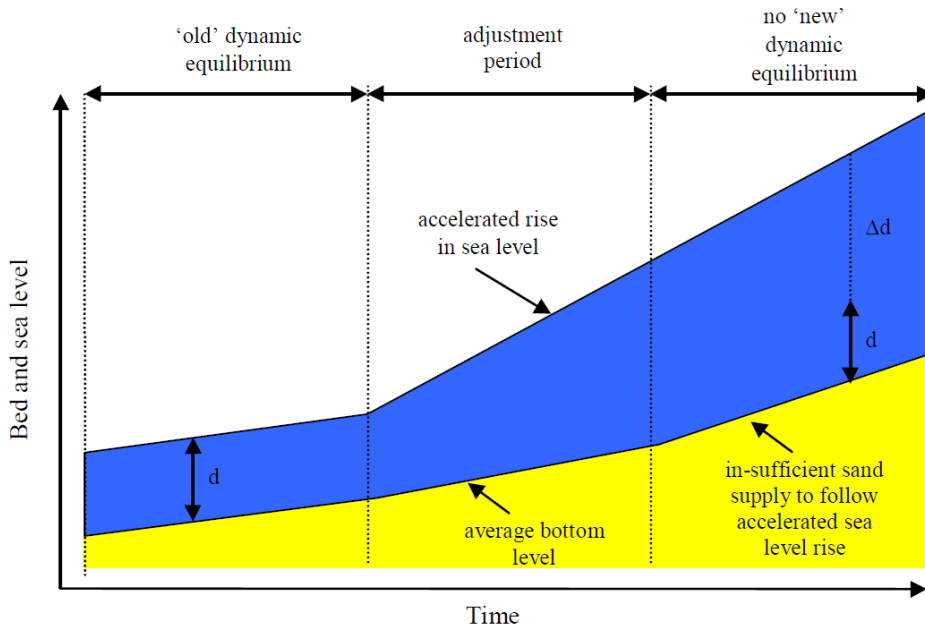
Figure 1.2: sea level rise is too fast for sediment accumulation to keep pace. No 'new' dynamic equilibrium is reached. From van Goor et al. (2001).

1.2.2 Empirical approaches

Several empirical relations were developed to define the stability of tidal inlet systems. Below the most important relations are discussed.

Longshore drift vs. tidal prism

Bruun and Gerritsen (1960) introduced a concept of inlet stability in terms of the rate of change in geomorphological characteristics in response to hydrodynamic and sediment dynamical conditions. They related inlet stability to two empirical criteria. The first one is the ratio Ω/M, where Ω is the tidal prism per spring tidal cycle, defined as the difference between the high and low water volumes inside the basin and M is the sediment transported into the inlet due to longshore drift (Gao and Collins, 1994b). The larger this ratio, the more stable the inlet is. Inlets with Ω/M ratios larger than 300, have a high degree of stability. A larger ratio indicates a dominant tidal influence compared to wave-induced sediment transport. Values smaller than 100 indicates the inlet is rather unstable. It must however be noted that this theory does not take into account some other processes influencing inlet stability, including for example cross-shore transport and tidal asymmetry. Besides, their definition of stability is related to ebb-shoal bar formation. "Good stability" indicates little offshore bar formation, while unstable inlets are characterized by the absence of a "permanent" channel. According to this definition inlets can be defined as "unstable" even when normal water exchange takes place by overflow across a bar system or when a channel shows a seasonal behaviour (Truitt, 1992). The second criterion used by Bruun and Gerritsen (1960) is $V_{mean(max)}$, defined

as the maximum of the cross-sectional mean velocity. According to them $V_{mean(max)}$ approaches 1 m/s for stable inlets. Gao and Collins (1994a) however showed this is inconsistent. Stability is not necessarily associated with a particular current speed.

Inlet cross-section vs. tidal prism

Several attempts were made to relate the cross-sectional area of inlets (A_E) to the tidal prism. Most of these relations are (semi)empirical. To a large degree these relations are separated from each other by differences in wave influence. O'Brien (1969) found a good linear relation between $Log_{10}A$ and $Log_{10}P$, where P is the spring tidal prism. This relationship represents equilibrium conditions when:

$$A_E = CP^q \tag{1.1}$$

where C and q are constants which can be determined from a regression analysis. The simplicity of this approach made it was used widely. The relation however shows significant scatter.

Townend (2005) put together data from studies covering estuaries and inlets in the US, the UK, New Zealand and the Netherlands (figure 1.3). Three groups were recognized with a different geomorphology, all having their characteristic values for the empirical constants C and q. This partly explains the appearance of scatter. Townend (2005) concluded that only the inlets, estuaries and rivers that have filled with sediment during the Holocene (group C; lower regression line, HH-C, in figure 1.3) are in dynamic equilibrium.
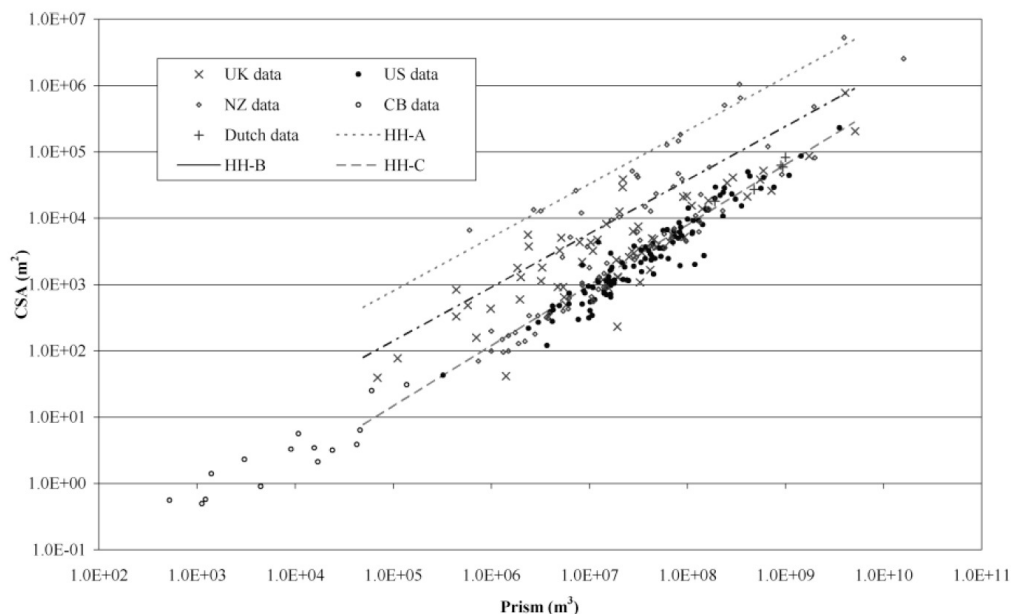
Figure 1.3: relation between tidal prism and cross-sectional area for UK, US, New Zealand, and Dutch data, including regression lines HH-A, HH-B and HH-C indicating the three estuary types, further clarified in Townend (2005).

Gao and Collins (1994 a,b) further elaborated the approach of O'Brien (1969) and analyzed additional factors and parameters determining equilibrium of tidal inlets to explain the scatter of equation 1.1. They suggested that inlet equilibrium A_E is not only related to the mean tidal prism, as was proposed by O'Brien (1969), but also to additional factors including current speeds during flood and ebb, flood and ebb durations, intensity of the longshore drift, sediment characteristics influencing sediment transport rates, width of the channel and the ratio between the transport capacity within the entrance to longshore sediment discharge (Gao and Collins, 1994 a,b).

Empirical relationships have proven to be useful in estimating equilibrium conditions. They can give an overview of what conditions can be expected, based on data of tidal basins of different scales. However they fail to give insight in the basic mechanisms that play a role in determining inlet stability. The studies of Gao and Collins (1994 a,b) proved that a more physical based approach is needed to fully understand the processes that determine inlet stability.

1.2.3 Physical based approach

Escoffier Closure Curve

Escoffier (1940) was the first to propose an analytical approach to inlet stability. He related inlet stability to a dynamic equilibrium state of the cross-sectional area. The strength of the inlet currents, together with the wave climate, determines the ultimate cross section of the inlet. As these two factors vary substantially over time, the inlet continuously adjusts itself to changing conditions (Van de Kreeke, 1985). The inlet flow velocities on its turn are largely dependant upon the tidal prism of a basin. The key assumption of Escoffier's approach is that when the inlet is in equilibrium, the maximum bottom shear stress during a tidal cycle $\hat{\tau}$ equals the equilibrium shear stress $\hat{\tau}_{eq}$. The tidal currents are just strong enough to remove the sediment that was deposited in the inlet by the wave-induced longshore current. The value for $\hat{\tau}_{eq}$ differs for each system, depending on the amount of sediment transported into the inlet, the wave climate, the tidal period and the sediment characteristics. Bruun (1978) found this value ranging between 3.5-5.5 N/m^2. The maximum shear stress is a function of the cross-sectional area A. This relation is defined as the 'closure curve'. The general shape of this curve is plotted in figure 1.4 and is also referred to as the Escoffier diagram.

The horizontal line corresponds to the equilibrium situation when $\hat{\tau} = \hat{\tau}_{eq}$. The curve can explain the response of the cross-sectional area to changes in hydraulic conditions. The cross-sectional areas A_1 and A_2 are equilibrium flow areas. At these values for A, the

maximum shear stress is just able to remove the amount of sediment deposited in the inlet. When A is larger than A_2, the shear stress is smaller than $\hat{\tau}_{eq}$. The tidal currents will not be able to erode all the sediment deposited in the inlet. Consequently, the cross-sectional area reduces towards A_2. When $A_1 < A < A_2$, the shear stress is larger than $\hat{\tau}_{eq}$. This will increase the cross-sectional area until it reaches A_2. When A is smaller than A_1, the shear stress falls below the equilibrium shear stress. Friction becomes increasingly dominant, resulting in a decrease of the cross-sectional area and finally the closure of the inlet (Van de Kreeke, 1985; Van de Kreeke, 1992). The behaviour of cross-sectional adjustment of tidal inlets becomes obvious looking at the seasonal variations (figure 1.4; right). For example, when due to a storm the cross-sectional area suddenly increases (figure 1.4; right; point B), the cross-section eventually returns to its equilibrium flow area (dashed line) (Van de Kreeke, 1985).
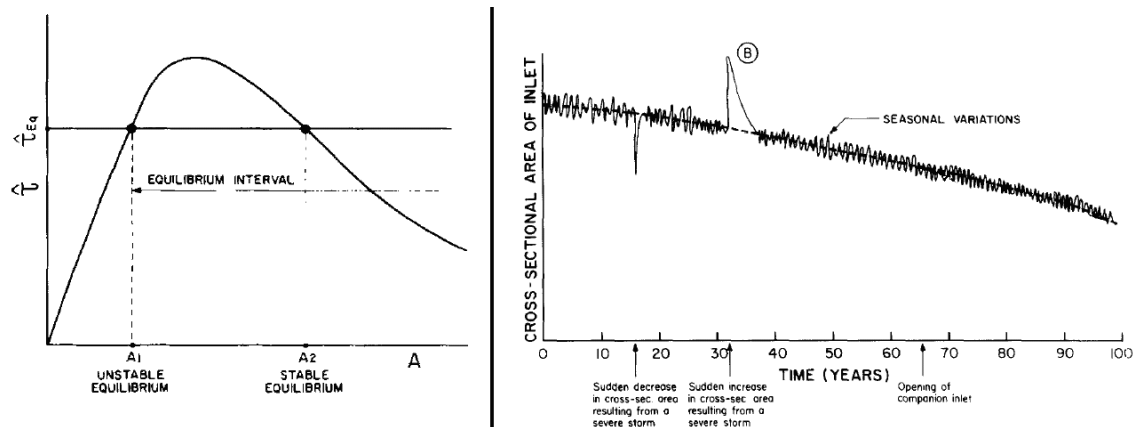
Figure 1.4: left: general shape of the closure curve, with bottom shear stress plotted against cross-sectional area. From Van de Kreeke (1985) after Escoffier (1940). Right: Evolution of cross-sectional area with time and changes in inlet cross-sectional areas due to seasonal variations. After Van de Kreeke (1985).

Escoffier's method still has an empirical background. Van de Kreeke (2006) and de Swart and Zimmerman (2009) elaborated Escoffier's theory and combined it with basic physics to construct (semi-empirical) models, describing the development of the cross-sectional area of inlets with time. Van de Kreeke (2006) found for inlets in equilibrium that:

$$A_c = A_{eq} \tag{1.2}$$

where

$$A_{eq} = CP^q \ , \ C = \left(\frac{MT^n}{k\alpha^m \pi^n} \right)^{\left(\frac{2}{m-2n} \right)} \quad \text{and} \quad q = \frac{n}{n-m/2}$$

M   = volume of sand entering the inlet during flood
T   = tidal period
α   = value depending on the shape of the cross-section

17

k   = constant depending on the sand characteristics
m,n   = values depending on sand transport law

Values for C and q are more or less similar for inlets with identical conditions. Theoretical values for q are comparable with values for q found with empirical relationships (equation 1.1).

1.2.4 Process-based approach

Stability is determined by the exchange of sediment between the basin and the sea. The flood currents import sediment into the basin while ebb currents again export it back in the seaward direction (van de Kreeke, 2006). Deformation of the tidal signal may disturb the balance between import and export in the inlet.

Tidal deformation

The tidal spectrum is composed of a finite set of sinusoids. The dominant tidal constituent at the North Sea and the coast of Texel is M_2. Distortion of the tide occurs during its propagation from deep water into shallow inlet systems. Higher harmonics ("overtides") are produced, with M_4 as the most important constituent. Non-linear distortion can be quantified directly by the M_2/M_4 sea-surface (equation 1.3) and velocity (equation 1.4) ratios:

$$\left(M_4 / M_2\right)_{sea} = a_{M_4} / a_{M_2} \tag{1.3}$$

$$\left(M_4 / M_2\right)_{vel} = v_{M_4} / v_{M_2} \tag{1.4}$$

a   = amplitude of tidal height
v   = amplitude of velocity

The larger the ratio of M_4/M_2 the larger the distortion. The sea surface phase (equation 1.5) and the velocity phase (equation 1.6) of M_4 relative to M_2 are respectively:

$$\left(2M_2 - M_4\right)_{sea} = 2\theta_{M_2} - \theta_{M_4} \tag{1.5}$$

$$\left(2M_2 - M_4\right)_{vel} = 2\varphi_{M_2} - \varphi_{M_4} \tag{1.6}$$

θ   = phase of tidal height
φ   = phase of velocity

The water level (z) can be approximated by:

$$z(t) = z_0 + z_{M_2} \sin(\sigma_{M_2} t - \theta_{M_2}) + z_{M_4} \sin\left(2\sigma_{M_2} t - \theta_{M_4}\right) \tag{1.7}$$

Because De Slufter basin is very limited in size we can assume the tidal wave behaves as a standing wave. Water levels are uniform throughout the basin and u ~ dz/dt. Therefore velocity (u) can be derived from equation 1.7:

$$u(t) \approx z_{M_2}\sigma\cos(\sigma_{M_2}t - \varphi_{M_2}) + z_{M_4}2\sigma\cos(2\sigma t - \varphi_{M_4}) \qquad (1.8)$$

This can again be rewritten into:

$$u(t) = u_0 + u_{M_2}\cos(\sigma_{M_2}t) + u_{M_4}\cos\!\left(2\sigma_{M_2}t + \left(2M_2 - M_4\right)_{vel}\right) \qquad (1.9)$$

u_0 = residual velocity
σ_{M2} = angular frequency M_2 tidal current
u_{M2} = amplitude of the M_2 tidal current
u_{M4} = amplitude of the M_4 tidal current

Distortion creates a phase lag between the M_4 and M_2 components. Phase relationships reflect whether systems have a duration asymmetry. It follows from equations 1.7-1.9 that for both relative phases $(2M_2$-$M_4)_{sea}$ and $(2M_2$-$M_4)_{vel}$ the duration of the falling tide exceeds the duration of flood between -90° and 90°. A relative phase between between 90° and 270° points to a larger duration of the flood phase compared with the ebb phase (Friedrichs and Aubrey, 1988).

Duration asymmetry can be expressed as:

$$D = \left[\left(d_{rise} - d_{fall}\right)/\left(d_{rise} + d_{fall}\right)\right]*100 \qquad (1.10)$$

d_{rise} = duration of the rising tide
d_{fall} = duration of the falling tide

A duration difference between the ebb and flood phases leads to a difference in maximum ebb and flood velocities. In case of a positive (negative) duration asymmetry, peak ebb (flood) velocities will exceed peak flood (ebb) velocities. This will have large consequences for the sediment transport pattern, resulting in either import or export of sediment. Depending on the particle size of the sediment and flow conditions, tidal dominance can be separated into dominance regarding bedload transport and dominance regarding suspended load transport. Different mechanisms play a role in these separate modes of transport.

Sediment transport

Bedload transport is usually defined as the sediment fraction transported by sliding, saltation and rolling. The finer fraction of the sediment is transported as suspended load. Bailard (1981, 1985) extended Bagnold's (1966) energetics based approach for sediment transport. This approach assumes that the work done in transporting sediment is a fixed proportion of the total energy dissipated by the flow (Bayram et al., 2001). Bailard's formula calculates the total sediment transport (q_t) for the combined effect of waves and currents under a sloping bottom:

$$\langle q_t \rangle = \langle q_b \rangle + \langle q_s \rangle \tag{1.11}$$

Where the instantaneous bed load (q'_b) and suspended load (q'_s) are defined as:

$$q'_b = \frac{0.5 f_w \rho e_b}{(\rho_s - \rho) g \tan \sigma} \left[|U'_t|^2 U'_t - \frac{\tan \beta}{\tan \sigma} |U'_t|^3 i\beta \right] \tag{1.12}$$

$$q'_s = \frac{0.5 f_w \rho e_s}{(\rho_s - \rho) g w} \left[|U'_t|^3 U'_t - \frac{e_s}{w} \tan \beta |U'_t|^5 i\beta \right] \tag{1.13}$$

f_w	= wave friction factor
ρ	= the density of water
ρ_s	= the density of the bed material
e_s, e_b	= efficiency factors
g	= gravitational acceleration
$\tan \sigma$	= dynamic friction factor
U'_t	= instantaneous velocity vector near the bed
$\tan \beta$	= local bottom slope
$i\beta$	= unit vector in direction of the slope
w	= sediment fall velocity

Tidal deformation and bed load transport

Asymmetry of the tidal signal will result in a tidally averaged net bed load transport. When M_4 is the most important overtide created, the bed load transport depends on the amplitudes of u_{M2} and u_{M4} and the relative phase $2M_2$-M_4. When flow velocity is approximated by equation 1.9, the bed load (q_b) averaged over a tidal cycle becomes:

$$\frac{<q_b>}{f} = u_{M_2}^2 u_0 + \frac{1}{2} u_{M_2}^2 u_{M_4} \cos(2M_2 - M_4)_{vel} \tag{1.14}$$

where f is a function of sediment and fluid characteristics defined by van de Kreeke and Robaczewska (1993) as:

$$f = \frac{\rho}{(\rho_s - \rho) g} \frac{e_b}{(\tan \phi - \tan \theta)} F \tag{1.15}$$

ρ	= density of water
ρ_s	= density of sediment
e_b	= efficiency factor (≈ 0.1)
θ	= local bed slope
ϕ	= angle of repose of bed material
F	= friction factor

It follows from equation 1.14 that there is no net bed load transport (q_b) when the relative phases is 90° or 270° and when the first term $(u_{M_2}^2 u_0)$ is zero. Net transport occurs in

the ebb direction for a relative phase between 90°-(180°)-270°. In this case the flood duration exceeds that of the ebb phase, resulting in larger peak ebb velocities compared to peak flood velocities. The system is regarded as ebb dominant, in terms of bed load transport. Net bed load transport occurs in the flood direction with a phase between 270°-(0°)-90° when ebb duration exceeds flood duration. Maximum ebb velocities will be smaller than maximum flood velocities. The bed load transport is flood dominant.

Tidal deformation and suspended load transport

de Swart and Zimmerman (2009) used another approach to describe the suspended load transport (q_s):

$$q_s = uC \tag{1.16}$$

u   = velocity

Where the depth-integrated concentration (C) is calculated with:

$$\frac{\partial C}{\partial t} = \alpha u^2 - \gamma C \tag{1.17}$$

α   = erosion coefficient
γ   = deposition coefficient

The first term on the right hand side of equation 1.17 describes erosion and the second term deposition. When the velocity is again approximated by equation 1.9, the net sediment transport becomes:

$$< q_s > = \frac{\alpha}{\gamma} \left\{ \frac{1}{4} u_2^2 u_4 \cos(2\varphi_{M_2} - \varphi_{M_4}) \left[\frac{2}{1+a^2} + \frac{1}{1+4a^2} \right] \right\}$$
$$- \frac{\alpha}{\gamma} \left\{ \frac{1}{2} a u_2^2 u_4 \sin(2\varphi_{M_2} - \varphi_{M_4}) \left[\frac{1}{1+a^2} - \frac{1}{1+4a^2} \right] \right\} \quad \text{for } u_0 = 0 \tag{1.18}$$

Where a is the settling lag parameter defined as the ratio of the principal tidal period divided by time that particles need to settle: $a = \omega / \gamma$.

It follows from equation 1.18 that maximum transport occurs at $\sin(2\varphi_{M_2} - \varphi_{M_4}) = \pm 1$ (for a > 1). When this term is equal to (-)1, the (ebb) flood slack has its maximum duration. When a slack tide has a longer duration, more suspended particles are able to settle. Therefore flood dominant systems, in terms of suspended sediment transport, are

characterized by a high water slack (HWS) of a longer duration compared to that of the low water slack (LWS). Ebb dominant systems have a longer LWS duration.

Settling lag effect and scour lag effect

A residual transport of suspended material can also occur without any tidal asymmetry, due to the "settling lag" effect. This effect is related to the inertia of the motion of sediment. Around slack water, sediment settles down, but because this settling takes time, sediment is consequently transported beyond the point where flow falls below its transport capacity (Van Straaten and Kuenen, 1957). Postma (1954) explained the influence of a settling lag effect on the transport of suspended sediment in the Wadden Sea. The inward net transport is related to the combining effect of the attenuation of the tidal current amplitude and the time lag between variations in concentrations of suspended sediment with respect to the strength of the tidal current. During the ebb phase, higher velocities are required for erosion of material from the bottom, than the velocities at which settling had occurred during the previous flood phase. This is caused by the difference between the critical shear stress at which sedimentation stops τ_{cr-s} and the critical shear stress at which erosion starts τ_{cr-e}. τ_{cr-s} is generally lower than τ_{cr-e}. This is called the "scour lag" effect and results in a landward transport of suspended sediment (Van Straaten and Kuenen, 1957).

Tidal deformation in small tidal basins

The dimensions of the tidal basin of De Slufter are very small compared to the tidal wave length. Therefore non-linear distortion inside De Slufter will be negligible. The water level moves more or less uniform throughout the system and uniform with the North Sea water level. Nevertheless we can distinguish three processes that can create an asymmetrical tide: an external asymmetry, a hypsometry effect and a truncation of the tide.

External asymmetry

The tidal wave on the North Sea propagates along the Dutch coast from the south to the north. During this propagation over the coastal shelf, distortion occurs. The effect of friction on the movement of the tidal wave is stronger around low water than around high water. The propagation of the trough of the tidal wave is retarded. Therefore the ebb phase has a longer duration than the flood phase. The tidal wave is already strongly deformed when it enters De Slufter (Dronkers, 1986).

Hypsometry

Tidal deformation can also arise due to interactions with the geometry of the basin. Assuming uniform levels in the basin, this can be derived from the continuity equation. Channel velocities for simple storage basins like De Slufter can be expressed as (Boon and Byrne, 1981):

$$uA_c = \frac{\partial V_b}{\partial t} = \frac{\partial}{\partial t} A_{xy} h \tag{1.19}$$

u   = velocity (m/s)
A_c = cross-sectional area (m^2)
V_b = basin volume (m^3)
t   = time
A_{xy} = horizontal surface area (m^2)
h   = water level

Equation 1.19 can best be defined as the hypsometric relation, where hypsometry is the vertical distribution of basin surface (A_{xy}) area as a function of water level. The influence of morphology on duration asymmetries follows from equation 1.19. When A_{xy} increases to a larger degree than does A_c during the rising tide, dh/dt will be smaller during flood and larger during ebb. The flood duration will therefore exceed the ebb duration, and maximum ebb velocities will exceed peak flood velocities (Walton, 2002). The increase in A_{xy} with water level is large, when the amount of intertidal areas is large.

The influence of the presence of intertidal areas on tidal asymmetry was studied by Speer and Aubrey (1985) who modeled idealized representations of both an ebb- (Wachapreague Inlet, Virginia; US) and a flood-dominated (Nauset Inlet, Massachusetts; US) inlet, with varying percentages of tidal flats. The tidal response of the Wachaprague Inlet model is dominated by the large amount of intertidal areas and the small a/h (tidal amplitude/channel depth) ratio. The system is, even when friction is increased to large values, characterized by a longer rising tide. Simulations of the Nauset Inlet model, characterized by only a moderate amount of intertidal areas (approximately 40%), indicate channel geometry dominates the effects of intertidal storage in this system. Nauset Inlet experiences a longer ebb duration (Speer and Aubrey, 1985). Ebb-dominant basins are characterized by a small a/h ratio (often smaller than 0.2), while that of flood-dominated basins are large (always larger than 0.3; Friedrichs and Aubrey, 1988)

An increase in the amount of intertidal storage capacity, results in a large increase of the relative (2M$_2$-M$_4$)$_{sea}$ phase. Friedrichs and Aubrey (1988) found an increase from values lower than 180° to values larger than 280°. The behaviour shifts from flood- to ebb-dominant. After reaching a maximum relative phase of 280°, phase values drop again to as low as 202°

with a further increasing intertidal storage. So it follows that $(2M_2\text{-}M_4)_{sea}$ tends to rise in estuaries where ebb duration is increased and fall in estuaries where flood duration is increased, with an increasing intertidal storage capacity.

Truncation

A characteristic channel morphology can cause a truncation of the tidal wave. When the channel bottom is located at a higher elevation than the low water level, the tidal signal will be distorted. When water levels decrease during ebb, at a certain moment, water levels in the channel can not drop any further because the channel depth is reached. Offshore water levels however continue to drop (figure 1.5). Water levels inside the channel are not driven anymore by the tidal forcing on the open sea. Water depths in the channel do not drop entirely to zero, because there is still some ebb flow draining the basin. This residual ebb flow may be the result of inefficiency in draining the back-barrier marshes and tidal creeks and the seepage of groundwater. The ebb flow continues draining the inlet, while LWS on the ocean has passed and water levels are increasing again. Water levels in the channel start rising, when the ocean tide has bridged the difference in elevation with the minimum depth of the channel. From this moment on, water levels in the channel are controlled again by the tide. This mechanism can lengthen ebb duration significantly.

Lincoln and FitzGerald (1988) found duration asymmetries D (equation 1.10) of -18% at five small tidal inlets in Southern Maine, US. This indicates a longer duration of the falling tide compared to that of the rising tide. The significance of the truncation effect causing tidal dominance in these small inlets follows from the behaviour during a spring-neap tidal cycle. During spring tide the difference between the low water level and channel bottom level is increased. Ebb duration should increase. The opposite is expected to occur during neap tide. Ebb duration will decrease. This was supported by observations from Lincoln and FitzGerald (1988), who found values for D_{spring} and D_{neap} of -29% and -9% respectively. Truncation plays an important role in the deformation of the tidal signal in these characteristic inlet systems. Since De Slufter has a comparable morphology, the truncation mechanism may be an important mechanism in distorting the tidal signal and causing a negative duration asymmetry.
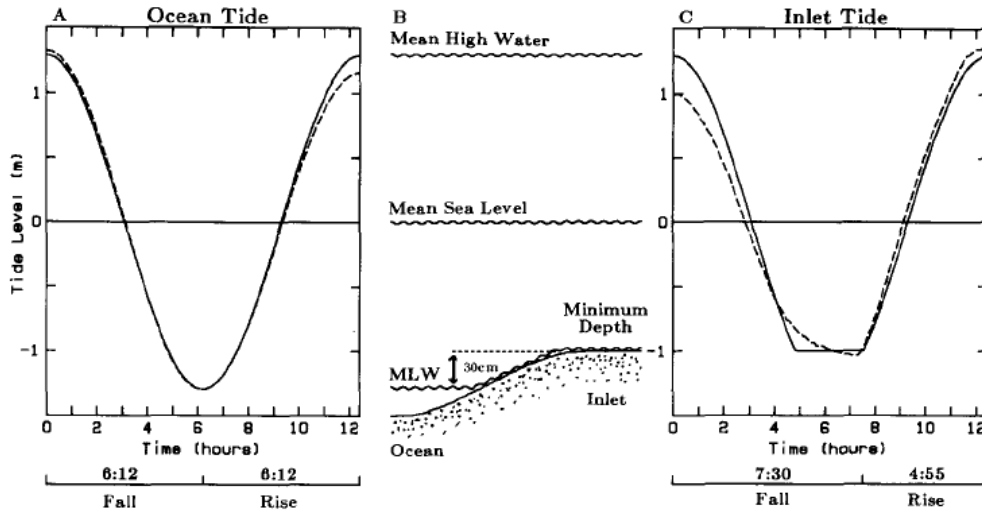
Figure 1.5: a model demonstrating truncation of a symmetric ocean tide interacting with a very shallow channel, with ocean tide (A), a schematized representation of a shallow inlet channel (B) and the truncated inlet tide (C). Plotted are tide record (solid line) and model simulations (dashed line). From Lincoln and FitzGerald (1988).

These three mechanisms mentioned above will influence the tidal signal inside De Slufter, determining the durations of the falling and rising tide and related velocity and sediment transport patterns. This will influence the stability of the inlet system. A fourth mechanism that has the ability to distort the tidal signal includes the response of the system during storm-conditions. During these conditions import and export is not restricted anymore to the channel. The beach flat, southwest of the channel, starts to play an important role. When the water reaches a certain level, import mainly occurs over the beach flat. Export, on the other hand, is generally restricted to the channel. The same pattern is also observed in larger scale estuaries (Fagherazzi et al., 2008).

1.3 Research questions

The goal of this thesis is to study the influence of basin morphology on the hydrodynamics of De Slufter and vice versa and to investigate how this interaction influences the stability and evolution of the system. The following research questions can be specified:

1) What is the morphology and hypsometry of De Slufter, and how does this relate to systems of a larger scale?
2) What is the influence of basin morphology on the hydrodynamics of De Slufter, and what is the specific influence of storm events?
3) Based on simple models, what will happen with the long term (decades or longer) stability of De Slufter?

This study is part of a long term research project of the Department of Physical Geography of Utrecht University into the behavior of slufter systems. Earlier research has been carried out in Het Zwin (e.g. Doomen, 2003), De Zwarte Polder (e.g. Zuijderwijk, 2006) and De Slufter (e.g. Boersema, 2004). Understanding the mechanisms and processes determining the stability of slufters is necessary to preserve the ecological value, and to develop an appropriate strategy for the management of these systems. It is also essential to get insight into the possible flooding risks associated with slufters. Added to this, knowledge about the processes in small tidal inlets can gain valuable insight in the mechanisms at work in much larger tidal inlet systems. This report focuses on the morphology of De Slufter and on the interactions with hydrodynamics in terms of basin stability and evolution.

1.4 Thesis structure

The thesis continues with an overview of all the data collected during the field work period and of the instruments used to collect this data in chapter 2. A short description is given of the different data sets used during this study. Chapter 3 describes the external hydrometeorological boundary conditions during the field campaign. The results are presented in chapters 4 and 5 starting with a description of the morphology of the system (chapter 4). A distinction is made between the long- and short-term development of De Slufter. The short-term development includes a description of the dynamics of all morphological units in De Slufter mouth during the field campaign. Chapter 5 analyzes the tidal deformation in De Slufter. First the magnitude of tidal deformation between the North Sea and De Slufter is studied. Second the possible mechanisms resulting in tidal deformation are discussed. These mechanisms include a truncation of the tide, an external asymmetry and a hypsometry effect. The hypsometric curve of De Slufter is compared with larger scale inlet systems. Chapter 5 ends with a model simulation. A simple hydrodynamical model is used to simulate velocities inside the Slufter inlet. These simulated velocities are compared with measured velocities. Results are discussed in chapter 6 and conclusions are presented in chapter 7.

2. Data collection and analysis

2.1 Measurements

During a field work campaign between 08/09 and 17/10 2008, measurements were carried out in the mouth of De Slufter. We can distinguish between hydrodynamical and morphological measurements.

The morphological behaviour of the system was measured using DGPS. 11 Cross-channel profiles were monitored at least twice during the field work, both before and after storm conditions. Added to this several beach profiles, perpendicular to the shoreline, and a profile covering the complete entrance of the Slufter mouth were measured several times. All profiles used for the morphological analysis are indicated in figure 2.1. Nearly each day of the field campaign, photographs were made of the mouth area of De Slufter.

Hydrodynamical information was collected at four locations and includes measurements of pressure, suspended sediment concentration and flow velocity (appendix 1). Data was gathered during the entire field period at the main frame, located in the narrowest part of the main channel (see figure 2.1). The main frame was placed in the deepest part of the channel. Due to channel migration towards the north, the location of channel relative to that of the main frame changed. At 06/10 the main frame was located in the westernmost part of the channel and was therefore removed and positioned in the deepest part of the channel, approximately 12 metres northwards (figure 2.2B).

Furthermore two removable 'mini frames' were used to collect data at different locations in de Slufter (figures 2.1 and 2.2A and indicated with blue in appendix 1). During the storm conditions from day 275 to 280 these mini frames were located on the beach flat which got inundated regularly during this period. They were orientated in the direction of maximum wave incidence during the storm.

To analyze the deformation of the tidal wave, when it propagates from the North Sea towards De Slufter, offshore water levels were collected. Offshore water levels used in this study originate from the measuring station *Texel, Noordzee* (see figure 2.1; red square in the image below the legend). This station is located at a distance of 1 km from the coast, and 4.2 km southwest of De Slufter. Water levels are measured here every 10 minutes. Offshore wave heights and angles used in this study were collected by the measuring station *Eierlandse Gat*, located in the inlet between Texel and Vlieland.
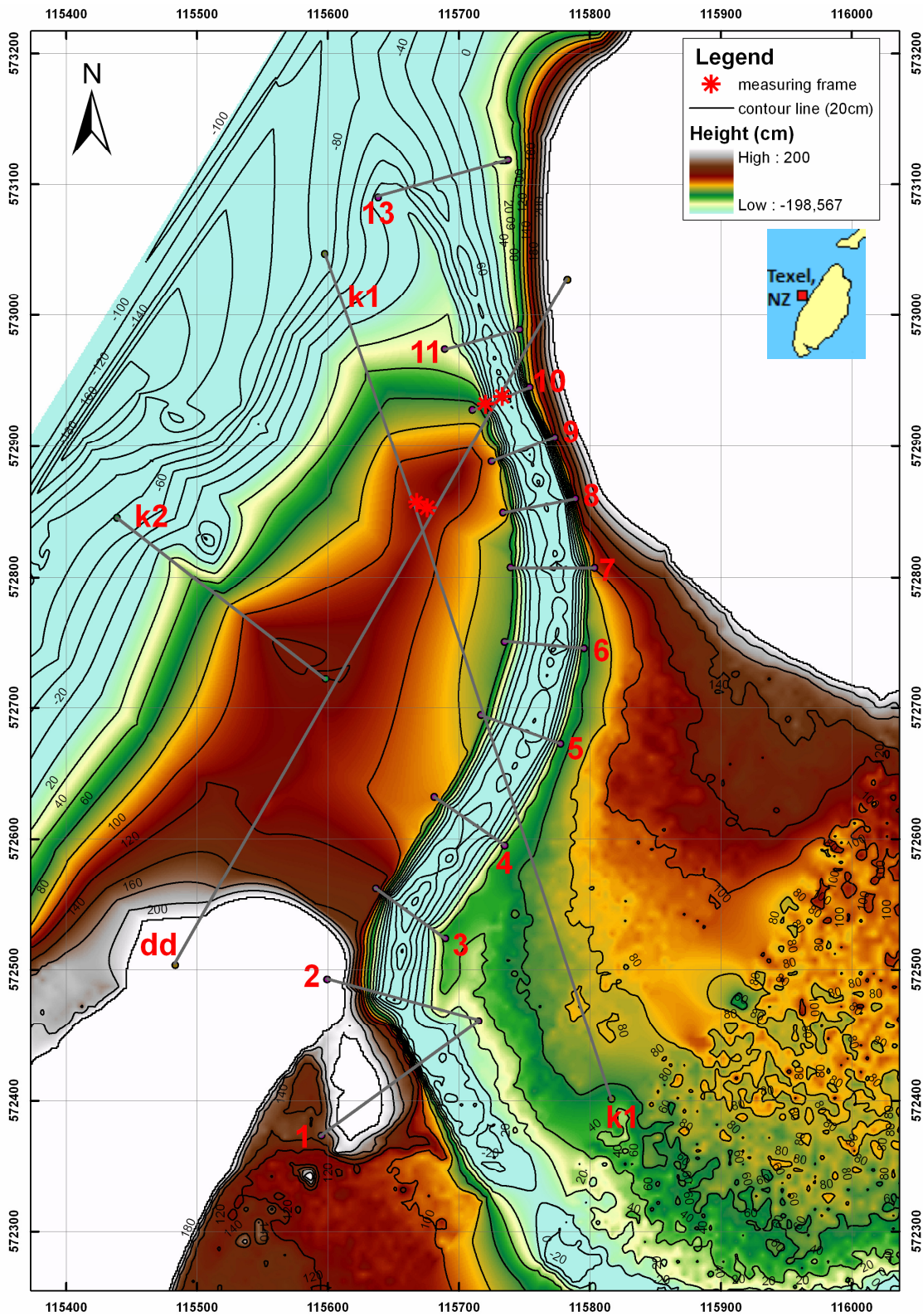
Figure 2.1: contour map of the mouth of De Slufter, with all measurement locations and locations of the dune to dune profile (white), beach profiles (yellow) and 12 channel profiles (red) indicated on it. Figure also includes the location of measuring station Texel, Noordzee (red square in figure below the legend). This figure represents the situation between 06/10 and 09/10.

2.2 Parameters and instruments

2.2.1 Morphology

The change in morphology of De Slufter mouth was monitored by measuring several profiles. These profiles were measured before and after storm conditions to study the impact of a storm event on the morphology of De Slufter mouth.

Morphological information (x, y, z coordinates) of the system was measured using a Differential Global Positioning System (DGPS). A tripod base station containing a GPS antenna was setup at a known location. This base station collects satellite information to determine its location. A second tripod containing a radio modem was placed nearby and connected to the base station (figure 2.2D). The radio modem transfers satellite information from the base station to a mobile rover with a handheld logger in the field. The location of individual points (x, y, z values) in the field is determined by correcting for the base location. Morphology and water levels (2.2.2) were all related to NAP (Dutch ordnance level; close to mean sea level)

Daily photographs of the main channel were taken from the highest location at the dune row north of the entrance of De Slufter. Photographs were used to illustrate migration patterns.

2.2.2 Water level

Water levels were measured to study the deformation of the tidal wave between the North Sea and the channel of De Slufter. The change in water level with time (dh/dt) was also used in the hypsometry model, to simulate velocities in the channel. Assuming hydrostatic pressure, water level can be derived from information about the pressure:

$$H_w = \left(\left(P_{measured} - P_{air}\right)/\rho g\right) + H_s \qquad\qquad (2.1)$$

H_w = water depth
$P_{measured}$ = pressure measured by the Keller sensor
P_{air} = pressure of the air measured with a barometer
ρ = density of water
g = gravitational acceleration
H_s = height of the pressure sensor above the bottom, relative to NAP

Pressure was measured using Keller pressure sensors. Every frame contained one pressure sensor.

2.2.3 Flow velocities

Flow velocities are measured with Electro Magnetic Flow (EMF) meters (figure 2.2C). The EMF meter creates a magnetic field in the sea water, which will act as an electrical conductor. The rate of change in electric potential, which originates due to flowing water, is measured by a pair of electrodes. These electrical signals are then converted to corresponding flow velocities. Calibration occurred in the lab. The main frame contained three EMF meters above each other at heights of 15 cm, 25 cm and 65 cm above the bed, whereas the mini frames contained one EMF meter at 15 cm from the bed level. Especially when the mini frames were located in the breaker zone and on the beach flat, this height of 15 cm regularly changed due to rapidly varying bed heights and a repeating prolapse of the mini frames. Velocities are measured in the X- and Y-direction (horizontal components).

2.2.4 Suspended sediment concentrations

Suspended sediment concentrations were measured with Optical Back-Scatterance (OBS) sensors (figure 2.2C). The sensor transmits a high-intensity infrared beam to the sea water containing the suspended sediment. These particles reflect or scatter the beam. The degree of scatter and reflectance is mainly determined by the amount and size of the particles. Calibration must therefore occur with the sediment that is suspended at that position. Here we assume that this is similar to the sediment at the locations of the individual frames. The main frame contained 8 OBS sensors at heights varying from 15 cm to 90 cm above the bed. The mini frames each contained 3 OBS sensors at heights above the bed of 15 cm, 25 cm and 40 cm.
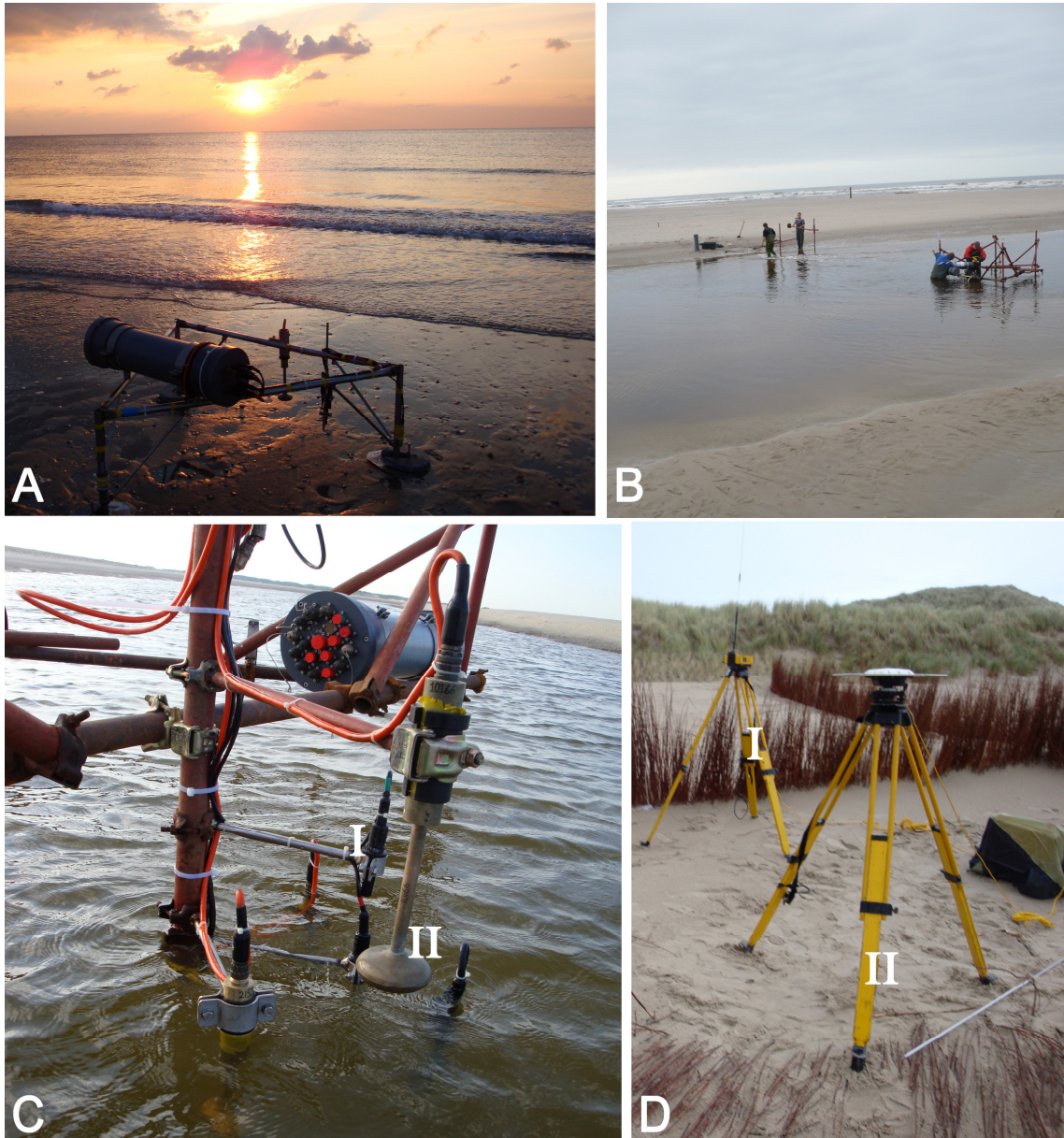
Figure 2.2: overview of instruments used during field work, including mini frame (A), main frame with initial (left) and final (right) location (B), instruments on the main frame (C) with one of the OBS-sensors (I) and one of the EMF meters (II), and the DGPS (D) with radio modem (I) and receiver (II).

2.3 Measuring method

Two different data collection protocols were used to collect data with the mini frames. From 08/09 until 24/09, continuous measurements were carried out with a frequency of 2 Hz. Because a frequency of 2 Hz is too small to sufficiently describe wave related processes, from 24/09 onwards the software was replaced by a program collecting data at 4 Hz. With this program measuring occurred in bursts of 17 minutes, followed by 13 minutes without measurements. Data was transferred from the data logger on the frames towards a laptop.

During this data transfer no measurements could be carried out. The main frame measured continuously with a frequency of 4 Hz.

3. Boundary conditions

3.1 External conditions

The boundary conditions during the field work are summarized in figure 3.1. The first weeks of the field campaign were characterized by calm weather with prevailing eastern winds. A set-down of the water levels was observed. Two storm events can be distinguished after this calm period. The first event lasted from Julian day 274 to day 277. A calmer day followed, before a second storm period started from day 279 to 280. During this second storm event the maximum offshore significant wave height (4.78 m) was slightly higher than during the first storm event (4.50 m). Its impact was however somewhat smaller, because the tidal range and related maximum water levels were larger during the first event. This is related to the fact that the first storm almost coincided with spring tide (table 3.1, figure 3.1). After this period of high energetic conditions, weather became calmer again, but less calm than before the storm-events, as can be derived from the set-up and wave heights.
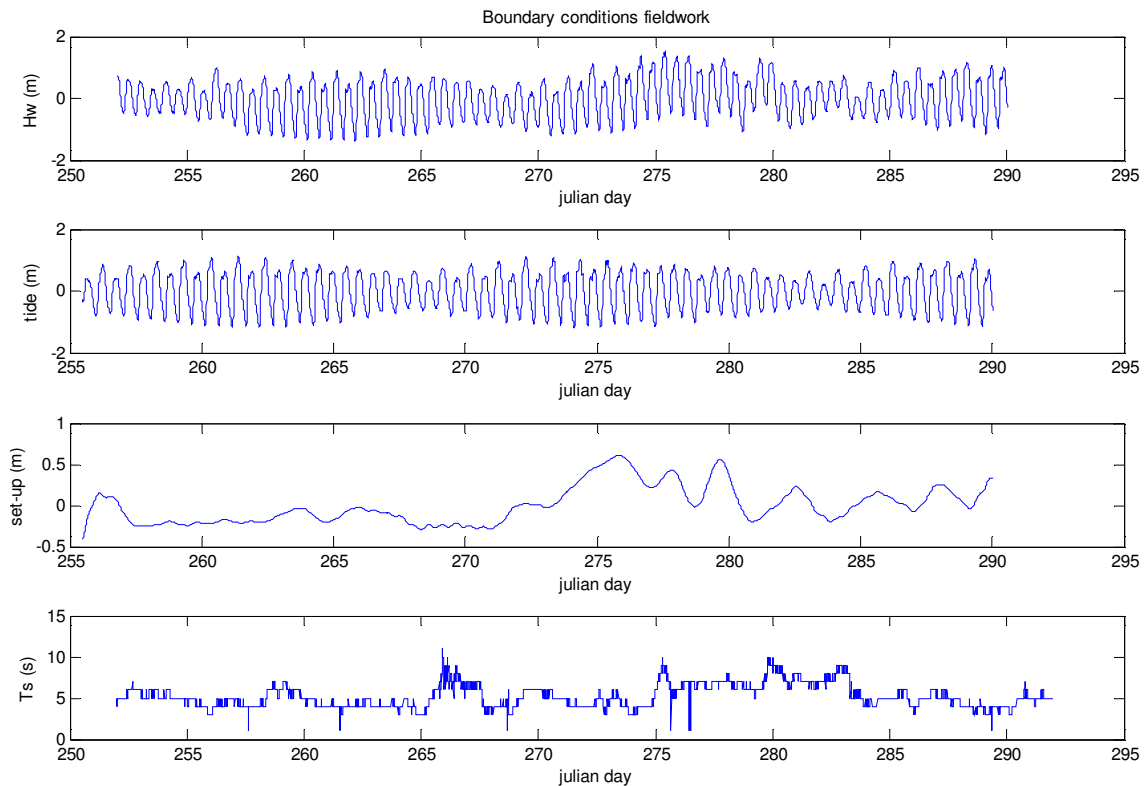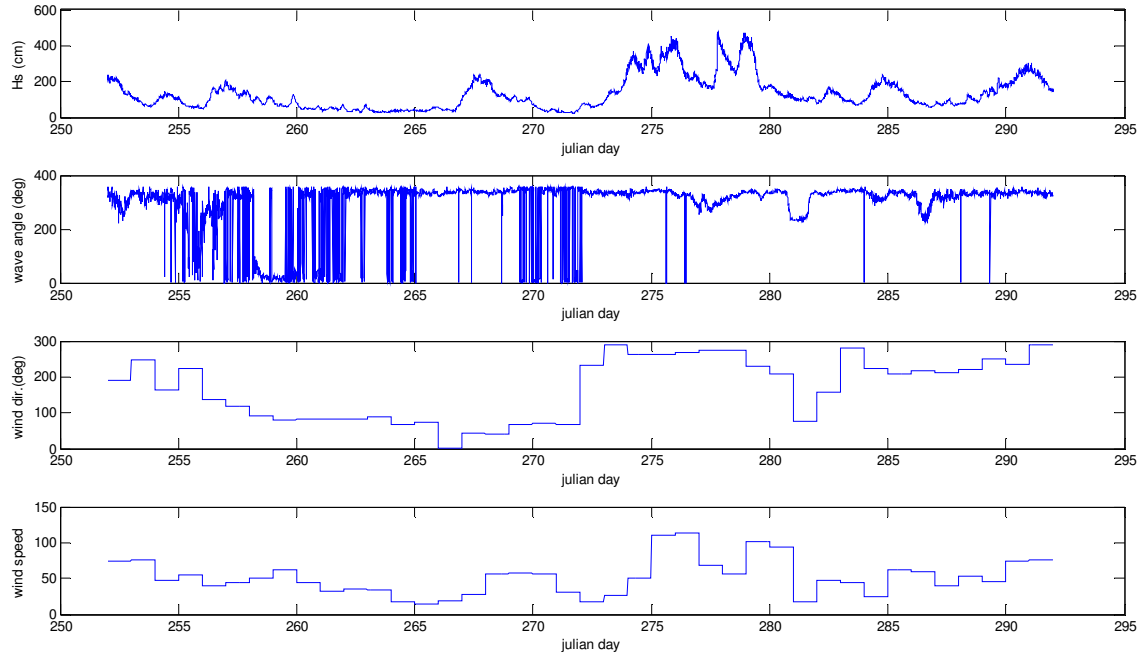
Figure 3.1: boundary conditions during the field campaign, with water level (Hw), the tidal and non-tidal (set-up) components of Hw, the wave period Ts, the significant wave height Hs, the wave angle and the direction and speed of the wind (dm/s).

Storm event	$H_{s, off max}$ (cm)	Period (jul. days)	Wind dir (°)	Tidal range (m)	Set-up (m)
event 1	450	274.0-276.5	W (270°)	2	0.60
event 2	478	277.8-279.5	W (270°)	1.3	0.55

Table 3.1: storm-events during the field campaign, including the duration of the event and the offshore significant wave height, wind direction, tidal range and set-up during the peak of the events. After Klein-Breteler (2009)

An overview of the long term wind and wave conditions for the area of the Texel Inlet west of Texel is given in Elias et al. (2006). For a large degree, similar conditions will count for De Slufter. The average wind direction is west-southwest, with an average speed of 7 m/s. This results in a prevailing northeast-directed longshore current. Wind-generated waves are dominant. Swell is less important. The long-term mean significant wave height and period at the Eierlandse Gat, the inlet northeast of Texel, was determined at 1.3 m and 5 s respectively. 90% of the waves come from a direction between southwest and north. Waves can become up to 6 m in height during storm events. This especially occurs during northwestern winds, when the fetch reaches maximum values.

The average wave angle during the initial fair weather conditions of the field campaign was 342.7 degrees (between NNW and N), while the average angle during storm conditions was 324.7 degrees (between NW and NNW). The average wave height was 0.86 m and 3.05 m during calm and storm conditions respectively. During the fair weather conditions the average wave height was significantly lower than the long term average (1.3 m) and wave angles were larger (closer to North) compared to the long term average. Wave

periods were comparable (4.9 s during the calm weather of the field work compared to 5 s on the long term).

3.2 Decomposition of the tidal signal

The signal of the measured water level consists of three components: a tidal component, a non-tidal residual and a wave component:

$$z(t) = z_{non-tidal}(t) + z_{tidal}(t) + z_{wave}(t) \qquad (3.1)$$

The non-tidal component is generated due to varying meteorological conditions. During periods of high pressure, water level will be lower than predicted by the tidal signal. Periods of low pressure, increase the water level. This is called the 'inverse barometer effect' (Smith, 1979). Apart from this effect, wind can generate a wind set-up and a wave set-up. During the storm events the total set-up reached values up to 0.6 m. When the deformation of the tidal signal is analyzed, we are only interested in the tidal component. Therefore the non-tidal component has to be detected and subtracted from the total signal. This was done with a low pass filter. Low pass filtering passes the low frequency components and blocks the higher frequency components. The divide between passing and stopping is determined by a cut-off frequency. In this study the LOESS Matlab software package was used to separate the astronomical tidal signal from the total water level signal.

4. Morphological development Slufter

4.1 Long-term development

Before the 13th century, Texel consisted of two parts: the island *Texel* in the south and the island *Eyerland* in the north. In between was the Anagat inlet, which was probably created during a large storm event in 1164. In the 13th century the Eierlandsche Gat inlet originates, still existing until today. The opening of this larger inlet eventually resulted in the closure of the Anagat inlet. A large shoal now connected *Texel* with *Eyerland*, which only was flooded during spring tidal conditions. To stabilize this connection and to prevent the reopening of the inlet, a sand drift dike (*'stuifdijk'*) with a length of 6 km was made in 1629-1630 on the shoal. To gain land, another *stuifdijk* was created in 1835 at the Wadden Sea-side of the initial dike. The same was done in 1855 at the North Sea-side. In 1858 a severe storm however results in a breakthrough of this *stuifdijk* in the northwest of Texel at three different locations. During this process three Slufters emerge: *De Muy*, *De Grote Slufter* and *De Kleine Slufter* (figure 4.1).

Figure 4.1: historical map from the northwestern part of Texel, indicating the locations of De Grote Slufter and De (Kleine) Slufter.

De Muy and *De Grote Slufter* were successfully closed in respectively 1860 and 1887. Similar attempts were made to close *De Kleine Slufter* in 1902, 1905 and 1925, but these temporary closures were without avail. Storm events reopened the inlet in all three occasions. *De (Kleine) Slufter* still exists until today. After the last attempt to close De Slufter, natural processes determined its evolution again. A large migration of the channel occurred,

strongly eroding the dunes south of the entrance. In 1957 the channel mouth migrated 1.5km to the southwest (figure 4.2). The system recovered by creating a shortcut to the sea back in the north (Schoorl, 1999 in Boersema, 2004; Durieux, 2004).
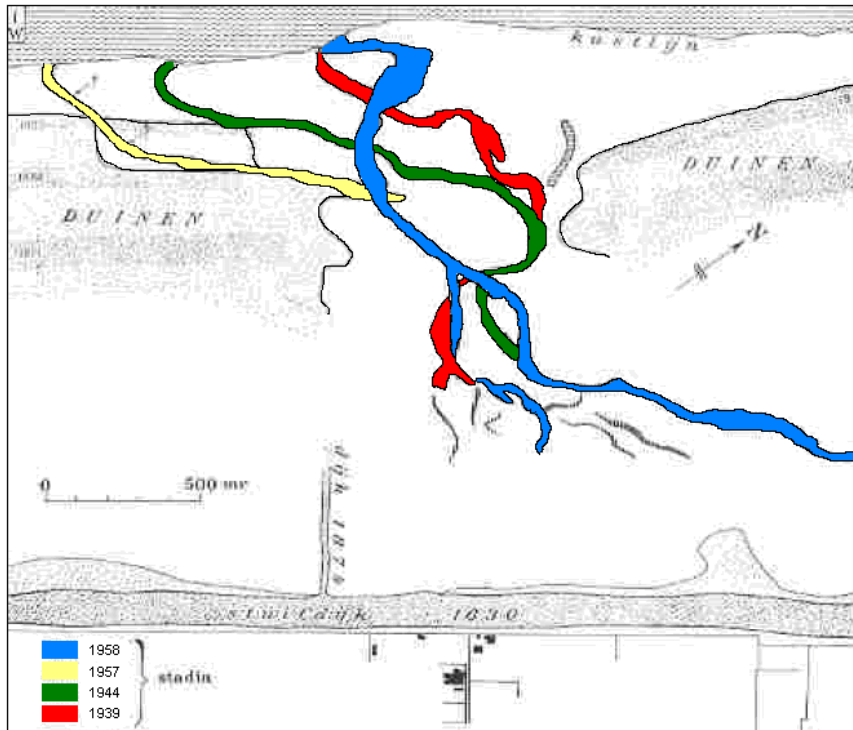
Figure 4.2: migration of the Slufter channel from 1939 to 1958. A southward channel migration was observed between 1939 and 1957 when the most southward location was reached. After van der Borg and Dorsser (1961) in Durieux (2004).

It's uncertain why there is a difference between the present migration direction (to the northeast) and that during the 1940s and 1950s (to the southwest). This is probably related to the decrease of the entrance width in the 1970s. Starting in the 1970s, coastal protection became increasingly important. To reduce the effect of incoming waves in the basin the entrance width between the dune rows was diminished from 700 to 400 meters. As the channel migrated northwards the Dutch Department of Waterways and Public Works (*Rijkswaterstaat*) started with active interference. When the channel reached the dunes northeast of the entrance it was relocated back to the southwest to prevent dune erosion. Sand is dumped in the active channel in the northeast and a new channel is created in the southwestern part of the mouth area.

Comparing yearly aerial photographs of the Slufter mouth for the last three decades, reveals a cycle extending 3-7 years. As an example of this cycle, photographs from 6 consecutive years in the 1990s are compared in figure 4.3. The first stage of the cycle starts with a very small channel length (1992; the remnants of the previous channel are still visible,

almost perpendicular to the new channel). The curvature of the channel is weak, flowing in a near straight line through the most southwestern part of the entrance area towards the North Sea. The most southern meander bend is not very well developed. The channel migrates northwards. The orientation rapidly changes and the curvature increases. As the curvature increases to a further degree, the channel in the southern part of the system gets a semicircular shape. In its most seaward reach the channel sharply turns off in northwestern direction in the shortest possible, straight line to the sea. In the final stage of the cycle (1997, 1998), the channel flows perpendicular to the dune row north of the entrance. At the most confined part of the entrance, the channel created a NE-SW direction and flows close to the dune row southwest of the inlet. The large southern meander bend is now very well developed. As the cycle develops, the meanders increase in size. Further migration to the northeast will erode the dune row east of the inlet. This will enlarge the width of the entrance, increasing wave influence inside the basin. The channel is relocated back to the south by *Rijkswaterstaat*. Interference of this order occurred in 1973, 1978, 1983, 1986, 1991, 1998, 2002, 2005 and 2009.
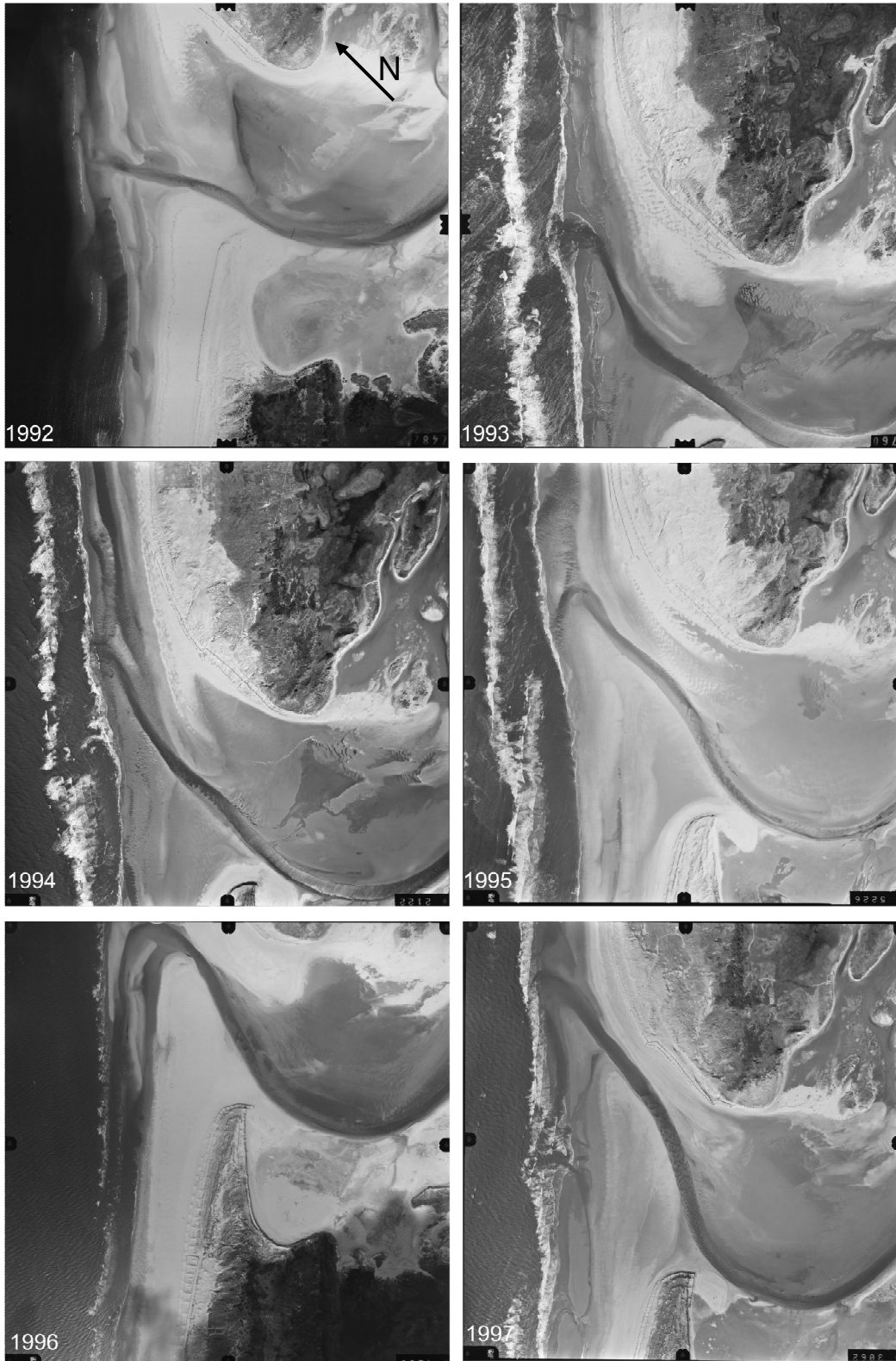
Figure 4.3: aerial photographs of De Slufter entrance area from 1992, 1993, 1994, 1995, 1996 and 1997. The orientation of the photographs is not north-south. North arrow indicated in photograph from 1992.

4.2 Short-term development

4.2.1 Method

The short-term morphological development of De Slufter was monitored by measuring several profiles in the mouth area at different moments during the field campaign. Inaccuracies in profile measurements arise, because the different points of a profile never exactly lie on a straight line. Therefore the sum of the distances between the points along the profile is larger than the real cross-sectional distance. This is problematic when we want to plot bed level against distance. To avoid this, the actual position is projected on the nearest position of the defined cross-section, assuming that the bed level is equal. With this assumption it is possible to represent a certain profile as a straight line. This is depicted in figure 4.4: the measured points (i.a. points A and B) do not lie on a straight line. By assuming a constant height along the lines A-a and B-b, the measurements can be represented by a straight line. We are now able to plot bed height as a function of distance.

This approach assumes a constant bed level on every line perpendicular to the profile. In reality, however this will not be the case. Complex bed forms covered the channel bed reaching heights up to several decimetres. This will also influence measurement accuracy of cross-sectional surface areas.
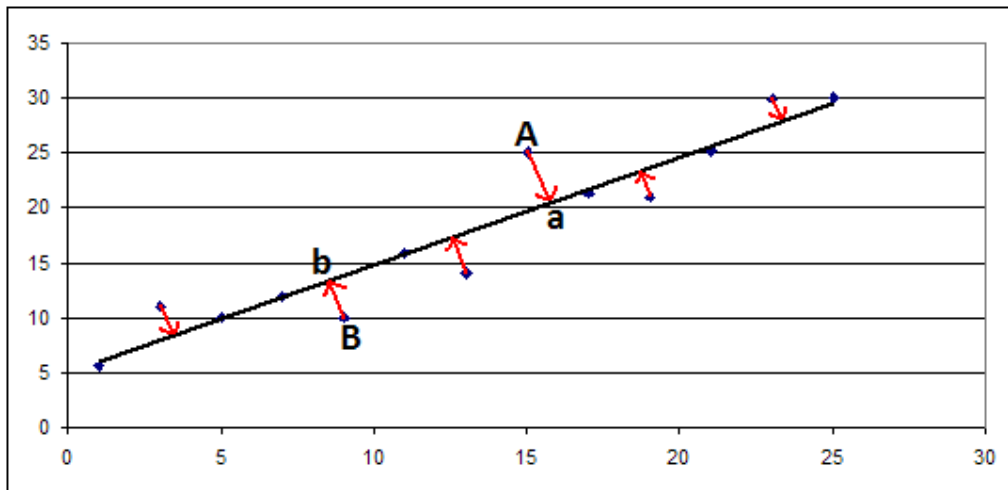
Figure 4.4: example of the corrections applied to the points measured with DGPS. The measurements do not lie exactly on a straight line as can be seen at points A and B. This is corrected by assuming a straight line including the points a and b.

Describing the morphology of De Slufter, we can distinguish between the mouth area and the back-barrier area. The mouth area is roughly the area seaward of the narrowest dune opening. In this mouth area we can further distinguish between the beach, the beach flat and the channel. The beach is the most dynamic part, constantly changing under the influence of incoming waves. The morphological changes of this part during the field work

are discussed in section 4.2.2. The channel imports and exports water and sediment to the back-barrier area and back to the North Sea. Under the influence of the prevailing northeastward directed longshore current, the channel migrates in the northeastern direction. As observed during the field work, this migration is largest during storm conditions (4.2.4). These are also the conditions when the beach flat gets inundated. This area mainly has an elevation ranging between 1 - 1.2 m. The morphological development of the beach flat, during the field campaign, is discussed in section 4.2.3. The entire Slufter basin is characterized by a very large surface area with an elevation between 1.1 m and 1.5 m +NAP. The implications of this characteristic morphology will be explained in chapter 5. The back-barrier area consists of a salt marsh dissected by a pattern of small tidal channels. The largest parts of this back-barrier region are only flooded during storm events and wave influence is negligible. Therefore, morphological changes are expected to be rather small. No morphological measurements were carried out in the back-barrier area. Data from the AHN are used for this area. The surface area of the entire system, until an elevation of 2.5m +NAP, comprises 419.7 ha (figure 4.5). At a water level of 2.5m +NAP, the system contains ~5350000 m^3 of water. The tidal prism and pre-storm cross-sectional surface area of the inlet during spring-tidal conditions (with a water level of 1m +NAP) equal ~436000 m^3 and 60.6 m^2 respectively.
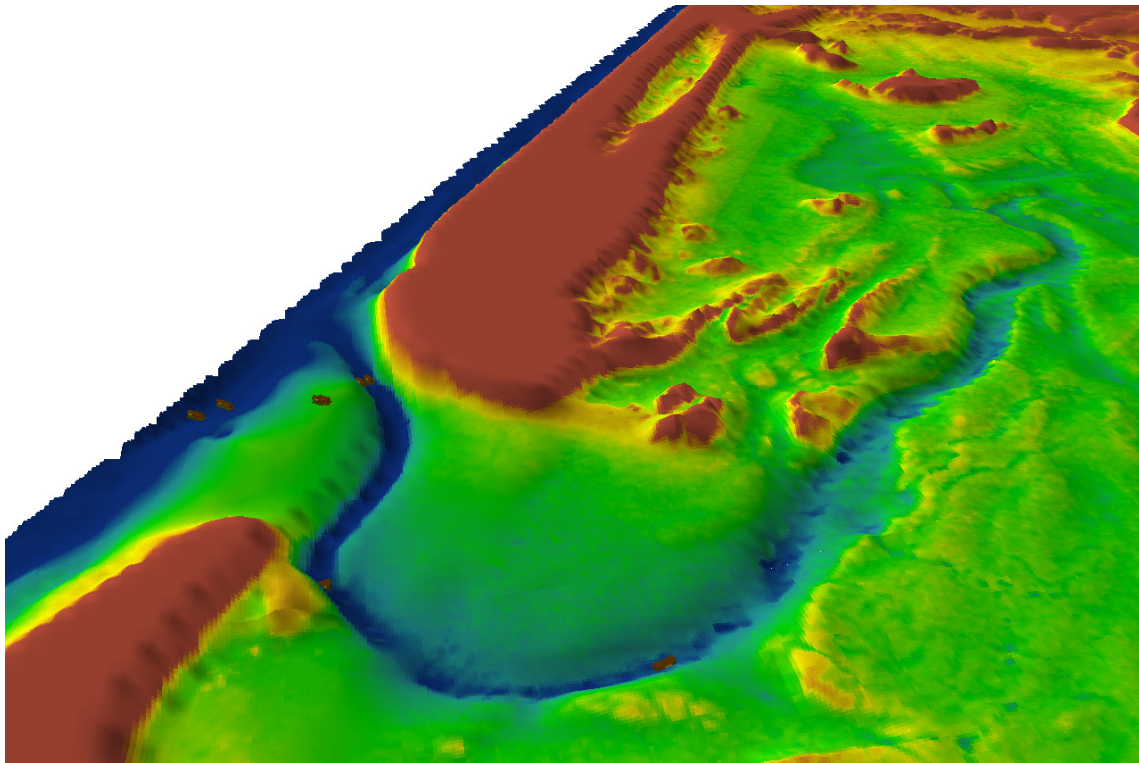
Figure 4.5: 3D-representation of the system (DEM), obtained by merging the field DGPS-measurements with the AHN. The locations were hydrodynamic measurements were carried out are indicated on the map. All elevations higher than 3m +NAP are cut off and indicated in red.

4.2.2 Beach

Two beach profiles were measured before and after storm-conditions. Profile k1 is located nearly 75 metres west of, and parallel to the main channel (figure 2.1). This profile was measured before the storm (12/09) and at the end of the first storm event (02/10). During pre-storm conditions, the breaking zone of the beach was characterized by a ridge and runnel system (figure 4.6) with a somewhat steep beach face. Beach morphology strongly changed during the storm. Wave height increased, destroying the ridge and runnel pattern (figure 4.7). The beach state shifted to a more dissipative state with a slight decrease in height and slope of the beach face.

17/09 (pre-storm)

Figure 4.6: beach morphology showing a ridge and runnel system at 17 September which has disappeared after the storm at 1 October (right).

Profile k2 is located southwest of profile k1 (figure 2.1). This profile was measured at the end of the first storm event (02/10) and after the second storm event (07/10). The ridge-runnel system was already largely destroyed here during the first storm event. The profile was further flattened during the second storm event (figure 4.8). Both profiles show a landward retreat of the beach due to storm conditions. Both storm events caused a retreat of approximately 6-8 meters.
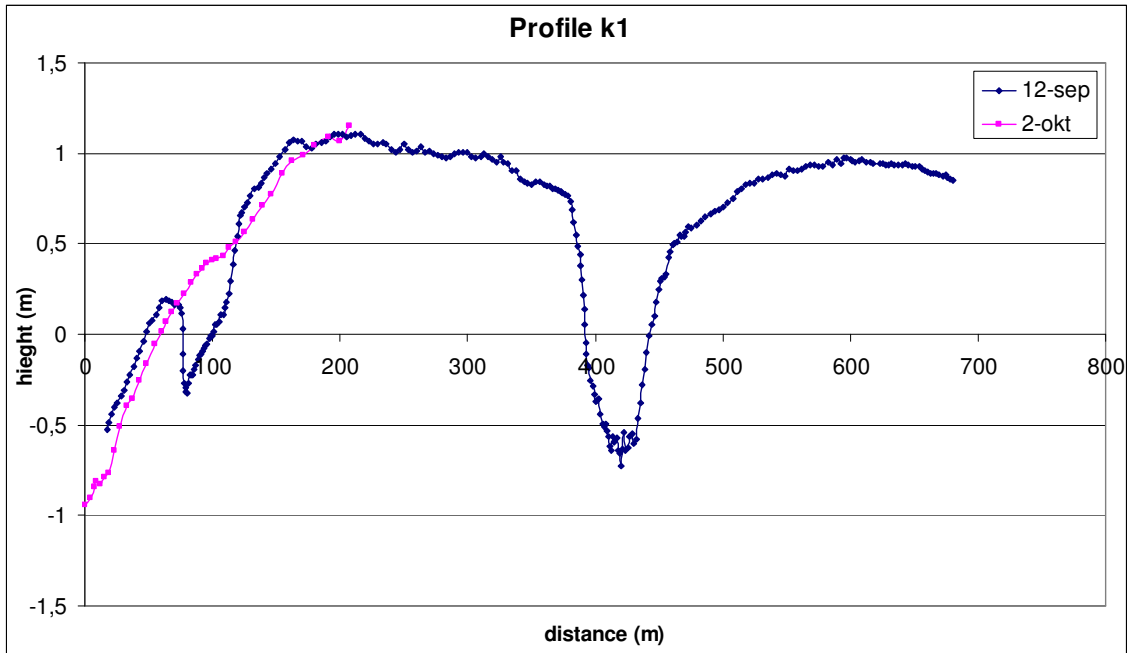
Figure 4.7: profile k1, with distance starting (0m) at most seaward location. Going from north to south in figure 2.1, indicated are respectively: the start and end location of the 02-10-profile and the end location of the 12-09-profile. This profile is not entirely perpendicular to the coastline, so distances are slightly exaggerated.
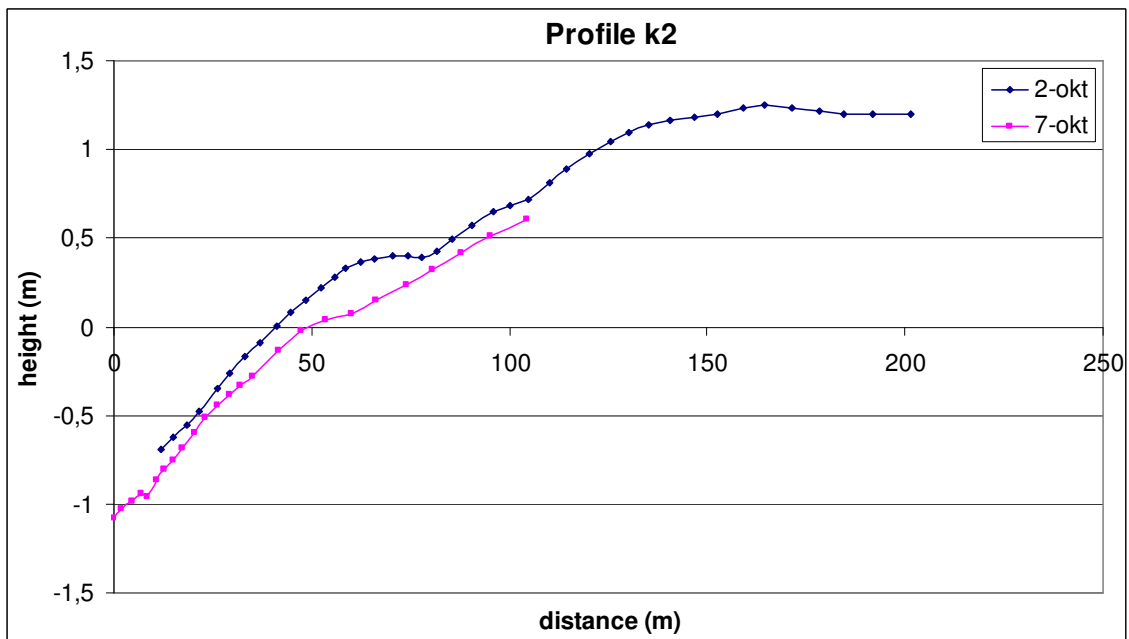
Figure 4.8: profile k2, with distance starting at the most seaward location (see figure 2.1).

4.2.3 Beach flat

Morphological changes on the highest part of the beach flat were monitored with a profile covering the whole Slufter mouth from the dunes in the southwest to those in the northeast of the entrance (profile dd; figure 2.1). A clear change can be seen between pre-

storm (12/09 and 29/09) and post-storm (02/10 and 11/10) morphology. The beach flat was never inundated completely between 12/09 and 29/09. No significant changes occurred during this interval, with elevations ranging between 1.0 and 1.1 metres.

Accretion occurs during the storm events. Elevation increases on most parts, by up to 15 centimetres (figure 4.9). Immediately after the first storm event (02/10), morphology is irregular with a large amount of small bars and troughs. The maximum height is in the order of 20 to 30 centimetres, while the length varies from approximately 20 centimetres to more than 1 metre. Those were probably caused by the waves, present during the storm. Several days after the second storm-event (11/10), morphology becomes more regular. The troughs were filled and the surface is smoothened again (figure 4.9). The average accretion on the complete beach flat between 29/09 and 11/10 amounts 5.5 cm. Largest accretion occurred on the central part of the flat.
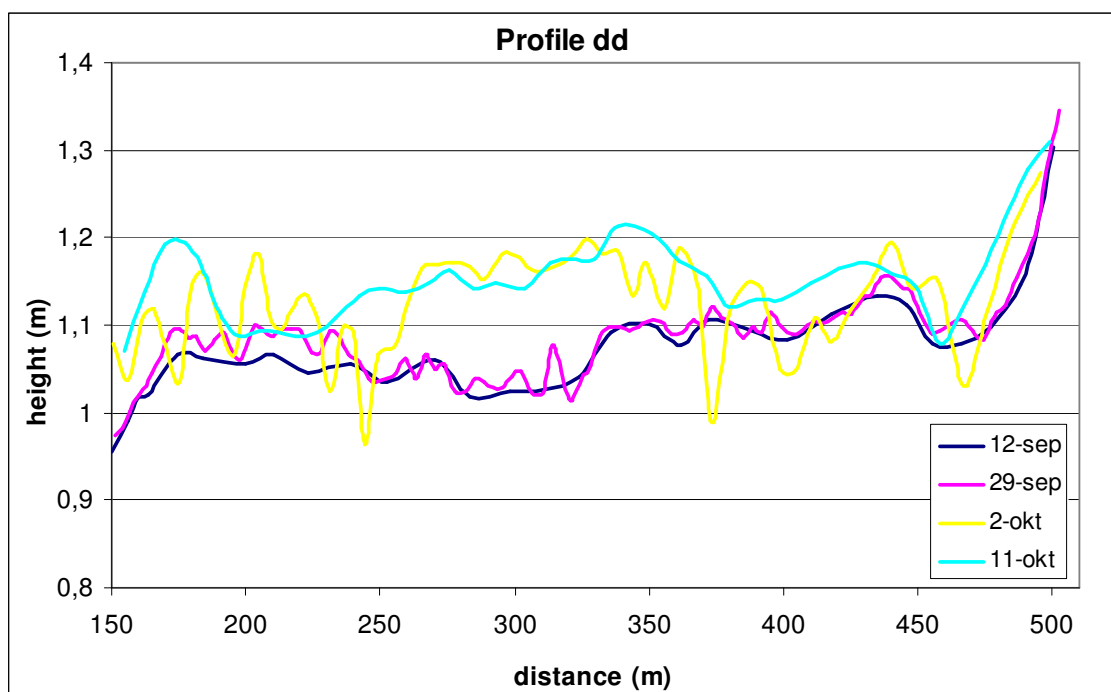
Figure 4.9: profile dd, with distance starting at 150 metres (just west of the channel) to the dunes west of the entrance (see figure 2.1).

4.2.4 Channel

11 Cross-channel profiles between the North Sea and the most southern meander bend were monitored during the field work campaign (figure 2.1). All profiles were measured before the storm-events, during calm weather conditions (16/09 or 17/09), and at least once after the two storm-events. Profile 10, located near the main frame, was measured six times. Change in channel morphology decreases in a landward direction, from a very large

migration at the very seaward reach of the channel to almost no migration near the meander bend.

The first days of the field work (16/09 - 28-09), the weather was very calm, with prevailing eastern winds. Observations reveal very small migration rates during this period. Two storm-events followed, resulting in a large migration of the seaward part of the channel. No channel migration was observed at profile 1. Pre-storm and post-storm morphologies exactly match (figure 4.10). At profile 2 (not shown), the western channel side was subject to an eastward migration of up to 5 metres, pointing to a small narrowing of the channel. The contrary occurred at profile 3 (not shown) where the channel slightly widened. The storm-events resulted in a small migration (2/3 metres) of the western channel side to the west. Profiles 4, 5 and 6 show the same storm-induced behaviour. The highest parts of the channel sides, more or less, remained at the same place, whereas the shape of the channel changes from rounded to slightly more rectangular (figure 4.11): the channel widened. This implies an increased cross-sectional surface area after the storm-events. The eastern channel side migrated to the east. Since profile 7 was only measured once during the field campaign no comparison can be made for the changes of this section of the channel. A combination of channel migration and widening occurred at profiles 8 and 9. The eastern channel side migrated approximately 10 metres. Migration was less for the western side ranging from nearly no migration at profile 8 to an eastward migration of 3/4 metres at profile 9 (figure 4.12). Profile 8 is characterized by a large widening of the channel, while profile 9 is also characterized by an eastward migration of the entire channel. Profile 9 also shows the influence of both storm-events individually, due to a measurement between the two storms (04/10). It seems that the second storm-event had a slightly larger impact (6 metres) compared to the first event (4 metres) in terms of migration distances. The same pattern for the eastern channel side is visible at profile 10 (figure 4.13), but migration is larger with distances of 6/7 metres and 8 metres for the first and second storm-event respectively. During the calmer weather after the storm events (7/10 - 14/10) a westward retreat of the channel is observed of nearly 3 metres. Largest changes in channel position and morphology can be seen in the most seaward section, at profiles 11 and 13. During calm weather (17/09) the channel at profile 11 was located in the west, with a width of 26/27 metres at 0 m NAP. The storm-events induced a channel migration of 10 (western channel side) to 18 (eastern channel side) metres. The channel became much wider (35/36 metres at 0 m +NAP) and less deep (maximum channel depths decreasing from -1 m NAP pre-storm, to around -0.6 m NAP post-storm). No large changes were observed in the period after the storms (07/10 - 14/10). Surprisingly, a large northwestward migration occurred at profile 13 (figure 4.14). This is probably related to the beach morphology with its ridge and runnel system, as will be explained in section 6.1. The storms shifted the channel 32/34 metres westward (09/10).

During calmer conditions afterwards (09/10 - 13/10), the western side of the channel rapidly migrated 10 metres back to the east. The eastern channel side remained at the same place during this period, strongly reducing the cross-sectional area of the channel. Unfortunately, profile 12 was only measured once, making it impossible to describe the morphological development in this section of the channel.
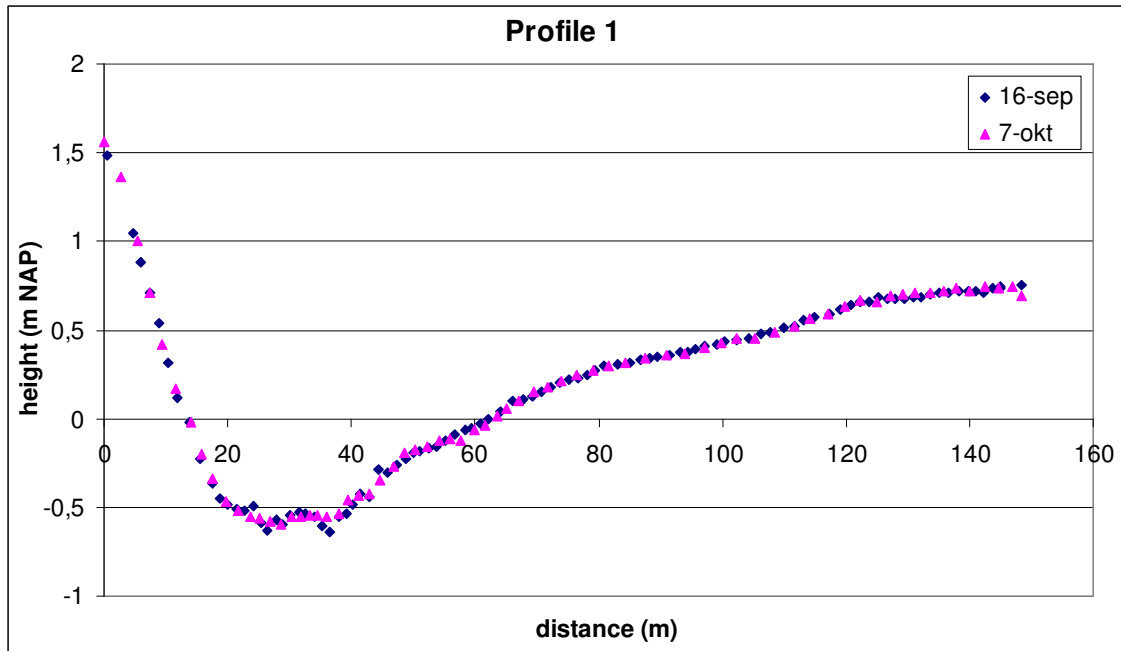
Figure 4.10: channel morphology at profile 1 at 16/09 and 7/10.
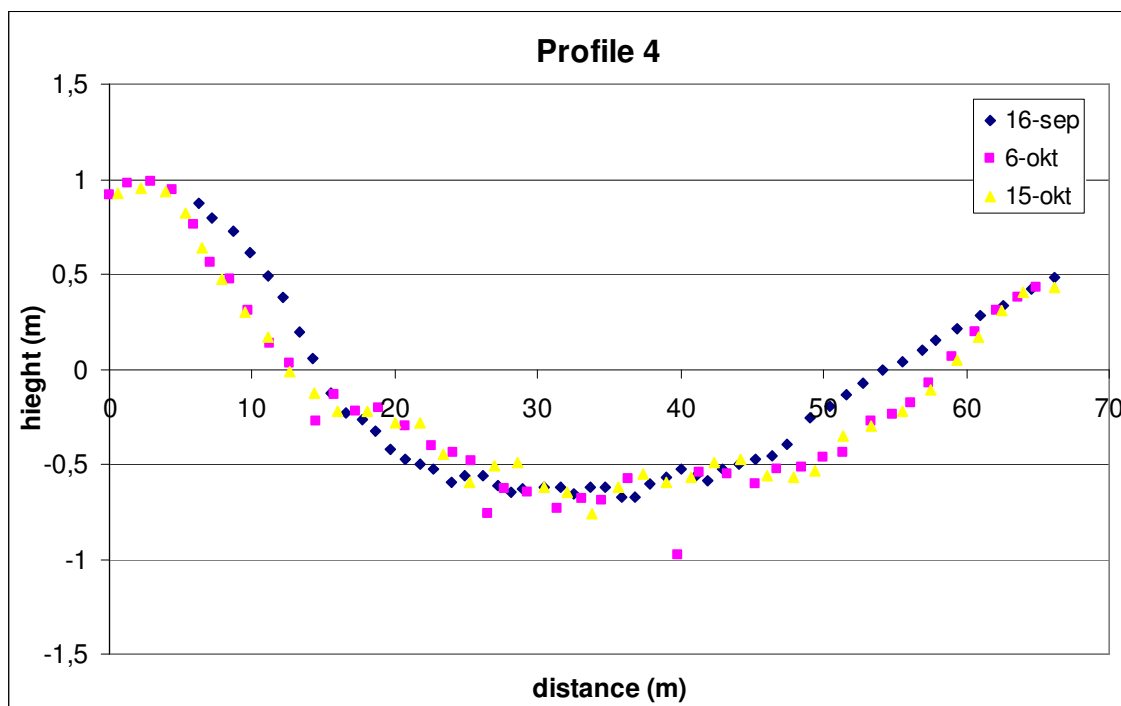
Figure 4.11: channel morphology at profile 4 at 16/09, 06/10 and 15/10.
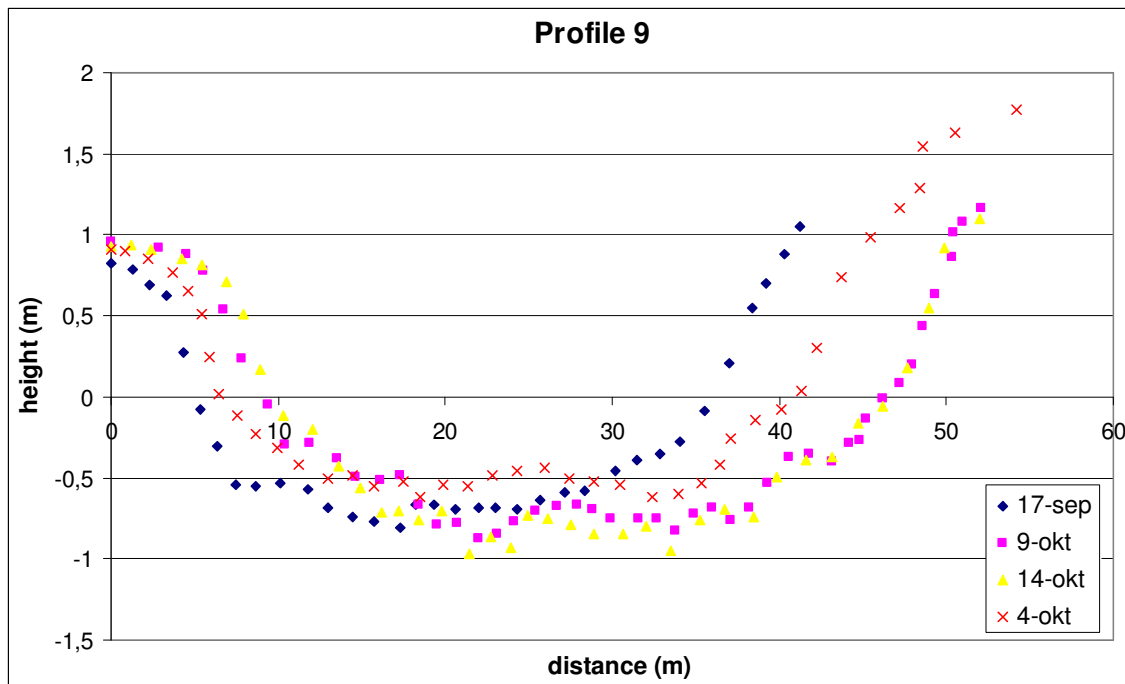
Figure 4.12: channel morphology at profile 9 at 17/09, 04/10, 09/10 and 14/10.
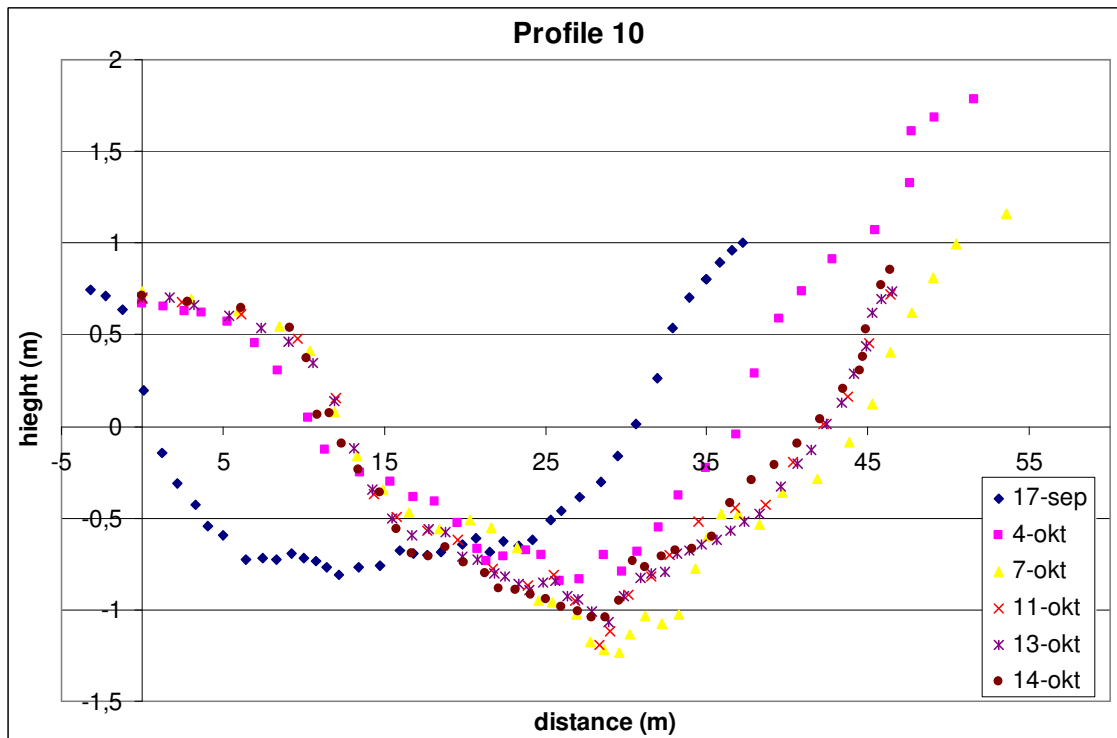
Figure 4.13: channel morphology at profile 10 at 17/09, 04/10, 07/10, 11/10, 13/10 and 14/10.
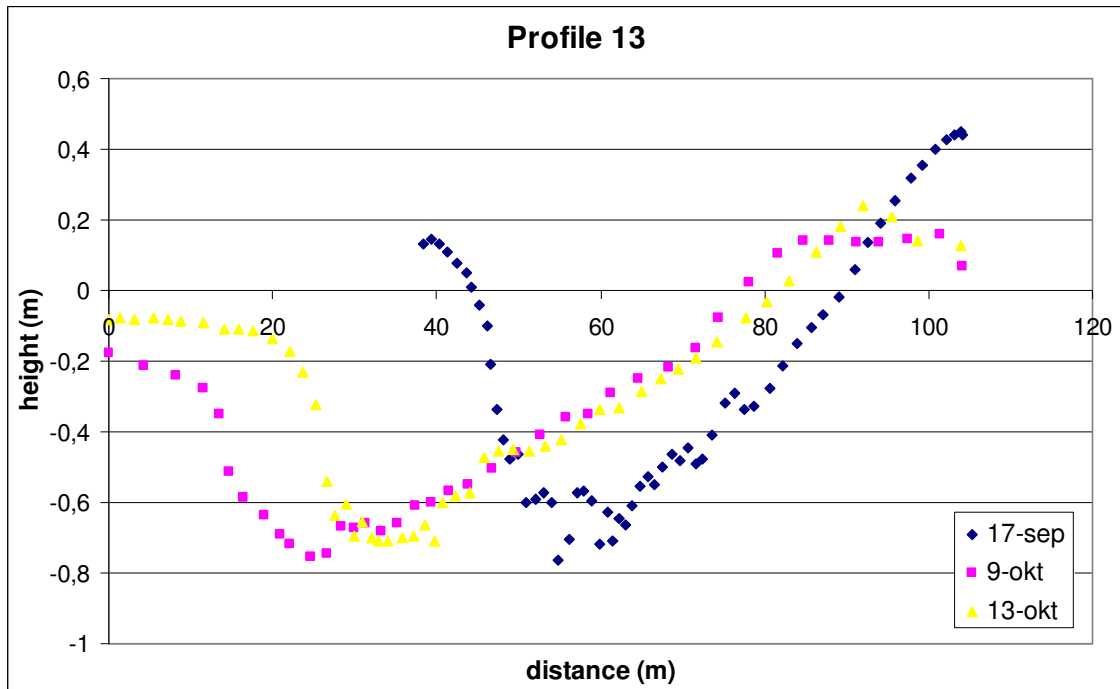
Figure 4.14: channel morphology at profile 13 at 17/09, 09/10 and 13/10.

Three processes are visible, analyzing the morphological development of the channel. We can distinguish between migration of the channel, a change in channel curvature and a change in channel geometry. In figure 4.15 the -0.2 m contour line is shown. This line approximately represents the positions of the channel at low water. It follows from figure 4.15 that storm-induced changes in channel morphology are largest near the sea and decrease in landward direction. Significant migration of the channel was only observed at profiles 6 and 9-13. Profiles 3-8 are only characterized by a widening of the channel. Changes in orientation are especially large between profiles 11-13, but as the curvature of the channel increases, the orientation of the channel near profiles 4-10 also changed (figure 4.15). Possible mechanisms causing the spatial and temporal variability in channel migration are further discussed in chapter 6.
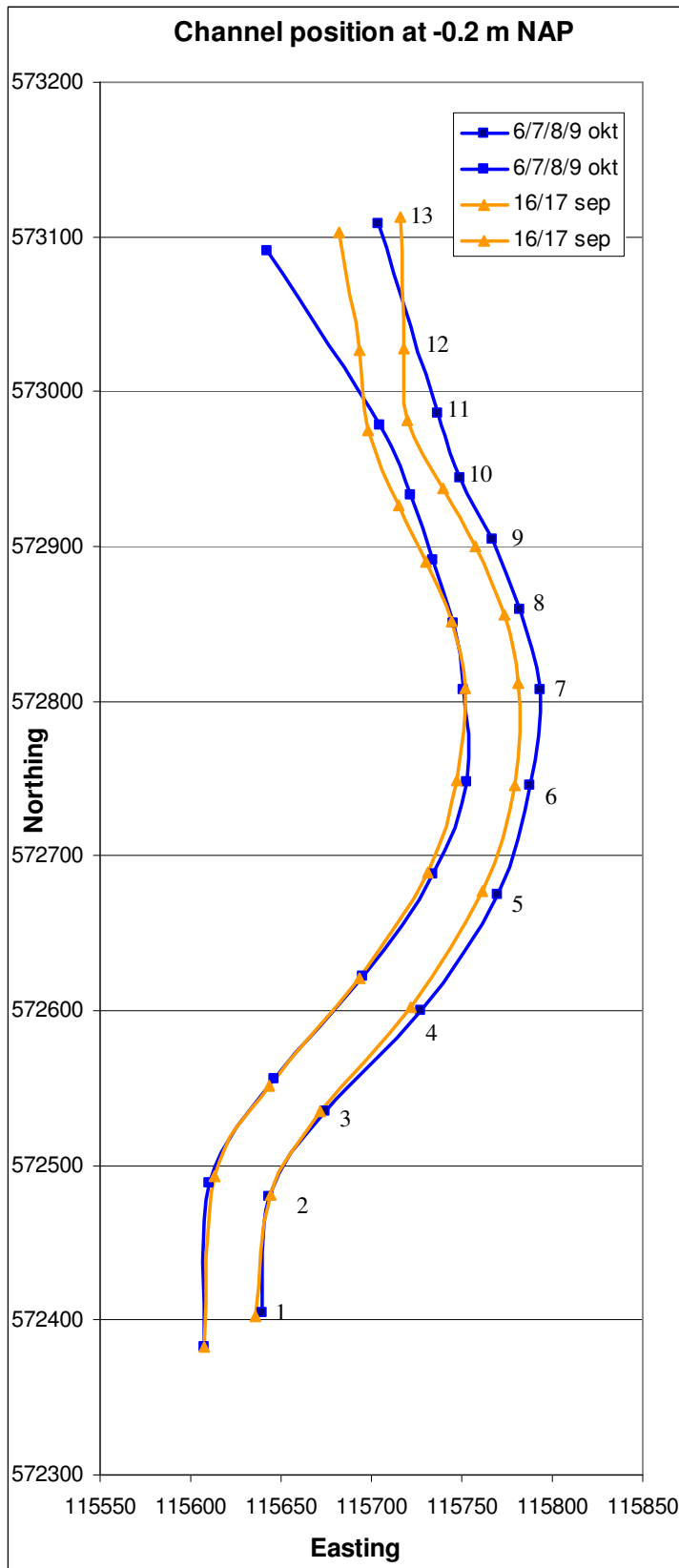
Figure 4.15: overview of the channel position at -0.2 m NAP for 16/17 September (pre-storm) and for 06/07/08/09 October (post-storm).

4.2.5 Cross-sectional areas

The cross-sectional area of the channel varies significantly between the profiles. Largest cross-sections are found in the most landward section of the channel (profile 1) where flow velocities are relatively small. The cross-sectional area decreases in seaward direction where flow velocities are largest. Smallest cross-sectional areas are observed at profiles 8-11 (table 4.1). Near profile 13 the cross-sectional area increases again (figure 4.16).

	16/17 sept	6/9 okt	14/15 okt
Profile 1	41,170	41,202	
Profile 2	39,677	37,252	
Profile 3	36,796	41,661	
Profile 4	35,463	39,784	38,442
Profile 5	32,861	38,585	
Profile 6	38,608	32,450	
Profile 8	28,283	41,651	38,666
Profile 9	28,831	35,858	36,253
Profile 10	28,873	32,600	30,949
Profile 11	28,616		35,430

Table 4.1: cross-sectional surface areas (m^2) of the channel profiles below 0.4 m +NAP for 3 different periods.
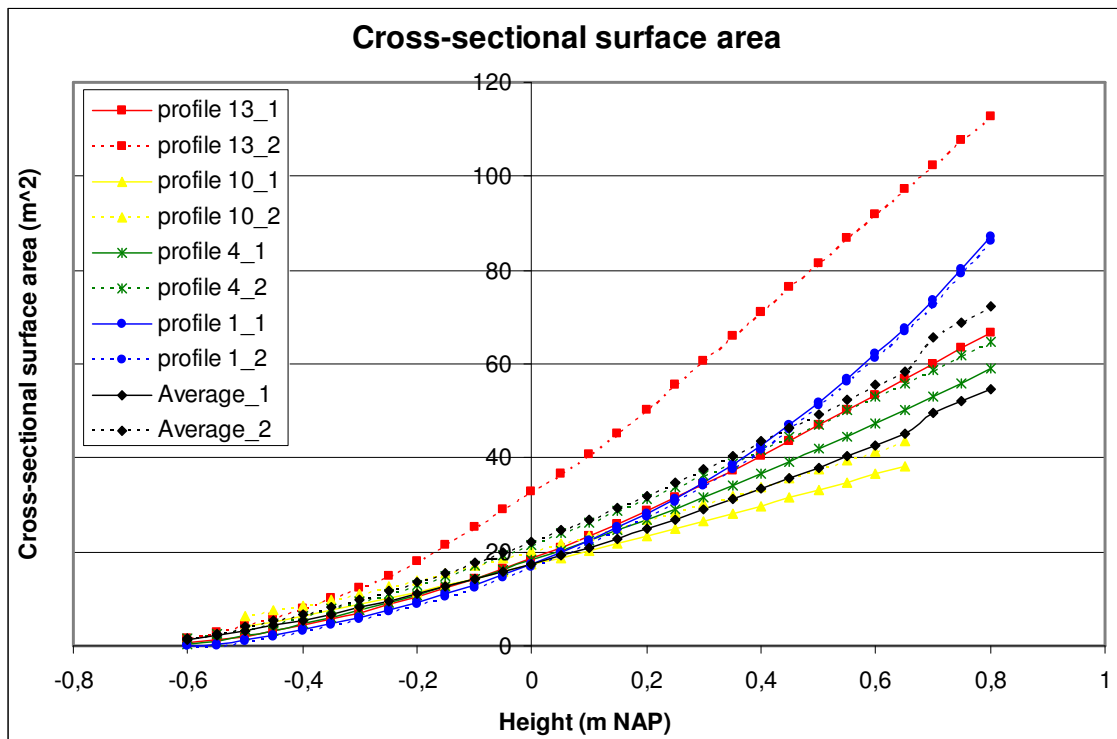
Figure 4.16: cross-sectional area of the channel for four profiles (1, 4, 10 and 13) at two moments during the field campaign: pre-storm (16/17 September) indicated with a full line (nr. 1) and post-storm (6/9 October) indicated with a dashed line (nr. 2). Averaged cross sectional areas are also included. Largest changes in morphology are observed at profile 13 and smallest changes at profile 1.

Figures 4.16 and 4.17 and table 4.1 show the changes in cross-sectional surface area due to the storm conditions. During the storm events, velocities are larger than average. Stream power increases, resulting in scour at the channel bottom. Channel shape shifts from rounded to slightly more rectangular. The channel is able to discharge larger amounts of water. The cross-sectional surface area of the seaward section (profiles 8-10) of the channel between 16/17 September and 6/9 October increases on average 21% (at +0.4 m NAP; table 4.1) to 23% (at -0.3 m NAP). In the landward section (profiles 1-4) of the channel these changes are much smaller. On average the cross-sectional surface area of this section increases 4% (both at -0.3 m NAP and +0.4 m NAP; table 4.1). At profile 1 no storm-induced changes in morphology are observed (figure 4.16). As mentioned in paragraph 4.2.4 the largest changes occurred at profile 13 (figure 4.16). The average increase in cross-sectional surface area between 16/17 September and 6/9 October ranges between 9.4% (at -0.3 m NAP) to 15.7% (at +0.4 m NAP; figure 4.17). Profiles 9 and 10 were also monitored in between the two storm events on 4 October. Whereas larger cross-sectional surface areas were expected compared to those before the storm, the contrary was monitored. Cross-sectional surface areas decreased by up to 14.9% (at +0.4 m NAP; black line in figure 4.17). Some profiles show a small decrease in cross-sectional surface area, as is the case for profile 10. Here this decrease can be attributed to the westward migration of the eastern channel side. The channel had narrowed.
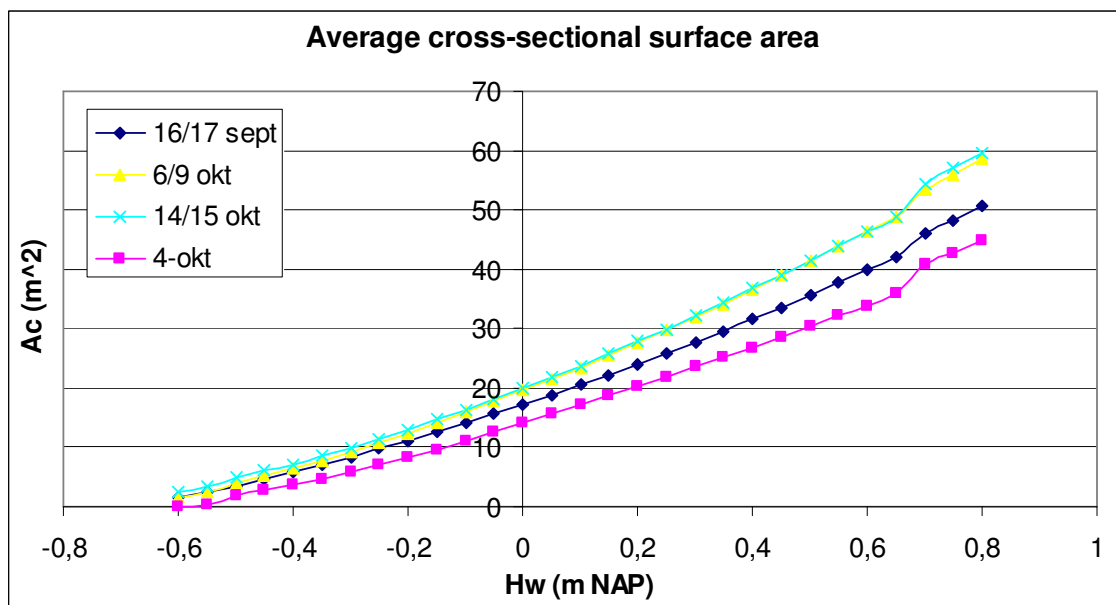
Figure 4.17: cross-sectional area of the channel averaged for profiles 4, 9, 10 and 11 plotted against water level for three different periods (16/17 october, 6/9 october and 14/15 october). The graph also includes the average Ac from profiles 9 and 10 for 4 october.

5. Tidal deformation

The tidal wave gets deformed when it enters the channel of De Slufter. The possible mechanisms that result in such a tidal distortion include the truncation of the tide, a hypsometric effect related to the morphology of the basin and a circulation that occurs during storm-conditions. Apart from these processes the tide may already be deformed on the North Sea before it reaches De Slufter. This chapter starts with an analysis of the magnitude of tidal deformation in De Slufter (5.1). The contribution of tidal truncation and the hypsometry effect to this deformation are studied in sections 5.2 and 5.3 respectively. In paragraph 5.4 the previously explained mechanisms are used to describe several hydrodynamical characteristics of De Slufter. The implications for sediment transport are discussed in paragraph 5.5. Using a simple hydrodynamical model, velocities in De Slufter are simulated in section 5.6. With this model we are also able to study the influence of storm events on the behaviour of the system.

5.1 Deformation of the tide

5.1.1 Wavelet analysis

In order to study the deformation of the water level and the velocity signal between the North Sea and the channel of De Slufter, the harmonic components of these time series have to be determined. In general a Fourier Transform (FT) or a least-squares harmonic analysis (HA) is used. However these techniques are limited to stationary signals, indicating a signal with an amplitude and phase constant over time. These methods can only give *time-averaged* information about the amplitude and phase of the several frequency components. The transformed signal does not contain information about the frequency as a function of time. It is unable to tell *when* these certain frequency components exist.

The tidal signal measured at the channel of De Slufter is however non-stationary, indicating the amplitude and phase evolves over time. This is caused by the effect of wind set-up which is not constant over time. The techniques mentioned above (FT and HA) are therefore not applicable for the Slufter-signal. A wavelet analysis is performed which is ideally suited for this purpose. In a wavelet analysis the time signal is decomposed into time-frequency space. From this, the dominant frequencies and phases and its variation in time can be derived. Information about the time and frequency are derived simultaneously (Lau and Weng, 1995; Torrence and Compo, 1998).

The wavelet MATLAB software package of C. Torrence and G. Compo* was used to analyze the tidal deformation of the water level signal between the North Sea and De Slufter. 10 minute-average signals were used in the Wavelet Transform. The wavelet analysis

identifies the frequencies present in the signal, from which the amplitudes of M_2 and its overtides M_4, M_6 and M_8 could be determined accurately. The amplitudes are a function of time. Apart from the amplitudes also the phases of these components could be determined.

5.1.2 Duration asymmetry

A large duration difference is visible between water level at the North Sea and at the Slufter channel (figure 5.1). Whereas the moment of High Water (HW) almost occurs at the same moment for the North Sea and the Slufter Channel, there is a large difference between the moments of Low Water (LW). LW at the Slufter channel occurs much later in time compared to LW at the North Sea and the breaker zone. The LW level at the North is also much lower than that at De Slufter. The duration of the falling tide in De Slufter is much longer than that of the rising tide (table 5.1). On average, ebb duration increases by 53.5 minutes, with an ebb duration of 7h37. From table 5.1 it can also be seen that the tidal signal on the North Sea is already distorted with an average ebb duration of 6h43. Duration asymmetry D (equation 1.10) increases from D = -8.34% at the North Sea to D = -22.73% at the main frame.

	North Sea (jul. day)	main frame (jul. day)	difference (minutes)
mean ebb duration	0.280058043	0.317372124	+ 53.73227612
mean flood duration	0.236940299	0.199833515	- 53.43376866

Table 5.1: mean ebb and flood durations and duration differences between North Sea and main frame.

---

* Available at *http://paos.colorado.edu/research/wavelets/software.html*
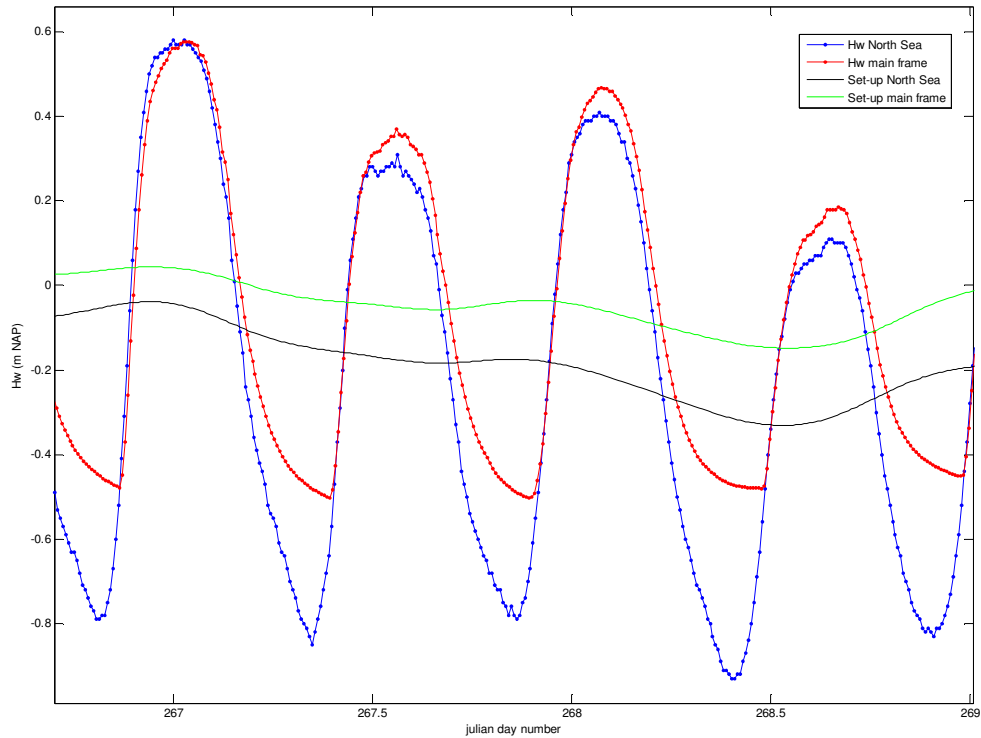
Figure 5.1: water levels (Hw; m) and set-up at North Sea and Slufter channel (main frame).

5.1.3 Deformation of the amplitude

The time signal of water level and velocity were analyzed by a wavelet analysis. This analysis reveals a large distortion when the tidal wave enters the channel of De Slufter (figure 5.2). M_2 amplitudes on average reduce 0.15m (table 5.2), but large differences occur during a spring-neap tidal cycle. Whereas the M_2 amplitude at the North Sea decreases from 0.75-0.7m at spring tide to 0.45-0.5m around neap tide, variation at the Slufter channel is much smaller. The same accounts to M_4 amplitudes, with equal M_4 amplitudes at neap tides for the North Sea and the Slufter channel. This pattern can also be found for the M_4/M_2 ratio. On average, ratios are much higher for the North Sea (0.146) compared with the Slufter channel (0.109), but during neap tides this ratio is slightly larger in the channel than at the North Sea.
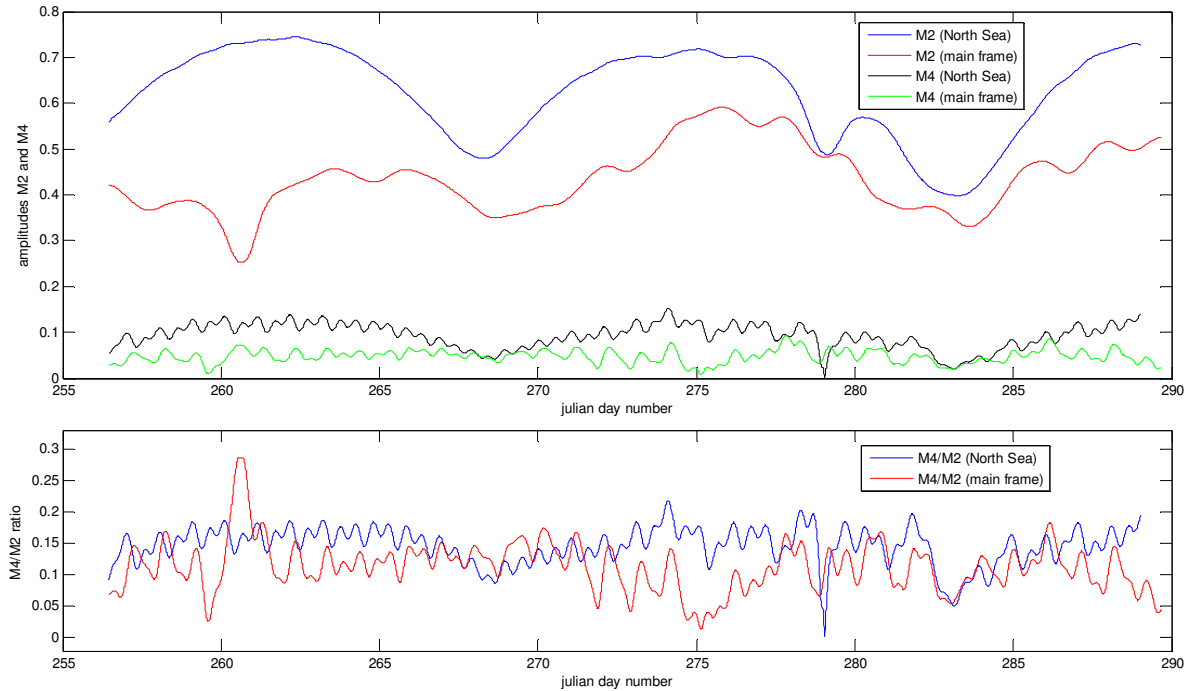
Figure 5.2: M2 and M4 amplitudes (upper) and M4/M2 ratios (lower) for the North Sea and breaker zone of De Slufter (both in meters) covering the complete field campaign.

NORTH SEA - MAIN FRAME (period: 263,6007 - 288,6389)					
	M2	M4	M6	M8	M4/M2
North Sea	0.59945	0.087675	0.088718	0.043072	0.146259
Main Frame	0.44913	0.048879	0.067006	0.039224	0.10883

Table 5.2: M2, M4, M6 and M8 amplitudes and M4/M2 ratios for the North Sea and channel (main frame).

5.1.4 Deformation of the phase

The relative phase relationship between M_2 and M_4: $(2M_2-M_4)_{sea}$, for the Slufter channel varies between 280° and 350° for most of the field work period (figure 5.3), indicating a longer ebb and shorter flood duration (equations 1.8-1.10). Only during storm conditions the phase shifts to values between 0 and 180°, which would indicate an ebb dominant bed load transport (see 1.2.4). During the propagation of the tidal wave from the North Sea towards the channel of De Slufter $(2M_2-M_4)_{sea}$, increases from approximately 225° to 300-310°. Flood duration at the North Sea is slightly longer compared to De Slufter.
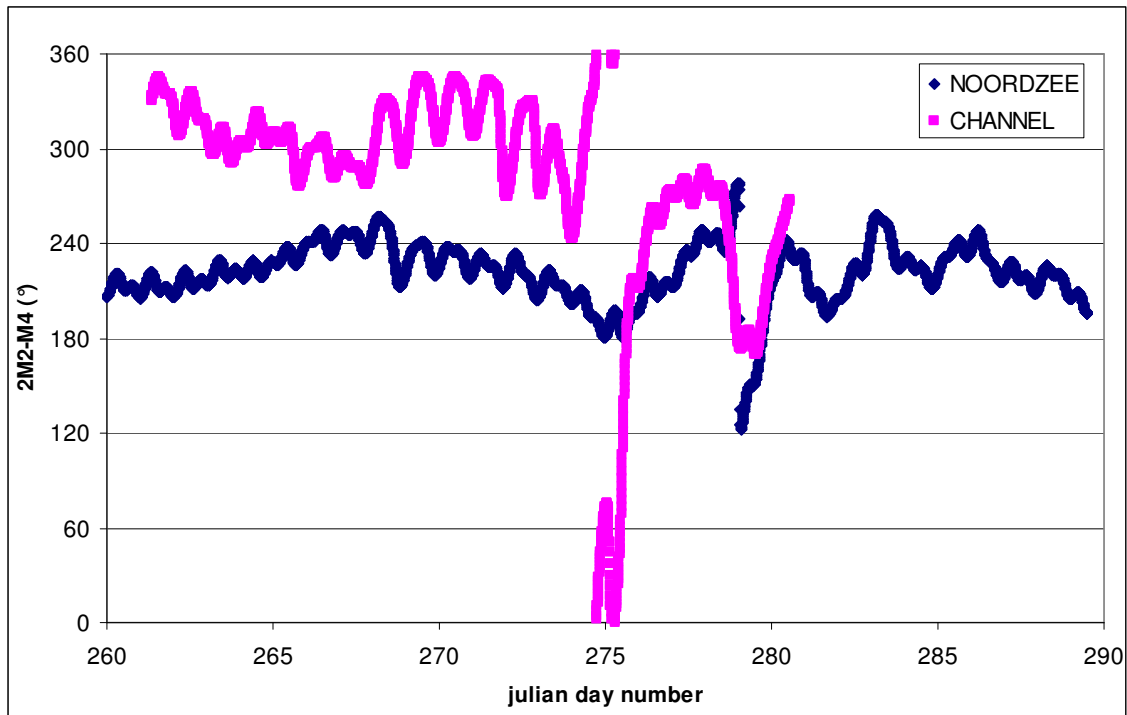
Figure 5.3: phase relationships (2M$_2$-M$_4$)$_{sea}$ for the North Sea and the main frame.

As mentioned in section 5.1.2 the tide is already deformed on the North Sea where there is a negative duration asymmetry of D = -8.34%. This external asymmetry can however not explain the increased asymmetry in De Slufter where D = -22.73%. Other processes must cause this tidal asymmetry. The next paragraphs discuss the effects of truncation (5.2) and hypsometry (5.3).

5.2 Truncation of the tide

The tidal wave is truncated when it enters the channel of De Slufter. This is caused by the morphology of the system. Due to its higher elevation, drainage of the system still occurs while the tide at open sea already starts to rise. A longitudinal profile of the inlet of De Slufter reveals a threshold between the main frame and open sea (figure 5.4). Water levels must be higher than -0.55 m to -0.5 m NAP before water can enter the channel. Water levels at the North Sea however regularly fall below this level. The mean low water level during the field campaign was located at -0.89 m NAP. During spring tides, water levels dropped to minimum LWS levels of -1.39m NAP. Water depths in the channel, however always remain at least 20 cm. When North Sea water levels fall below the elevation of the channel bottom, tidal forcing loses control on channel water levels. Drainage of the basin still occurs while the North Sea tide already rises again. Only when North Sea water reaches a height of around -0.5 m NAP during the flooding phase, water in the Slufter channel starts to rise as well (figure 5.5).

During neap tide and storm conditions, the minimum water levels are located at higher elevations than the channel bottom, and the effect of truncation is smaller (figure 5.5; left).
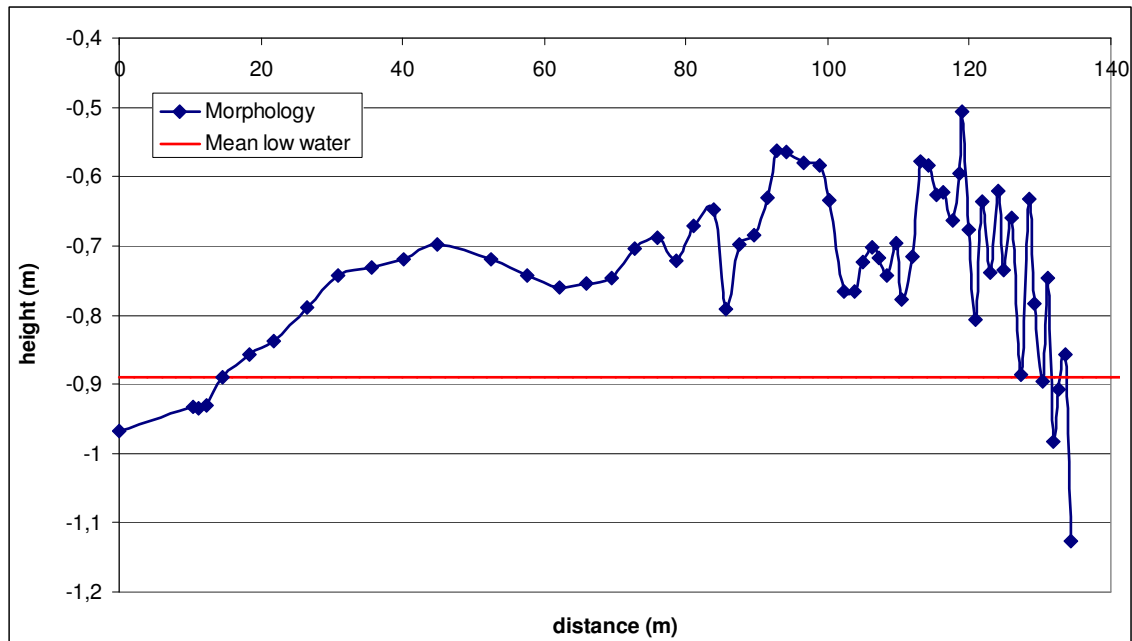
Figure 5.4: longitudinal profile of Slufter channel with mean low water on the North Sea. Maximum channel depths are plotted against distance starting at the most seaward part of the inlet towards the location of the main frame.
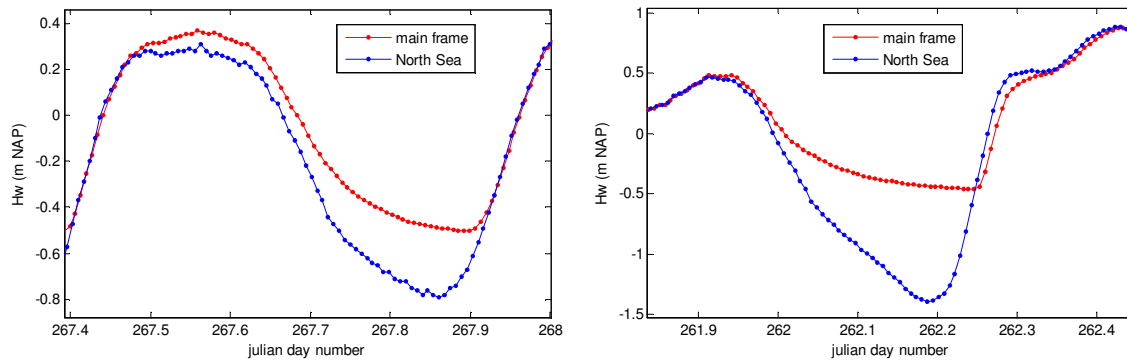
Figure 5.5: water levels at the North Sea and at the channel at the location of the main frame for neap tide (left) and spring tide conditions (right).

5.3 Hypsometry

5.3.1 Digital Elevation Model

ArcGIS software was used to analyse the wet surface area and volume of De Slufter at varying water levels. Points measured by DGPS during the field campaign were merged with data points from the AHN (*Actueel Hoogtebestand Nederland*), a digital elevation model (DEM) covering the whole area of The Netherlands. It contains one measurement every five

square metres, obtained with airborne laser altimetry (LiDAR). The AHN points used here date from 2005. There is a large difference between the present morphology of De Slufter and that of 2005. In 2005, there was a complex morphology with a remnant channel in the uttermost east of the channel mouth area, in which sand was dumped to prevent erosion of the adjacent dunes in the east, and a new active channel in the extreme west of the mouth area. This large difference in morphology made it difficult to merge the two point clouds. Therefore, some imaginary points were added to the DGPS measurements, to improve the conjunction of the two data sets. The *natural neighbour* method was used to interpolate the merged points into a DEM of De Slufter. This interpolation method calculates cell values as a function of inverse distance by averaging the values of cells in the neighbourhood. The cells closest to the cell being estimated, have the largest influence in the averaging process. The *natural neighbor* technique is the only interpolation method in ArcGIS able to handle a large number of input points.

Surfaces areas and volumes can only be calculated from a triangulated irregular network (TIN). In a TIN, bed height is represented by a collection of nodes and lines, building a large set of non-overlapping triangles. The surface area of these triangles can be easily calculated. Therefore the DEM was converted into a TIN, from which calculations could be done. The accuracy of both the DEM and the TIN are discussed in paragraph 6.4.

5.3.2 Hypsometric curve

Using the TIN model, the volume and wet area of the basin are calculated as a function of water level. This was calculated from 0 m NAP onwards, with steps of 10 centimetres, towards 2.5 metres +NAP (table 5.3). This was taken as maximum water level, because at this level almost the entire surface area of De Slufter is covered with water.

H_w (m + NAP)	surface area (m^2)	%sa	d$_{\%sa}$	volume (m^3)	%vol	d$_{\%vol}$
0	147050,0278	3,5037		110188,4423	2,0589	
0,1	168462,5341	4,0139	0,5102	128743,2434	2,4056	0,3467
0,2	186587,5936	4,4458	0,4319	147841,7480	2,7625	0,3569
0,3	206905,8178	4,9299	0,4841	170206,0905	3,1803	0,4179
0,4	241987,8461	5,7658	0,8359	197940,7107	3,6986	0,5182
0,5	268809,3750	6,4049	0,6391	223561,5580	4,1773	0,4787
0,6	304975,0000	7,2666	0,8617	256014,3450	4,7837	0,6064
0,7	345925,0000	8,2423	0,9757	291517,4296	5,4471	0,6634
0,8	409812,5000	9,7645	1,5222	335218,9496	6,2636	0,8166
0,9	558375,0000	13,3043	3,5398	393274,1996	7,3484	1,0848
1	755731,2500	18,0067	4,7024	472260,1694	8,8243	1,4759
1,1	954025,0000	22,7314	4,7247	571788,7942	10,6840	1,8597
1,2	1405850,0000	33,4969	10,7656	720363,4358	13,4601	2,7761
1,3	1959325,0000	46,6845	13,1876	929839,3749	17,3742	3,9141
1,4	2520225,0031	60,0490	13,3645	1200368,3059	22,4291	5,0549
1,5	2932550,0000	69,8734	9,8244	1503427,5137	28,0919	5,6627
1,6	3153575,0070	75,1397	5,2663	1826892,7970	34,1359	6,0440
1,7	3307162,5074	78,7992	3,6595	2164352,9425	40,4414	6,3055
1,8	3468250,0000	82,6374	3,8382	2518342,1177	47,0558	6,6144
1,9	3639000,0051	86,7058	4,0684	2899741,6222	54,1823	7,1265
2	3737150,0083	89,0444	2,3386	3280153,1713	61,2904	7,1081
2,1	3811754,1361	90,8220	1,7776	3668153,6540	68,5402	7,2499
2,2	3875275,0012	92,3355	1,5135	4063101,9420	75,9199	7,3797
2,3	3960725,0060	94,3715	2,0360	4479788,3481	83,7058	7,7859
2,4	4008825,0067	95,5176	1,1461	4888968,2890	91,3514	7,6456
2,5	4196950,0000	100,0000	4,4824	5351825,9096	100,0000	8,6486

Table 5.3: flood simulation with water level (column 1), surface area covered by water at particular water level (column 2), percentual coverage compared to a maximum at 2.5m +NAP (column 3), rate of change in coverage (column 4), volume of water at particular water level (column 5), percentual volume compared to a maximum volume at 2.5m +NAP (column 6) and the rate of change in volume (column 7).

The morphology of De Slufter determines the amount of surface area covered by water in the system. Increasing water levels from below NAP towards 0.8 meter +NAP, the surface area covered by water, does not increase by large amounts. At these water levels, water transport solely occurs inside the channel. A further increase of the water level, floods the channel levees and its adjacent low sloping beaches. These low sloping areas cover large parts of the system. Here, a small increase in water level can result in the flooding of a very large surface area of the basin (figure 5.6; figure 5.9). Nearly 50% of the total increase in wet surface area, occurs between 1.1 m and 1.5 m +NAP (with the coverage at 2.5m +NAP taken as 100%; table 5.3, columns 1-4; figure 5.8). From 1.6 m +NAP onwards, the rate of change decreases again towards much lower values. At this stage the low sloping regions are already filled with water. The water reaches the dune foot where slopes are larger again and an increase in water level will not flood large surface areas (figure 5.6, figure 5.9).
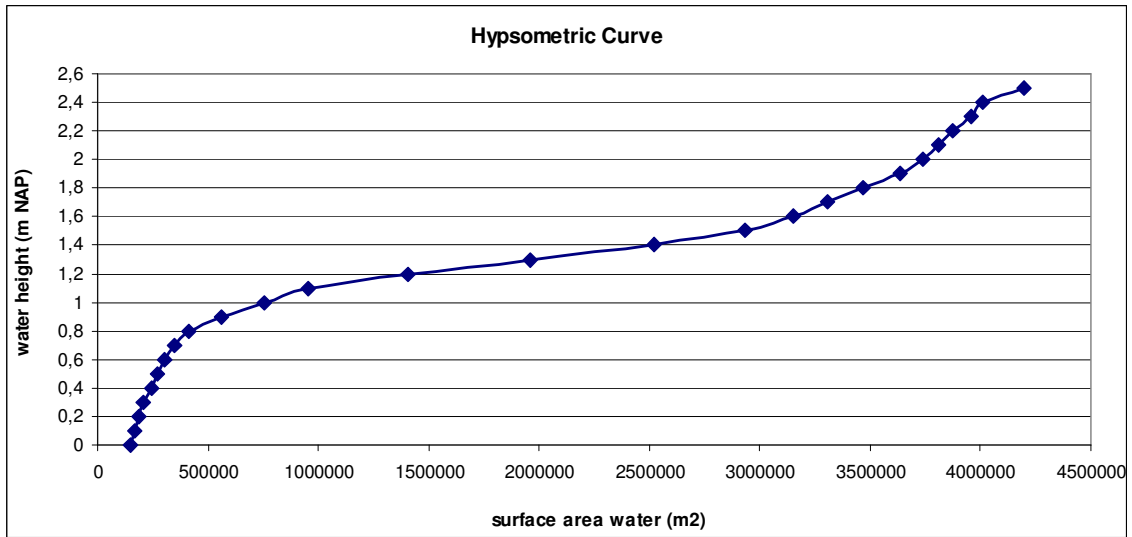
Figure 5.6: relation between surface area covered with water (m^2) and water level (m +NAP) for De Slufter (hypsometric curve).

Figure 5.7: volume of water (m^3) inside the system at different water levels (m +NAP).
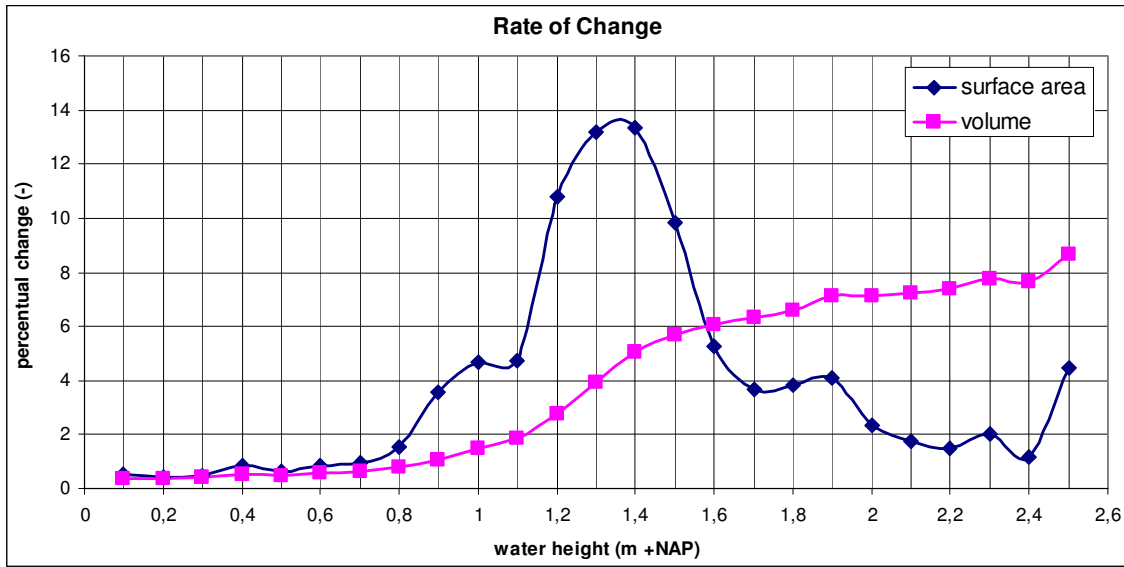
Figure 5.8: rate of change in surface area covered by water and volume (for example: the values at 1.2 m indicate the percentual change from 1.1 m to 1.2 m +NAP).
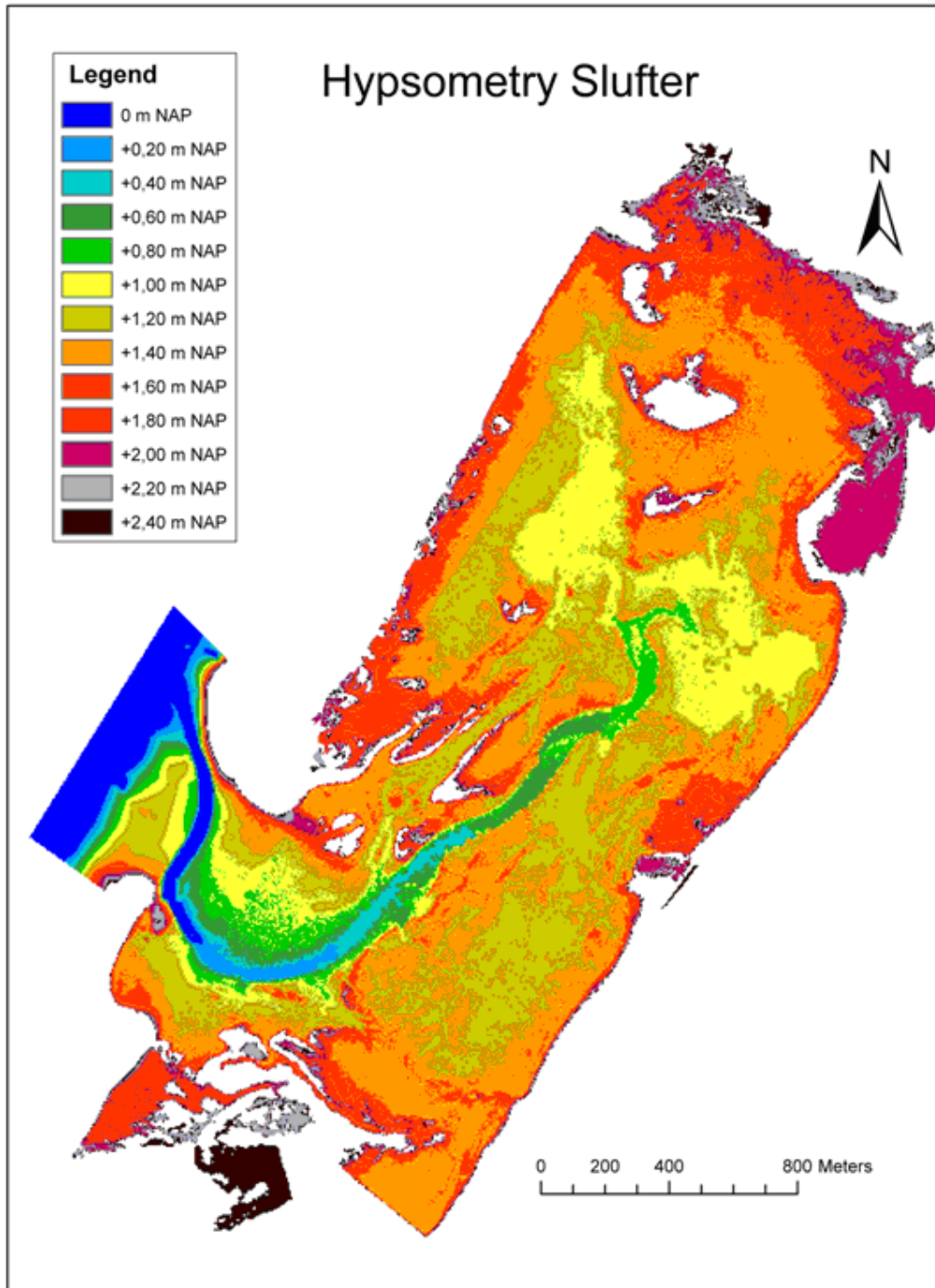
Figure 5.9: hypsometric map of De Slufter with different colors indicating several stages of the flooding process and the relevant surface area covered by water at this particular stage.

5.3.3 Background

Basin hypsometry has a large influence on the behavior of the system, effecting the duration and the occurrence of maximum ebb- and flood current velocities. As explained in section 1.2.4, a strong increase in A_{xy} compared with that of A_c results in an increased

duration of the flood. Because the intertidal area in De Slufter is small, this is not the case for periods of average water levels. This only occurs when the large beach flats are flooded during storm events. The rates of change in A_{xy} and A_c with water level differ significantly (figure 5.10). At small water levels, when the water is restricted to the channel, A_{xy}/A_c is more or less constant. From 0.9 m onwards the beach flats are flooded. A_{xy} increases much faster than A_c and A_{xy}/A_c peaks at 1.2 m. From then on, A_{xy}/A_c decreases again. At 2.1 m A_{xy}/A_c has comparable values with conditions during water levels of 0 - 0.7 m. During storm events and spring tides, when water levels up to 1.4 m were reached, the duration of the flood phase increases compared to normal conditions (see 1.2.4).
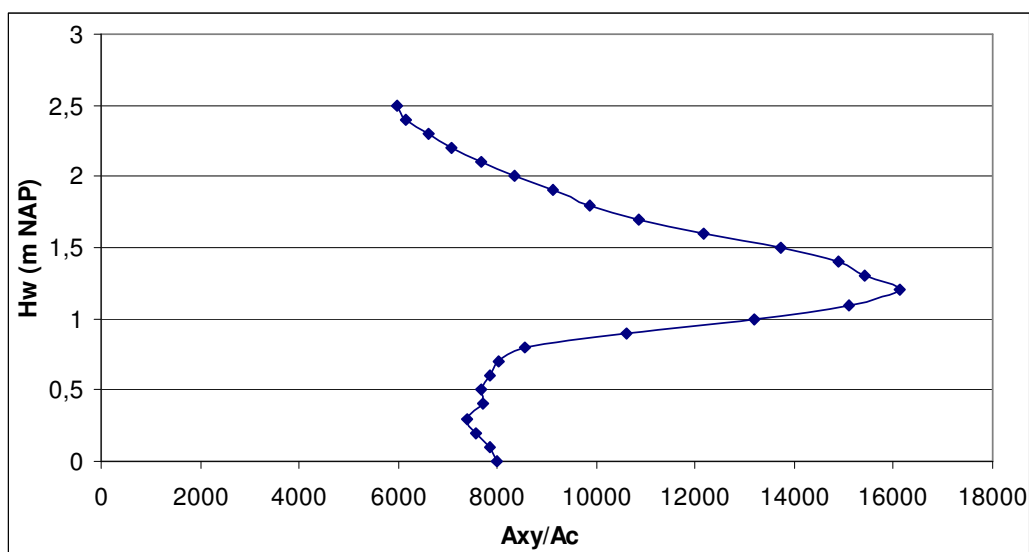
Figure 5.10: A_{xy}/A_c for different water levels.

5.3.4 Comparison with larger basins

The much larger basins of the Wadden Sea have a completely different morphology (Dronkers, 2005). The basin of De Slufter is elevated at a much higher level, compared to the basins of the Wadden Sea. These basins have a much larger amount of intertidal flats in relation to De Slufter (figure 5.11). The majority of these intertidal areas is located below mean sea level. This is especially the case for the Texel inlet where more than half of the tidal flats are subtidal. Assuming a tidal wave with water levels ranging between -1m and +1m NAP, 45% (Ameland Inlet) to 78% (Texel Inlet) of the cross sectional surface area is covered with water during LW, compared to less than 3% in De Slufter. At HW the Wadden basins are completely covered with water (~100%), implying an intertidal surface area of 22% (Texel Inlet) to 55% (Ameland Inlet) of the maximum cross sectional area (figure 5.11). This is however an overestimation of the average situation since a tidal range of 2 m will only be reached during spring tidal conditions. 18% of the cross sectional surface area of De

Slufter is covered with water at water levels of +1m NAP (table 5.3), indicating an intertidal surface area of 16%. Because the amount of intertidal flats is larger for the Wadden Basins, compared with De Slufter, A_{xy} increases rapidly with water level. The growth in A_c will be smaller. The parameter A_{xy}/A_c will therefore increase with water level for the Wadden basins. For De Slufter, this parameter remains more or less constant until a water level of 0.8 m +NAP (figure 5.10). This indicates that, under normal conditions, the Wadden basins experience a longer flood duration compared to De Slufter.
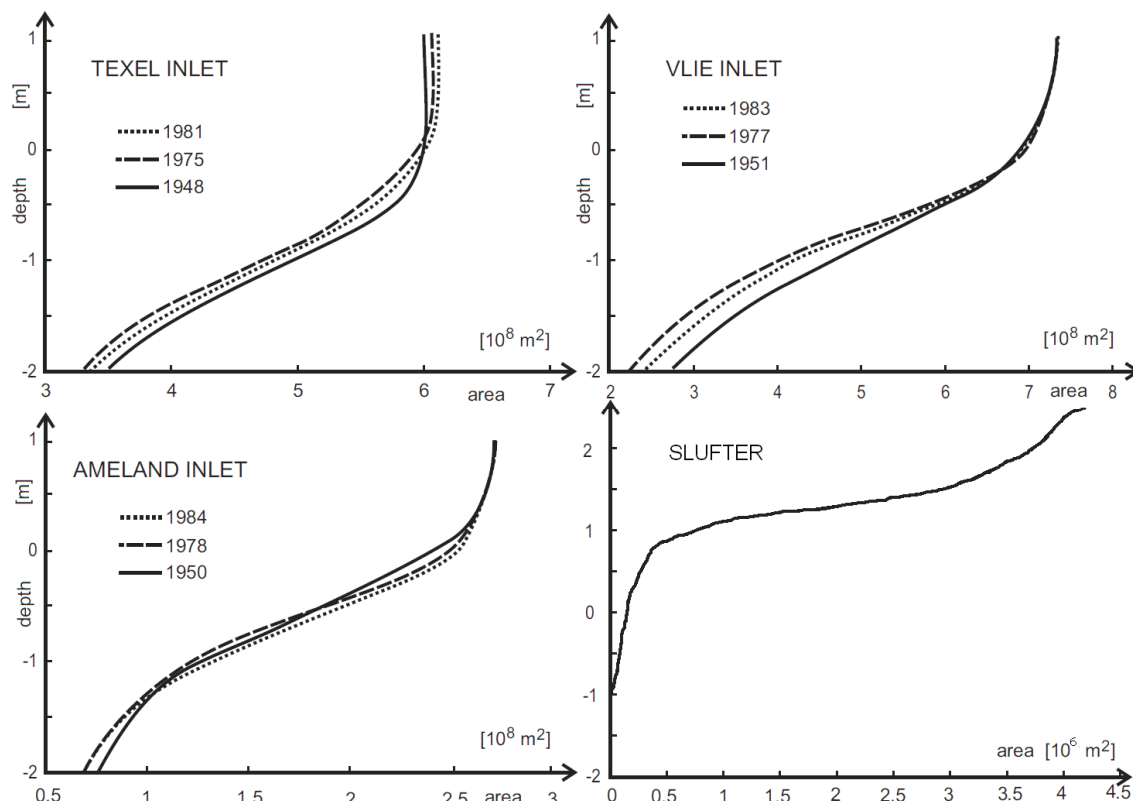
Figure 5.11: hypsometric curves for three large tidal basins (Texel Inlet, Vlie Inlet and Ameland Inlet) of the Wadden Sea at different periods and for De Slufter (right, lower). Hypsometry of the Wadden basins after Dronkers (2005).

5.4 Hydrodynamical characteristics

In the following sections several hydrodynamical characteristics measured (or derived from measurements) in De Slufter will be discussed. Flow velocities measured at a height of 25 cm above the bed (v), water level (H_w), water volumes (V_b), cross-sectional areas (A_c), wet surface areas (A_{xy}) and the variation of water level with time (dh/dt) all vary with changing conditions. First, these parameters will be analyzed during a tidal cycle with a flood and an ebb phase (5.4.1; 5.4.2). Second, the values of these parameters during storm conditions are analyzed (5.4.3).

5.4.1 Flood

Starting at LW, volume and cross-sectional area are small while dh/dt, forced by the North Sea tide, and velocity starts to increase rapidly (figure 5.12, figure 5.13). Maximum flood velocities are reached somewhat after maximum dh/dt-values are reached, but differences are small. The average delay with maximum values of dh/dt is 27 minutes. Based on velocity measurements u_{max} on average occurs 1h25 after LW.

Water levels in the channel continue increasing, but the rate of rising stagnates. As the velocity follows the pattern of decreasing dh/dt, velocities also decrease. Subsequent velocity patterns differ, depending on maximum water level reached. During spring tidal conditions a second peak in flood velocities can be observed, also visible in dh/dt (figure 5.13). This peak is most pronounced at large maximum water levels and is the result of the creation of the overtides of M_2 (mainly M_4 and M_6). Velocities increase again, but peak velocities do not reach levels reached earlier on. During neap tides, velocities decrease after peak velocities are reached on towards HW (figure 5.12).

5.4.2 Ebb

After HW the flow direction reverses. Again forced by the North Sea tide, dh/dt starts to increase, but rates and maximum values are smaller compared with the flooding phase. Maximum ebb velocities are slightly more in phase with maximum values of dh/dt, compared with the flooding phase. There is an average delay of 16 minutes between maximum ebb velocities and maximum dh/dt. Water levels at dh/dt_{max} (0.29m +NAP) are higher than those during flood (0.02m +NAP). It follows from equation 1.19 that this indicates slightly larger values for A_c and V_b, but this will not affect velocities to a large degree. Peak ebb velocities are comparable to peak flood velocities (figures 5.12 and 5.13).

On average 2h07 after HW, maximum velocities are reached. This is about the moment truncation of the tidal wave in the channel of De Slufter starts (figure 5.5). The water of the North Sea falls faster than water in the channel. Therefore dh/dt in the channel never reaches values comparable with the flooding phase.
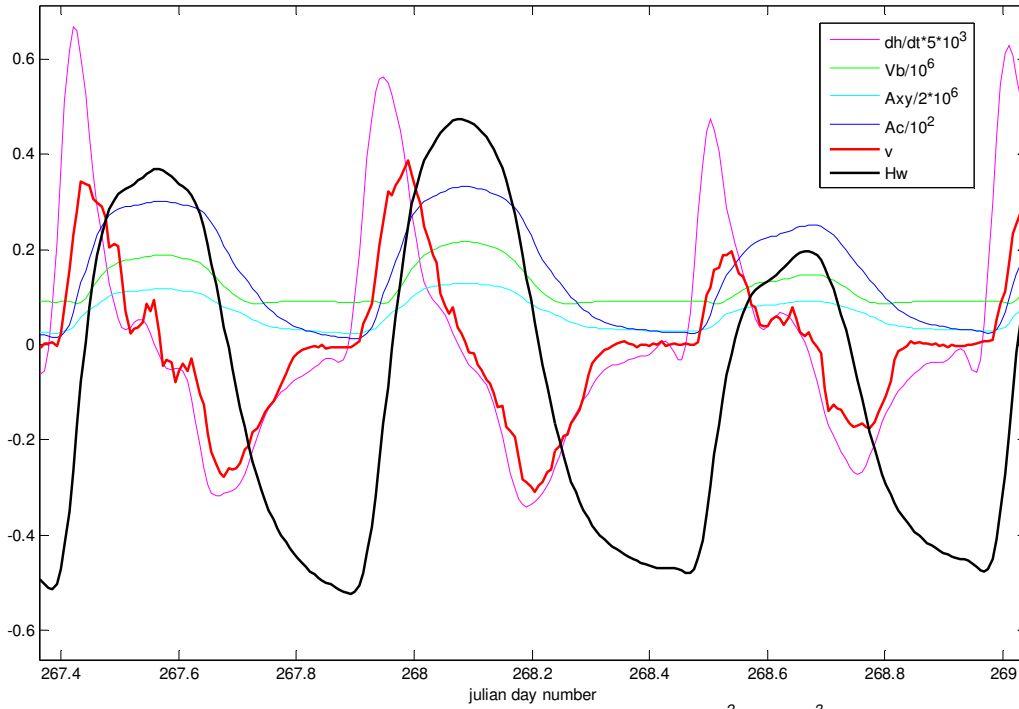
Figure 5.12: several parameters for neap tidal conditions including Ac (m², Vb (m³), Hw (m NAP), dh/dt (m/s) and measured velocities (m/s).
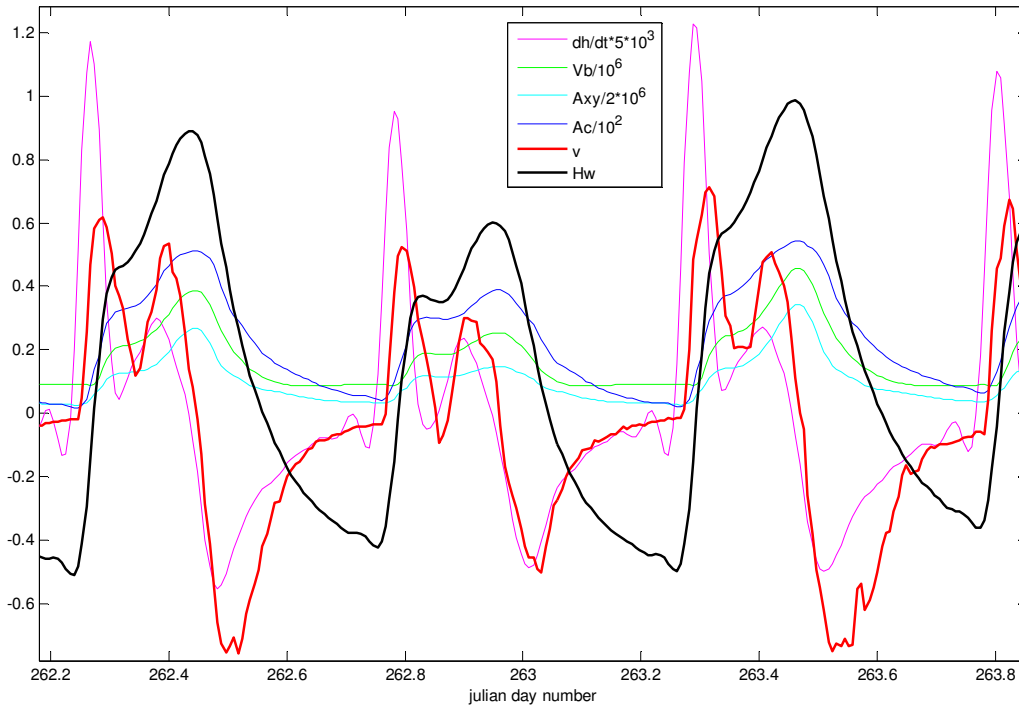
Figure 5.13: several parameters for spring tidal conditions including Ac (m², Vb (m³), Hw (m NAP), dh/dt (m/s) and measured velocities (m/s).

5.4.3 Storm-conditions

During storm conditions, there are large differences between the flood and the ebb phase (figure 5.14). Increased water levels due to wind- and wave set-up do not result in increased values for dh/dt during the flood phase, compared to normal conditions. Values are comparable to spring tidal conditions. Average peak velocities are 0.97 m/s (table 5.4). During the storm, large areas of the beach flat become inundated at water levels around 1.0 m - 1.1 m +NAP. The horizontal surface area (A_{xy}) increases rapidly and the ratio A_{xy}/A_c becomes larger (A_c; figure 5.10 & 5.14). Because this occurs just before HW, dh/dt and therewith velocities are small (around zero) and remain small until drainage of the beach flats starts. Water levels on the beach flats are small, which will increase friction. The duration of the flood phase increases significantly compared to normal conditions. Duration asymmetry decreases from -26.6% during normal conditions to -6.5% during storm conditions. The North Sea water level however drops undisturbed, creating larger pressure gradients between the flats and the channel. This mechanism results in average peak ebb velocities (1.99 m/s) twice as large as peak flood velocities (table 5.4).
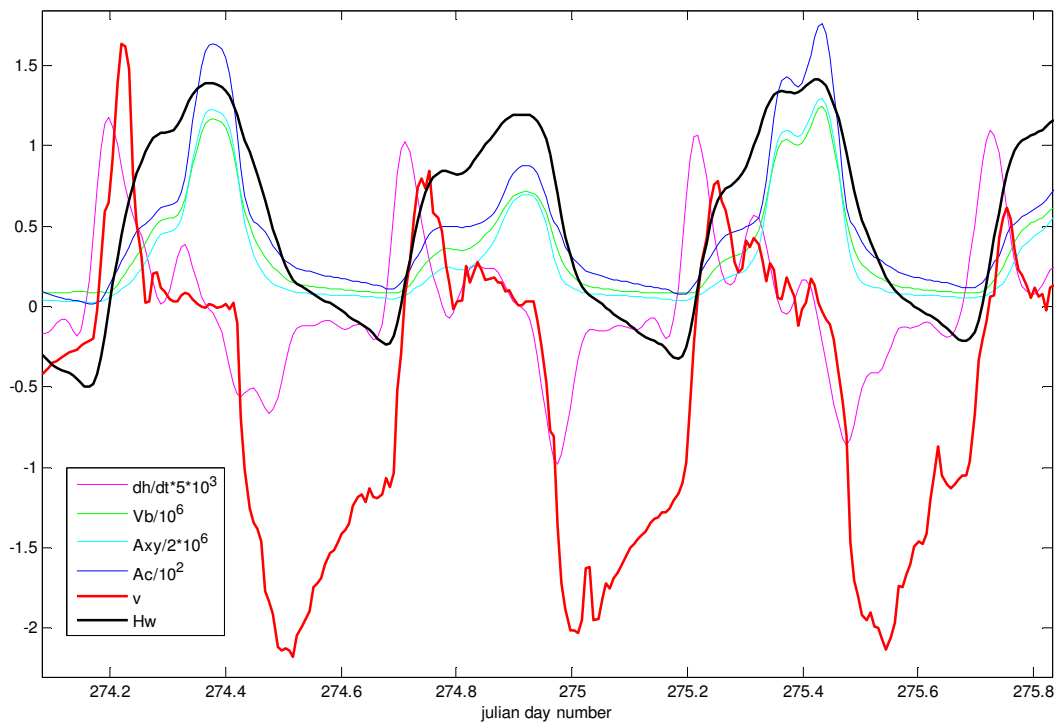
Figure 5.14: several parameters for storm conditions including Ac (m^2), Vb (m^3), Hw (m NAP), dh/dt (m/s) and measured velocities (m/s).

There is a circulation pattern inside De Slufter during storm events. When the beach flat gets inundated starting at water levels of ~0.9 m NAP, channel velocities rapidly drop to much lower values (figure 5.15). The water entering De Slufter is not confined to the channel

anymore. The largest amount of water entering the basin now flows over the beach flat, rapidly increasing the wet cross sectional area. As water depths on the beach flat are much smaller than water depths in the channel, velocities on the flat exceed those inside the channel. As HW is reached velocities reverse. As can be seen from figure 5.15, water levels and flow velocities on the beach flat rapidly decrease to values around zero. Outflow from the basin towards the North Sea occurs through the channel. Peak ebb velocities are much larger than maximum flood velocities.
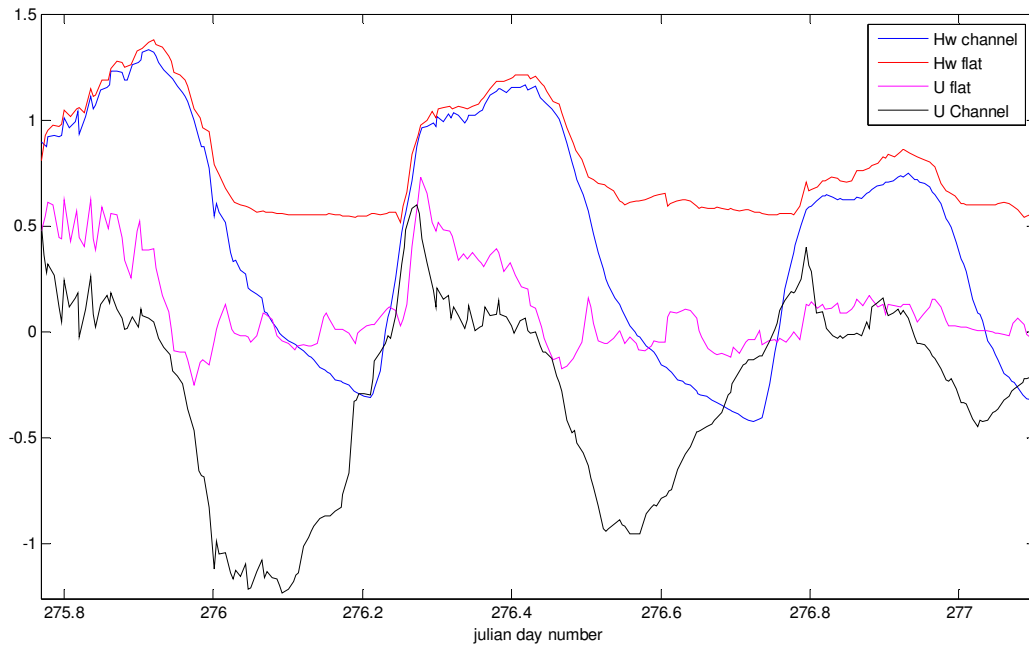
Figure 5.15: comparison between Hw and velocities (10 min. averages) at the channel (main frame) and at the beach flat for three tidal cycles during storm conditions.

Tide nr	t_{max}	Hw_{max}	t_{min}	Hw_{min}	ΔD	$U_{max\text{-}flood}$	$U_{max\text{-}ebb}$	dh/dt_{max} $*10^{-4}$	dh/dt_{min} $*10^{-4}$	AC_{max}	Axy_{max} $*10^{5}$
1	261,93	0,51	262,24	-0,51	-23,29	0,47	-0,51	2,06	-1,15	51,07	5,37
2	262,43	0,89	262,75	-0,42	-24,32	0,62	-0,76	2,71	-1,28	34,57	2,66
3	262,95	0,60	263,26	-0,50	-21,62	0,52	-0,50	2,20	-1,13	51,04	5,35
4	263,46	0,99	263,77	-0,36	-23,29	0,71	-0,75	2,84	-1,15	38,87	2,94
5	263,97	0,76	264,29	-0,42	-22,67	0,67	-0,56	2,49	-1,17	54,37	6,89
6	264,49	0,82	264,80	-0,40	-23,29	0,59	-0,63	2,56	-1,23	47,25	4,01
7	265,00	0,58	265,32	-0,47	-24,32	0,51	-0,46	2,25	-1,12	49,20	4,54
8	265,51	0,78	265,82	-0,47	-28,57	0,57	-0,58	2,53	-1,10	37,97	2,87
9	266,00	0,67	266,35	-0,50	-32,47	0,48	-0,49	2,36	-1,09	48,00	4,19
10	266,53	0,55	266,86	-0,51	-30,56	0,47	-0,43	2,11	-0,98	42,83	3,32
11	267,03	0,58	267,39	-0,51	-32,47	0,53	-0,39	2,02	-0,93	36,46	2,77
12	267,57	0,37	267,89	-0,52	-27,03	0,34	-0,28	1,55	-0,74	37,95	2,87
13	268,08	0,47	268,47	-0,48	-31,77	0,39	-0,31	1,30	-0,79	30,18	2,35
14	268,67	0,20	268,97	-0,48	-19,44	0,20	-0,18	1,09	-0,63	33,24	2,58
25	274,37	1,39	274,68	-0,24	-12,82	1,64	-2,18	2,73	-1,53	49,48	4,64
26	274,91	1,20	275,18	-0,33	-5,41	0,84	-2,03	2,37	-2,26	163,94	24,54
27	275,43	1,42	275,68	-0,22	-1,41	0,78	-2,13	2,47	-1,99	87,84	13,96
28	275,92	1,43	276,20	-0,28	-6,67	0,62	-1,63	2,54	-1,50	176,25	25,88
AV_{normal}		0,63		-0,47	**-26,59**	**0,51**	**-0,49**	2,15	-1,03	42,36	3,77
AV_{storm}		1,36		-0,26	**-6,55**	**0,97**	**-1,99**	2,53	-1,82	119,38	17,26

Table 5.4: parameters from spring tide (tide nr. 1) to neap tide (tide nr. 14) and during storm conditions (tide nr. 25-28) and averages, including maximum and minimum water levels (m +NAP), duration asymmetry ΔD (%), maximum ebb- and flood velocities (m/s), maximum and minimum dh/dt (m/s), cross sectional surface area (m^2) and horizontal surface area (m^2). Normal conditions are indicated in green going from spring tide (tide nr. 1) towards neap tide (tide nr. 14) and storm conditions in orange.

5.5 Sediment transport

5.5.1 Bed load transport

As can be seen in the previous paragraphs there is a large negative duration asymmetry in De Slufter as a combined result of an external asymmetry, tidal truncation and a hypsometry effect. It can be expected that this would lead to much larger peak velocities during flood than during ebb, resulting in a strong flood-dominated bed load transport. This is however not the case. Velocities are rather small during fair weather conditions and peak flood velocities are therefore only slightly higher than peak ebb velocities. The amount of bed load transport is strongly dependant upon the flow velocity. An approximation of the bed load transport is achieved when bed load transport is estimated as the third power of the flow velocity (see equation 1.12):

$$\langle q_b \rangle \approx \left(u^3 \right) \tag{5.1}$$

Equation 5.1 is an approximation of equation 1.12, which could not be used, because several parameters (friction factors) are unknown. For every tidal cycle (ebb and subsequent flood stage) during the period from day 262.00 to day 275.76 the net bed load transport is calculated with equation 5.1 and plotted against the maximum water level reached during the associated flood stage in figure 5.16. The net bed load transport is plotted as a fraction, f, of the (absolute) maximum transport reached during the period between day 262.00 and day 275.76:

$$f = \langle q_b \rangle / \langle q_b \rangle_{max} \tag{5.2}$$
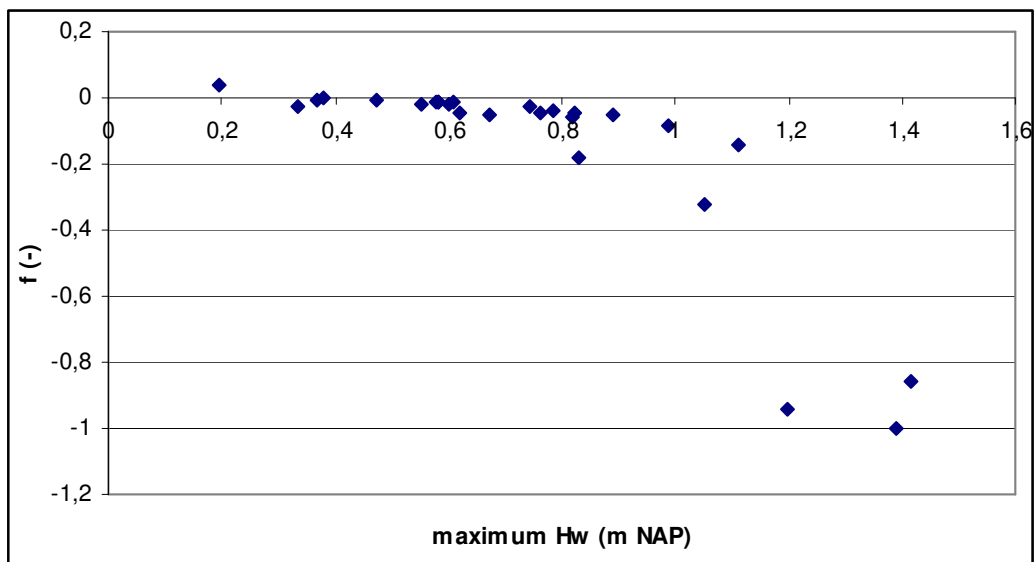
Figure 5.16: bed load transport fraction f, where f is defined as the net bed load transport during each tidal cycle (ebb phase and subsequent flood phase) divided by the maximum value reached during this period (equation 5.2). f Is plotted against the maximum water level reached during the associated flood phase.

During normal conditions, with maximum water levels between 0.2 m and 1.0 m +NAP, the net bed load transport appears to occur in the ebb direction. This ebb dominance is however weak, because differences between ebb- and flood-transport are small. This could already be seen from table 5.4, where maximum ebb ($U_{max-ebb}$) and flood velocities ($U_{max-flood}$) are shown. During normal water levels the averages of $U_{max-ebb}$ and $U_{max-flood}$ over a neap-spring tidal cycle are almost equal with respectively -0.486 m/s and 0.505 m/s.

The average bed load transports for both the ebb stage and the flood stage during a neap-spring tidal cycle (day 262.00-269.18) and during storm conditions (day 274.02-276.00) were calculated using equation 5.1 (table 5.5). The measured velocity signal reveals a small ebb dominated behavior over a neap-spring cycle, with nearly 5% more bed load transport during the ebb phase than during the flood phase. During storm conditions the bed load transport becomes strongly ebb-dominant. This can also be seen in figure 5.16. The net bed

load transport, when maximum water levels range between 0.2 - 1.0 m +NAP, is on average only 4.1% of the average net bed load transport during water levels of 1.2-1.5 m +NAP. The average $U_{max-ebb}$ (-1.993 m/s) during the storm event is also much larger than the average and $U_{max-flood}$ (0.971 m/s; table 5.4).

Fraction of transport	flood	ebb
measured N-S cycle	0.4556	0.5444
measured storm	0.1398	0.8602

Table 5.5: fraction of sediment transport during the flood and ebb phases for measurements and model results. Distinction is made between the average fraction during a neap-spring (N-S) tidal cycle (day 262.00-269.18) and the average fraction during the storm event (day 274.02-276.00).

The values of table 5.5 however should be analyzed with caution, because there are other factors than velocity that play a role in determining the bed load transport (see 1.2.4). It is however clear that during normal conditions, differences between bed load transported during flood and ebb are small.

5.5.2 Suspended load transport

The duration of slack tides plays an important role in the transport of very fine suspended material (section 1.2.4). During storm conditions there is a large difference with normal conditions in the duration of the slack tides (figure 5.14). This will influence suspended load transport fluxes. During calm weather conditions, the duration of HWS is usually very small. When slack tide is defined as the period with velocities between -0.10 and 0.10 m/s, HWS duration is usually less than 10 minutes. Flow direction reverses and velocities rapidly increase again. The duration of LWS is on the other hand much larger. As water levels in the channel decrease slowly towards LWS due to the truncation mechanism, velocities also gradually decrease near values around zero. This is particularly obvious during neap tide (figure 5.12). For example for tide number 14 and 15, the duration of LWS is 3h50. When slack duration differences are used as an indication for the transport of suspended material, this implies the system should demonstrate a net export of fine material out of the system. During storm-events the pattern is more complicated. The pattern seems to be reversed (figure 5.14). There is no real LWS, with durations less than 10 minutes. HWS duration increases up to maximum lengths of 2u50 (tide number 25) inside the channel. This is related to the circulation pattern mentioned in section 5.4.3. Channel velocities rapidly drop when the beach flat is inundated. An increased HWS duration would indicate a net import of suspended material during storm-events. Due to the complexity of this circulation and other factors influencing the total suspended load flux, these results should be analyzed with caution. Sediment transport patterns in the Slufter channel are discussed in much more detail in the MSc Thesis of Kramer (2009).

5.6 Hydrodynamical model

5.6.1 Theory

A simple hydrodynamical model was used to simulate flow velocities in the channel of De Slufter. This model assumes a uniform water level in the basin. Since basin volumes as a function of varying water level $(\partial V_b / \partial h)$ are determined accurately for De Slufter (see 5.3), equation 1.19 can be expressed as:

$$u = \frac{1}{A_c} \frac{\partial V_b}{\partial t} = \frac{1}{A_c} \frac{\partial V_b}{\partial h} \frac{\partial h}{\partial t} \tag{5.3}$$

where Ac is the cross-sectional area of the entire inlet.

This equation was used to model cross-sectionally averaged velocities. By comparing these simulations with measured velocities we are able to study the importance of hypsometry and possible other processes in determining channel velocities. The measured velocities used in this analysis are measured at the main frame, at a height of 25 cm above the bed. No comparison can be made with velocity measurements from other heights, because these measurements appear to be unreliable, especially during storm conditions. The measured velocities will often not represent the cross-sectionally averaged velocities, creating deviations between model results and measurements. The implications of this will be discussed in section 6.4.

In this model measured values of $(\partial h / \partial t)$ could not be used, because this signal is too irregular. The spikes in the signal lead to large temporary increases in $(\partial h / \partial t)$. This will result in overestimated velocities. To avoid this, the tidal signal was reconstructed using the Wavelet Transform (5.1.1). This reconstructed signal appears to be smoother than the measured water level, and therefore better suited to use in the model. The reconstructed signal contains the constituents M_2, M_4, M_6 and M_8.

Basin volumes were not calculated for water levels below 0 m NAP. Since these volumes need to be known as input for the model, linear interpolation was used for these values. The water level must be at least 30 cm above the pressure sensor to correctly display values for dh/dt. Therefore values for dh/dt under -0.3 m NAP are not taken into account in the model. This explains the gaps in figures 5.17 and 5.18 for modelled velocities just before and after LW.

5.6.2 Model results:

Normal conditions

Velocities were modeled with equation 5.3 and compared with measured velocities. Model velocities are of the same order as real velocities and phases most of the times agree. There are however also some differences between the two. Differences are largest during the flood stage, when the model overestimates peak velocities. This overestimation is largest during spring tides. Especially during spring tide, the flood phase is often characterized by two velocity peaks (figure 5.18): a large peak early during the flood stage and a smaller peak just before HW. This pattern is modeled correctly by equation 5.3. Deviations between measurements and model results are much smaller during the ebb phase. Peak velocities are simulated very accurate by the model (figure 5.17; figure 5.18).
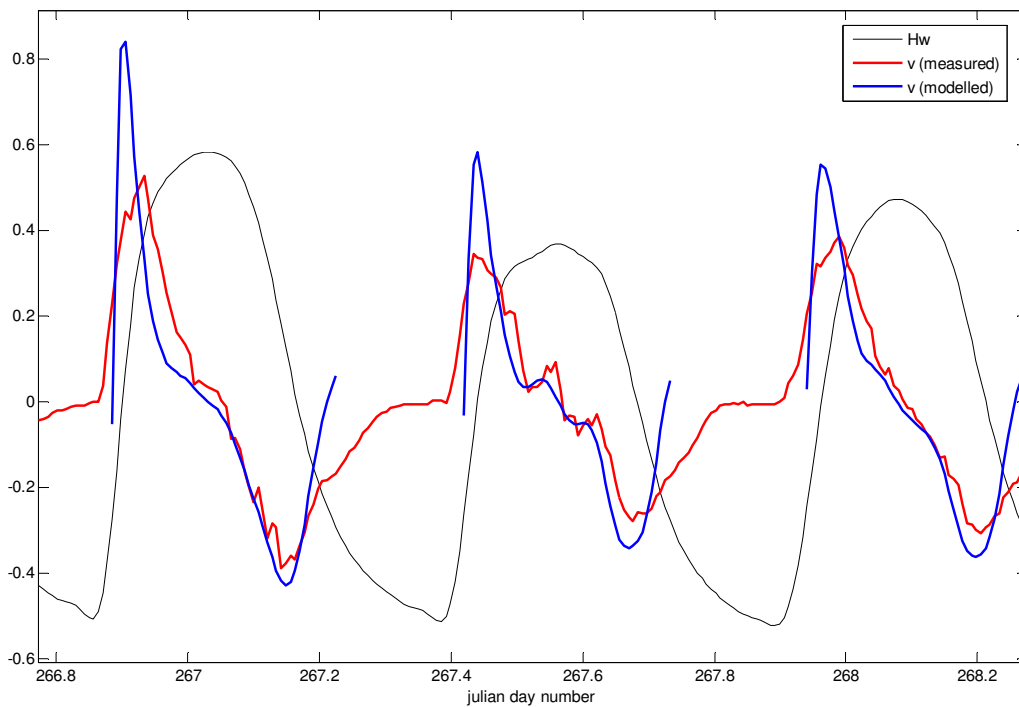
Figure 5.17: modeled and measured velocities during neap tidal conditions.
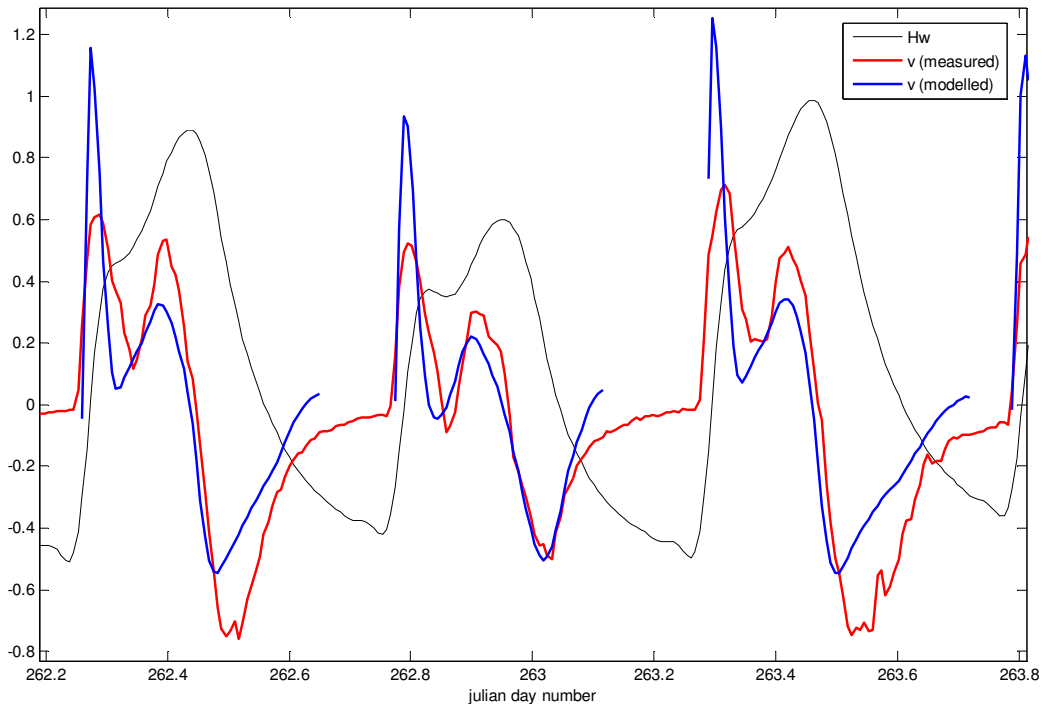
Figure 5.18: modeled and measured velocities during spring tidal conditions.

Storm conditions

Differences between model results and measurements are particularly large during storm events (figure 5.19). Equation 5.3 predicts a second peak in velocities during flood. After the first peak is reached, velocities peak again when the large areas of the beach flat get flooded when water levels become 1.1m +NAP and higher. During these periods A_{xy}/A_c increases rapidly (figure 5.10). In reality this second peak in flood velocities is much smaller or does not appear at all. This is probably related to the fact that the beach flat takes over a large part of the water transport at water levels of 1.1 m + NAP and higher (see section 5.3). In this case, A_{xy} and A_c used in the model will not represent reality and the assumptions behind the model are not valid anymore. Model results will be incorrect. When the beach flat is flooded, velocities in the channel rapidly drop (figure 5.15) and a second peak in velocities will not occur. On average, peak flood velocities more or less agree with measured maximum speeds. This is not the case during ebb. The model largely underestimates measured velocities. Velocities reach more than -2 m/s, whereas the model only predicts peak velocities of -1 to -1.5 m/s. The model predicts a weak ebb dominated bed load transport during storm-events whereas the system appears to be strongly ebb dominant in reality. There is also a large difference in the duration of the ebb phase between measurements and the model.
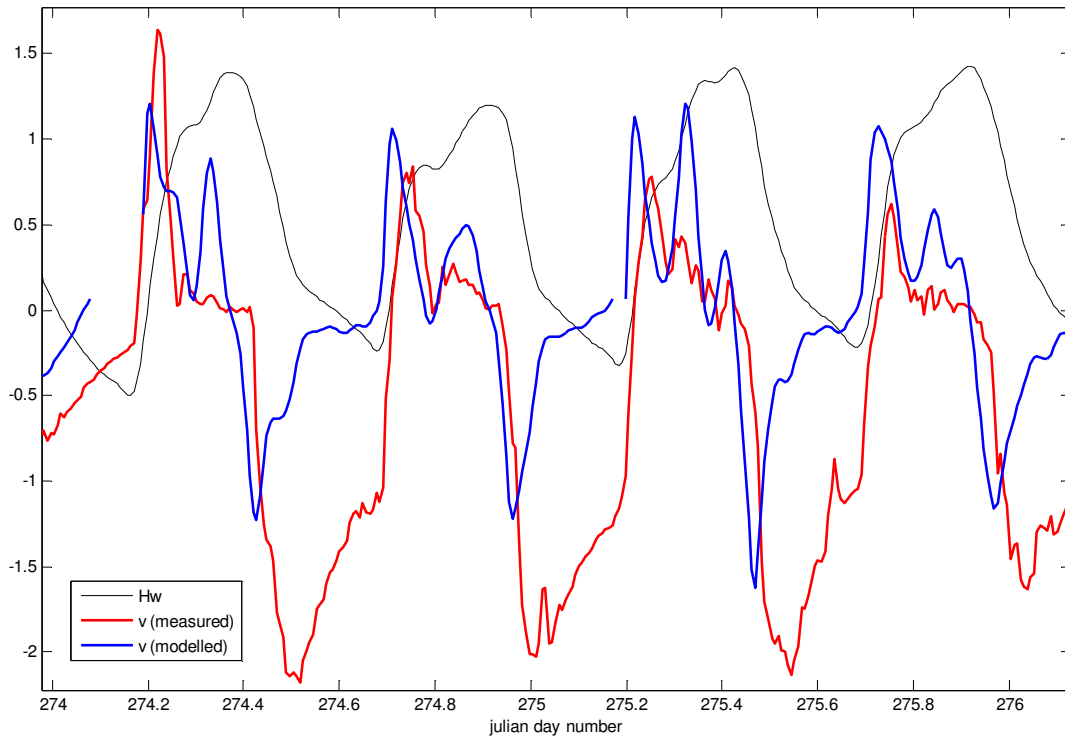
Figure 5.19: modeled and measured velocities during storm conditions.

Bed load transport

The modeled velocity signal was also used to predict net bed load transport directions with equation 5.1 (table 5.6). The predictions were compared with net bed load transport directions derived from the measured velocity signal (table 5.5) to determine the accuracy of the model in predicting the bed load transport. During storm conditions the model does not simulate bed load transport correctly. The model simulates an almost symmetrical bed load transport, with comparable amounts of bed load transport during the ebb and flood stages. Bed load simulations for the neap-spring tidal cycle show a better correspondence with results from measurements. A very weak ebb dominant behavior is simulated.

Fraction of transport	flood	ebb
modelled N-S-cycle	0.4994	0.5006
modelled storm	0.5015	0.4985

Table 5.6: same as table 5.5, but for model results.

6. Discussion

6.1 Inlet stability

Durieux (2004) applied the approach of Bruun and Gerritsen (1960) involving morphological stability (section 1.2.2) to De Slufter. A value of 0.4 was found for the ratio Ω (tidal prism per spring tidal cycle) / M (yearly longshore transport entering the inlet) indicating a very unstable situation. M was probably overestimated ($1 \cdot 10^6$ m^3), but even decreasing this value by one or two orders results in relative unstable conditions. De Slufter exists for more than 150 years in its present state, indicating an equilibrium situation. So, apart from some questionable aspects about this theory mentioned in section 1.2.2, this approach is not applicable to small inlet systems like De Slufter. Good results in predicting inlet stability were achieved for large systems, but the tidal prism of De Slufter is apparently too small to use this method in this case.

The empirical relationship of Townend (2005) between tidal prism and cross-sectional inlet area (below mean sea level; MSL) was mainly used for much larger systems. Spring tide data from De Slufter however fits reasonably well with the lower regression line (HH-C) in figure 6.1. This regression line groups the inlets that approach dynamic equilibrium most.
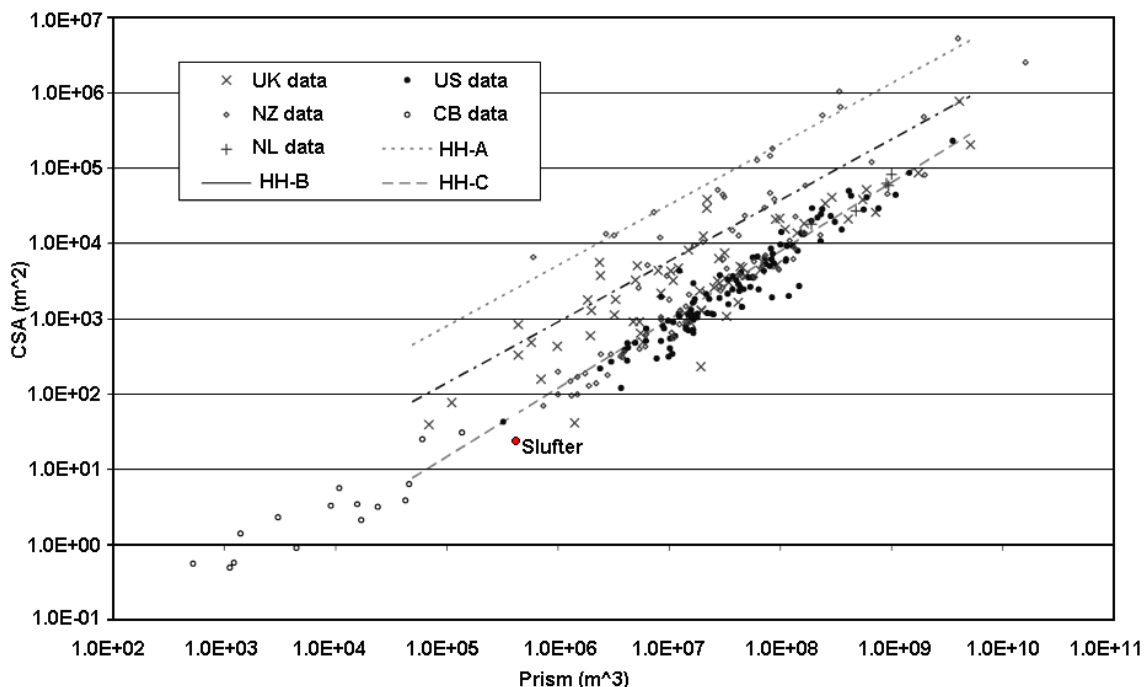
Figure 6.1: relation between tidal prism and cross-sectional area for De Slufter against UK, US, New Zealand, and Dutch data (after Townend, 2005).

Van de Kreeke (1990) used the same approach and related tidal prism to cross sectional area for some stable inlets at the west coast of Florida. A relation of:

$$A = 1.18 \cdot 10^{-4} P^{0.97}$$ (6.1)

was found. Lam (2003) used this relation to identify stable inlets in Vietnam (figure 6.2). It appears that the deviation from this regression line for De Slufter is again not very large, and in between the 95%-confidence limits. When a spring tidal prism of 436292 m^3 is used, equation 6.1 predicts a cross sectional area of 34.87 m^2 whereas a cross-section of 23 m^2 below MSL was measured. With a deviation of 34% this indicates that the difference between prediction and reality is still large, but within the 95% confidence limit. It is however uncertain whether or not the inlet was in equilibrium with the hydrodynamical conditions at the moment when the cross-sectional area was measured.
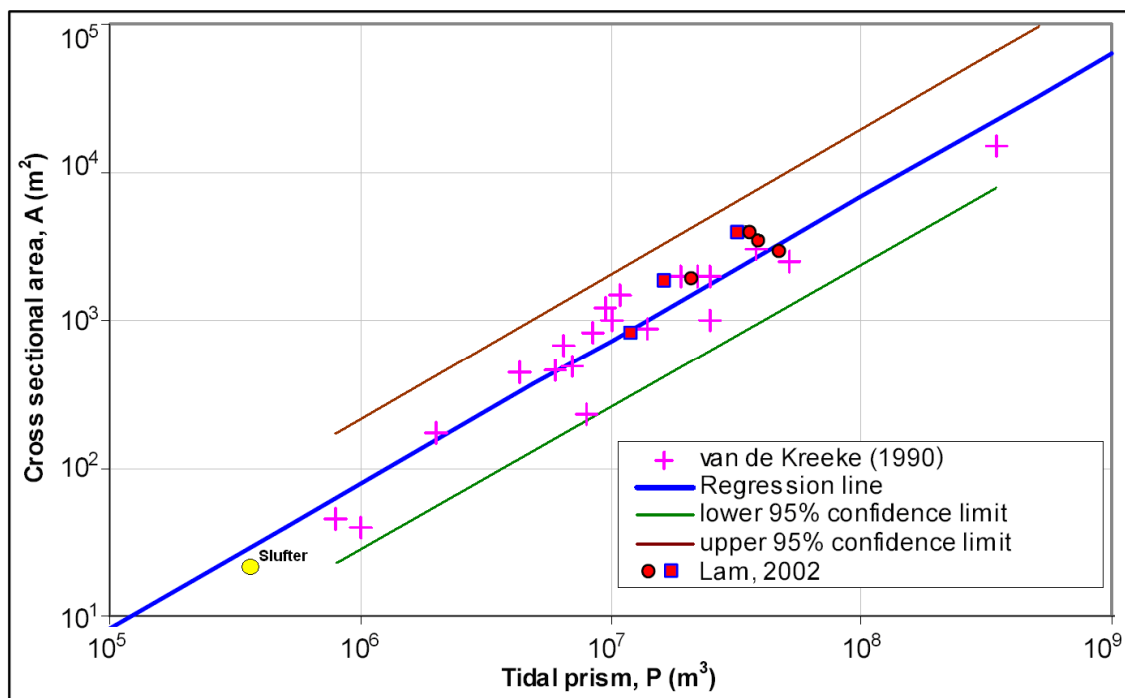
Figure 6.2: relation between tidal prism and cross-sectional area during MSL for De Slufter against data from stable inlets of van der Kreeke (1990) and Lam (2003).

6.2 Morphology

Cross-sectional area

No quantitative analysis is made of bed load transport amounts. However, the net bed load transport ratios, derived from velocities in the channel of De Slufter indicate a strong ebb dominated behaviour during storm events (section 5.5.1). Cross sections of the inlet also indicate a storm induced increase of the cross sectional area. This can be seen in figure 6.3 where the cross sectional areas of the entire inlet are plotted.
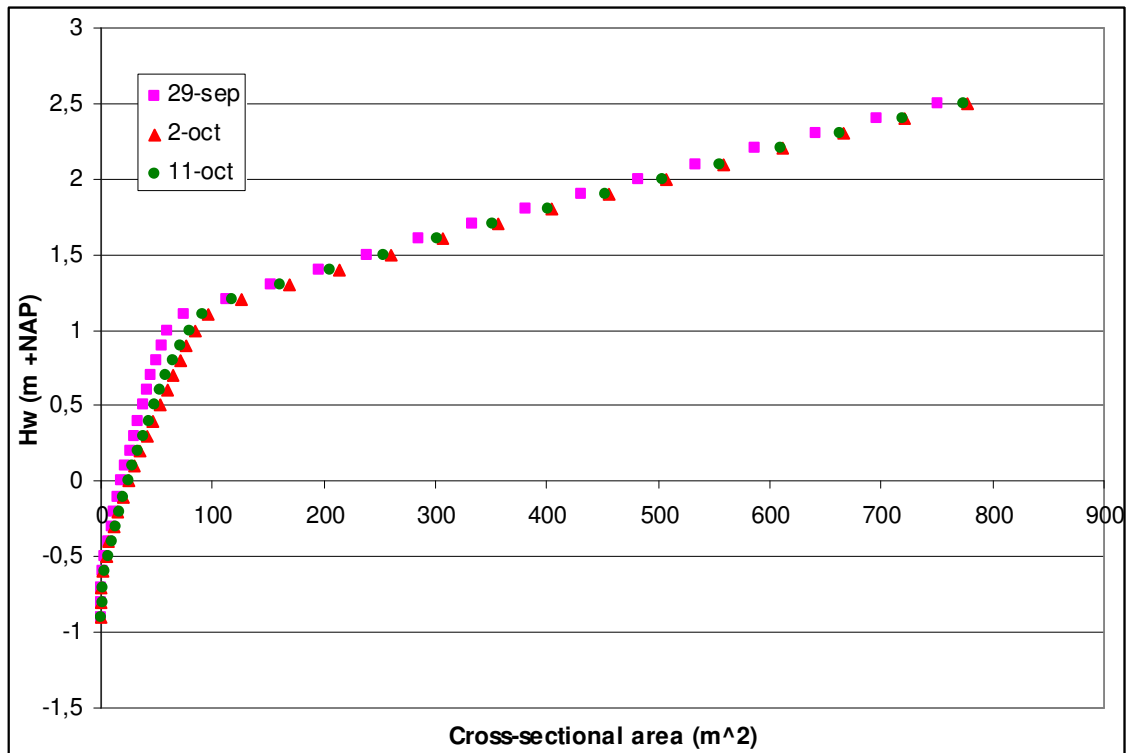
Figure 6.3: Cross-sectional areas of the inlet of De Slufter from the dd-profile, for 29-09 (pre-storm), 02-10 (between two storms) and 11-10 (post-storm) at different water levels.

The largest part of the increase in cross section already occurred during the first storm event (02/10). After the storm period (11/10) the cross sectional area decreased to a small degree, but differences are small. The influence of the second storm event on morphology appears to be smaller than that of the first event. This is possibly related to the slightly longer duration of the first storm event compared to the second event. There is also a small difference in the average direction of wave incidence between the two storm events (table 6.1; figure 6.4). During the first storm event the waves came more from the North (338.1°) compared to the second event (325.2°). The wave direction of incidence during the first event was nearly parallel to the orientation of the channel. During the second event the direction of incidence was more oblique with respect to the channel orientation. Wave angles are however measured offshore and will probably differ from the situation in De Slufter. The profile measurement after the second storm event was done at day 285 (11/10), which is five days after the event. The cross-sectional area may already have decreased during the days after the storm, because the inlet wants to retain equilibrium. It can be concluded that the amount of profiles measured during the storm events is too small to describe the factors influencing the morphology in detail.

	period	average wave angle (degrees)
storm event 1	274,0-276,5	338,127
storm event 2	277,8-279,5	325,224

Table 6.1: average wave angle for both storm events.
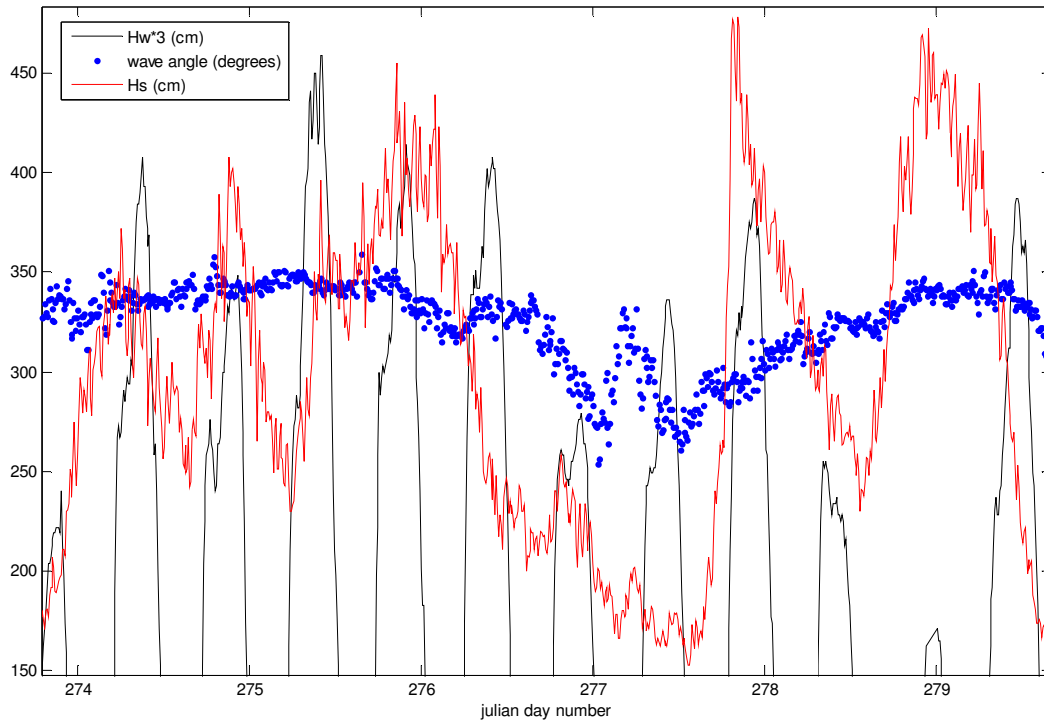
Figure 6.4: wave angle (degrees), offshore significant wave height Hs (cm) and water level above NAP in the channel (cm) plotted against time during the two storm periods.

The decrease of inlet cross section after the storm events is probably a response of the inlet to retain equilibrium. The storm events enlarged the cross section and the inlet became out of equilibrium (figure 1.4). Assuming a stable equilibrium before the storm events, the shear stresses after the storm become smaller than $\hat{\tau}_{eq}$. Not all sediment deposited in the inlet could be eroded by the tidal currents. The cross section reduces, until equilibrium is reached again. This effect can be seen when maximum velocities before and after the storm event are compared (figure 6.5). Maximum velocities after the storm conditions, both during the flood and ebb stage are slightly smaller than peak velocities before the storm conditions. Differences are however small.
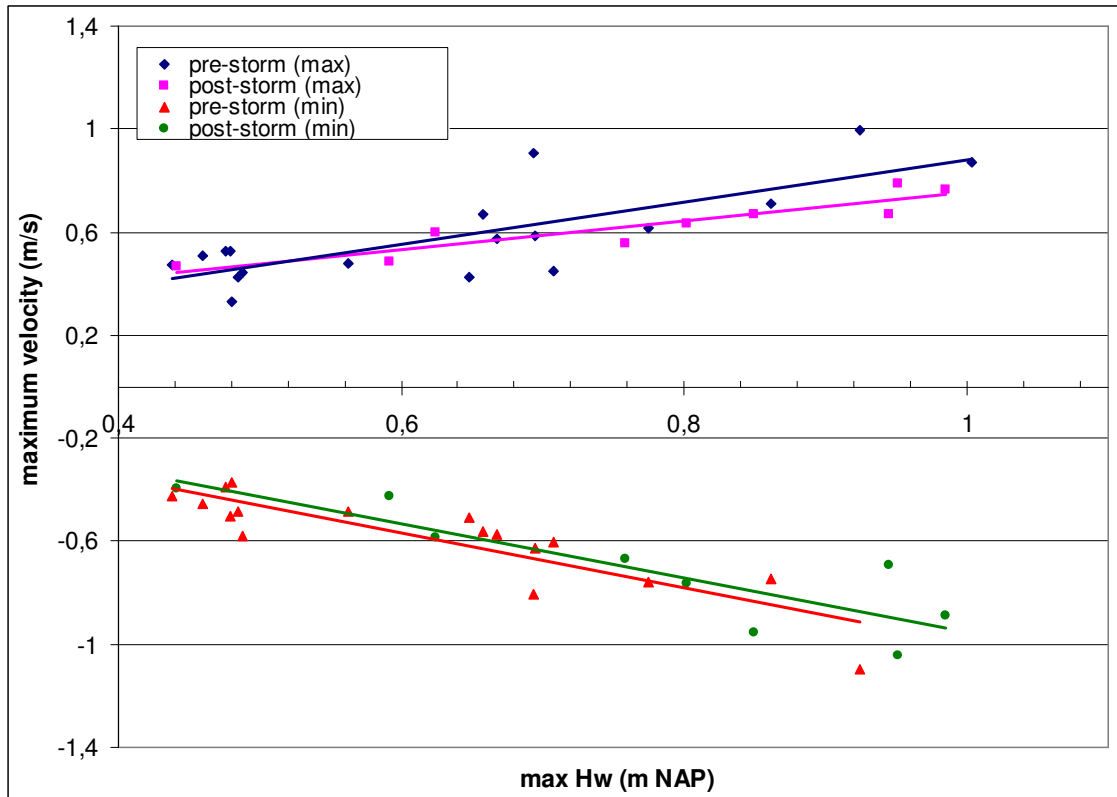
Figure 6.5: maximum water levels reached during all the tidal cycles of a period before the storm (day 262-275) and a period after the storm (day 285-291) plotted against maximum velocities reached during the associated tidal cycle (both maximum ebb- and flood-velocities). Ebb-velocities are negative. The figure also includes linear regression lines for both pre-storm and post-storm maximum velocities.

The cross-sectional area of the channel below 1.0 m +NAP increases from 59.7 m^2 (29/09) to 83.9 m^2 (02/10) and 80.2 m^2 (11/10). There is however a large difference between the channel section and the beach flat. Whereas the cross sectional area of the channel (between -0.9 m and 1.0 m) increases by a large amount (figure 6.3; lower section), cross sectional areas at a height of 1.2 m - 1.3 m are nearly equal before and after storm conditions. This indicates a decrease of the cross-sectional area between 1.0 m and 1.3 m. Accumulation must have occurred on the beach flat (see section 4.2.3; figure 4.9). The elevation of this flat increased by an average amount of 5.5 cm. This behaviour is probably related to the circulation pattern discussed in section 5.4.3. Whereas large amounts of water are imported over the beach flat during storm conditions, export is mainly confined to the channel. This favours the accumulation of sediment on the beach flat. Large amounts of sediment became available during the erosion of the beach near the shoreline. A landward retreat of the beach of 12-15 meters was observed (4.2.2). Part of this sediment is probably deposited on the beach flat. To conclude: sedimentation occurred on the beach flat west of the channel, but the main channel exports sediment during storm conditions.

Channel migration

A large channel migration was observed during storm conditions. Three probable mechanisms that play a role in this migration include the impact of waves, the circulation pattern in the mouth of De Slufter and a curvature induced circulation.

The impact of waves on channel migration is shown in figure 4.15. Smallest migration rates took place at profiles 1, 2 and 3. The channel is sheltered against incoming waves at these locations by the dune row southwest of De Slufter. Going in a seaward direction, migration rates increase with increasing influence of incoming waves and the longshore current. The sheltering effect caused by the beach flat decreases seaward. The orientation of the channel also changes in seaward direction. In the landward section of the channel (profiles 3-6) the direction of incidence of the waves is nearly perpendicular to the channel orientation. In the seaward section (profiles 7-13) the orientation becomes less oblique with respect to the waves. Therefore the wave impact will be smaller in the seaward section. However, because more waves reach the channel here and the sheltering effect by the beach flat is smaller in this area, migration rates are still largest in the most seaward section of the channel (profiles 9-13). The large channel migration rates near profile 13 are also closely related to the storm-induced change in the morphology of the beach and the strength of the longshore current.

As explained in section 4.2.2, the pre-storm beach morphology is characterized by a ridge and runnel system. This also influenced the flow pattern of the channel. Due to the presence of a spit-like ridge, the channel flows parallel to the shoreline in the north eastern direction for a distance of a few hundred metres before debouching into the sea (figure 6.6). Increased wave action during the storm-events destroyed the ridge-runnel morphology. The bar, forcing the channel to the northeast, was breached and finally disappeared. This significantly shortened the flow path of the channel to the sea, which now debouched into sea much further to the south. During calm weather after the storm-events, the pattern was restoring again. Between 09/10 and 13/10 the western channel side migrated 10 metres to the east. Driven by the longshore current, the ridge and runnel pattern is recovering and building out to the northeast.

Figure 6.6: panorama of the Slufter channel showing its flow path. The channel reaches the sea in the far right of the picture. The water flows nearly parallel to the coast line for a distance of several hundreds of metres.

The eastern channel side was subject to strong erosion during storm conditions. Cliffs were formed reaching heights up to 80 centimetres (figure 6.7). Maximum cliff heights were

observed just upstream of profile 10. They were formed due to the large velocities during ebb. As water flows rapidly seaward, the outer bend (the eastern channel side) is subject to strong erosion. Van der Vegt et al. (2009) however found no indication at the main frame that this eroded sediment is transported to the inner bend of the channel leading to channel migration. Whether such a cross-channel circulation exists in the channel at locations where the curvature is larger (for example near profiles 7 and 8; figure 2.1) is unclear, because no measurements were carried out here. Future measurements should reveal if this is the case and, if so, how much this process contributes to the total migration of the channel.

Figure 6.7: cliffs on 01/10 formed during the first storm-event at the eastern channel side.

Bank failure is an important mechanism in the formation of cliffs. Van den Berg et al. (2002) identifies two types of subaqueous slope failure: breach failures and liquefaction slope failures. Breaching occurs in dilatant sands, when pore volume expands under increased shear stresses. A negative pore pressure is created, resulting in a slowly retreating slope (retrogressive erosion). The negative pore pressure prevents large failures to take place as the particles are 'glued' together. Instead grain-by-grain erosion occurs, maintaining the steep character of the slope. Liquefaction slope failures generally occur with much more gentle slopes. They start to flow when the slope suddenly starts to behave like a viscous fluid. This is generally caused by an external trigger. These failures are characterized by an increase in pore pressure and a reduction in the angle of internal friction. Breaching seems to be an important process in De Slufter, because very steep slopes were observed at the eastern channel side.

A third mechanism that probably causes channel migration during storm conditions is the circulation pattern mentioned in section 5.4.3. Import during flood mainly occurs over the beach flat, while the water is exported through the channel during ebb. When the water level reaches 1.1 m +NAP, during spring tide or storm conditions, the amount of water stored on the beach flat starts to increase rapidly. The relative percentage of water stored on the beach flat compared to the percentage stored in the channel can be derived from the cross sectional area of the entire inlet of De Slufter. From a water level of approximately 1.35 m

+NAP and higher, a larger percentage of water is stored over the beach flat than in the channel (figure 6.8).
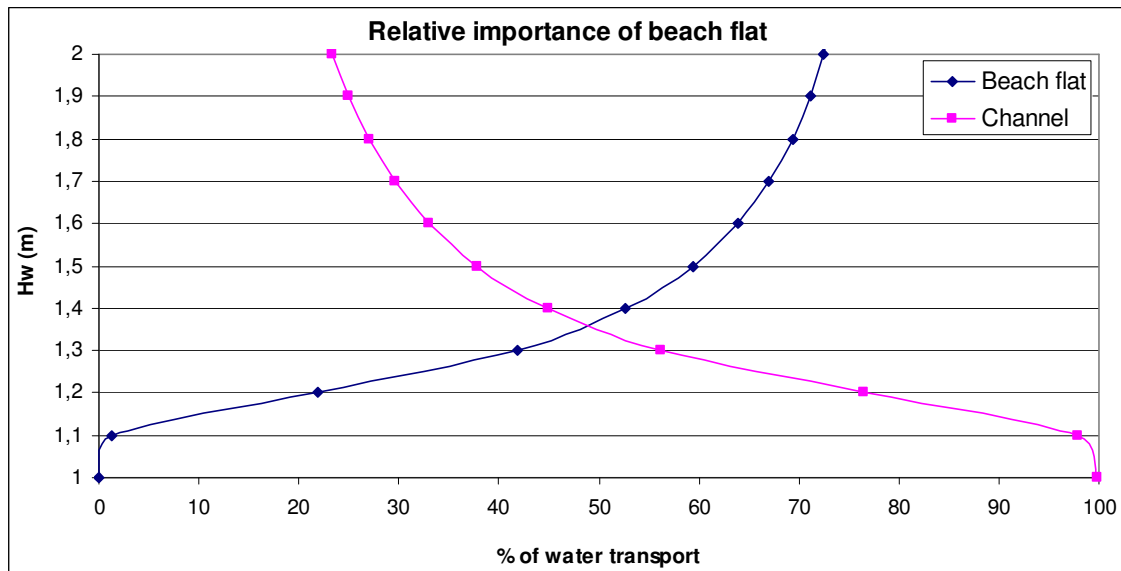
Figure 6.8: percentage of water transport plotted against the water level. Until a water level of 1.35 m +NAP most water is transported through the channel, while at the higher water levels, the beach flat becomes the most important area over which transport takes place.

Due to the circulation, sediment may be transported from the beach flat towards the channel. Deposition can occur here, especially near the western channel side. This may cause an eastward migration of the channel. To conclude: the combined effect of waves and the circulation pattern are probably the most important mechanisms causing channel migration. However, channel profiles should be monitored more often during storm events to get a more detailed understanding of the processes causing migration. This is however difficult due to the increased water levels.

6.3 Basin evolution

During normal conditions, no net bed load transport direction can be determined. Differences between ebb and flood transport are small. The net suspended load transport appears to be flood-directed. Storm events lead to a strongly ebb dominated bed load transport. When the evolution model of Boon and Byrne (1981) would be applicable to the situation of De Slufter, initial infilling occurred after the formation in 1858. This eventually led to the present situation with a very large surface area between 1.1 m and 1.5 m +NAP (nearly 50% of the total basin area). These areas were formed over the years, during spring tidal conditions and storm conditions and led to the present situation in which these areas result in ebb dominancy during storms and weak flood dominancy during normal conditions.

The system has decreased its flood dominant behaviour and has now developed some kind of dynamic equilibrium. During normal conditions, no significant sediment import or export occurs. During storms material is flushed out of the basin. When the beach flat is flooded during such a storm, sediment is deposited here. The bed height increases and during a following storm of the same magnitude, less surface area of the beach flat will be flooded. Eb-dominance has slightly decreased compared to the previous storm.

The model proposed by Boon and Byrne (1981) is however strongly idealized, and several processes are excluded from the model. These processes include for example: sea level rise, channel migration, the change of the cross sectional area (Stevenson et al., 1988), mechanisms driving the net transport flux of suspended material.

Measurements during the field campaign revealed no dominant net transport direction during a spring-neap tidal cycle and strong ebb dominance during storm conditions. It is unclear what the balance is on longer time scales of a year or even longer (decades). The storms observed during the field work were relatively moderate in relation to much larger storms. For example, during 2007 two of such large storms occurred, with maximum water levels reaching 2.51 m and 2.77 m +NAP respectively (compared to maximum water levels of 1.5-1.6 m for the storm-events during the field work). During these kinds of storms the response of the system will probably differ from the behaviour during moderate storms. The ratio of A_{xy}/A_c rapidly decreases again at water levels over 1.5 m NAP (figure 5.10). This will influence the value and occurrence of maximum ebb and flood velocities. Probably, dU_{max} will be smaller during more intense storm events, because the hypsometry-effect in De Slufter appears to be largest at water levels between 1.1 m and 1.5 m +NAP. Although the precise distribution between sediment import and export is unclear, the system appears to have reached an equilibrium situation. This equilibrium also follows when De Slufter is compared with other inlets in equilibrium (6.1).

Human interference is another important mechanism determining the behaviour of De Slufter. Without this interference De Slufter would be much more dynamic. The channel would erode the dunes north of the entrance and the channel would migrate northwards. As a result of dune erosion the entrance width increases, enhancing wave impact inside the basin. An unbound northward migration and increased meandering of the channel would extend the total length of the channel. This latter process increases friction, attenuating the tide. The transport capacity will reduce, resulting in a decreased cross-sectional area favouring flood dominance (Van de Kreeke, 1985). Probably the channel will create a short cut to the sea by itself, as happened for example in 1957 (figure 4.2). It is however largely uncertain what the entire impact of the several processes would be, when human interference would cease.

6.4 Tidal deformation

Accuracy of the DEM and TIN

During the transformation from the DEM to the TIN, from which basin volumes and wet surface areas were calculated, a z-tolerance of 10 cm was used, pointing to the maximum difference between the input DEM and the output TIN. A TIN consists of a large collection of small triangles. Near the depressions of the model this will result in an overestimation of the bed height, whereas the TIN will underestimate bed height at the crests of the model. This can be seen in a simplified comparison between a TIN model and a realistic morphology (figure 6.9). Due to the large amount of points taken in the TIN model of De Slufter this difference in height is not very large and the TIN seems a reliable approximation of reality. Comparing the TIN and the DGPS measurements for the dune to dune profile reveals a maximum difference of only 8 centimetres (figure 6.10).
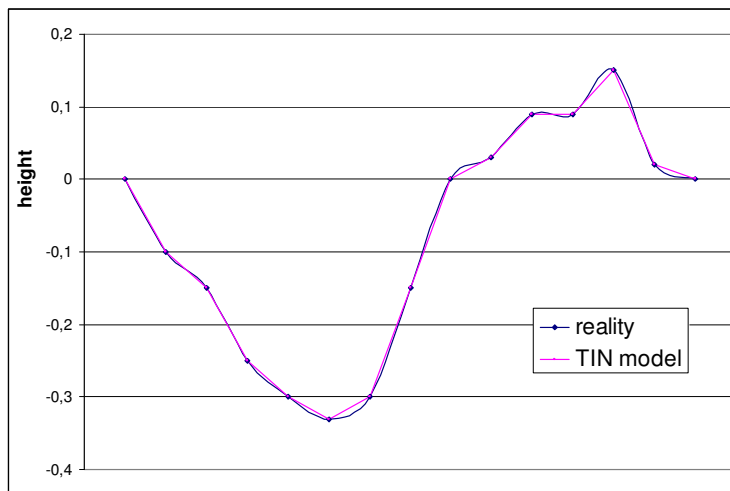

Figure 6.9: simplified example of a real morphology and a TIN model.
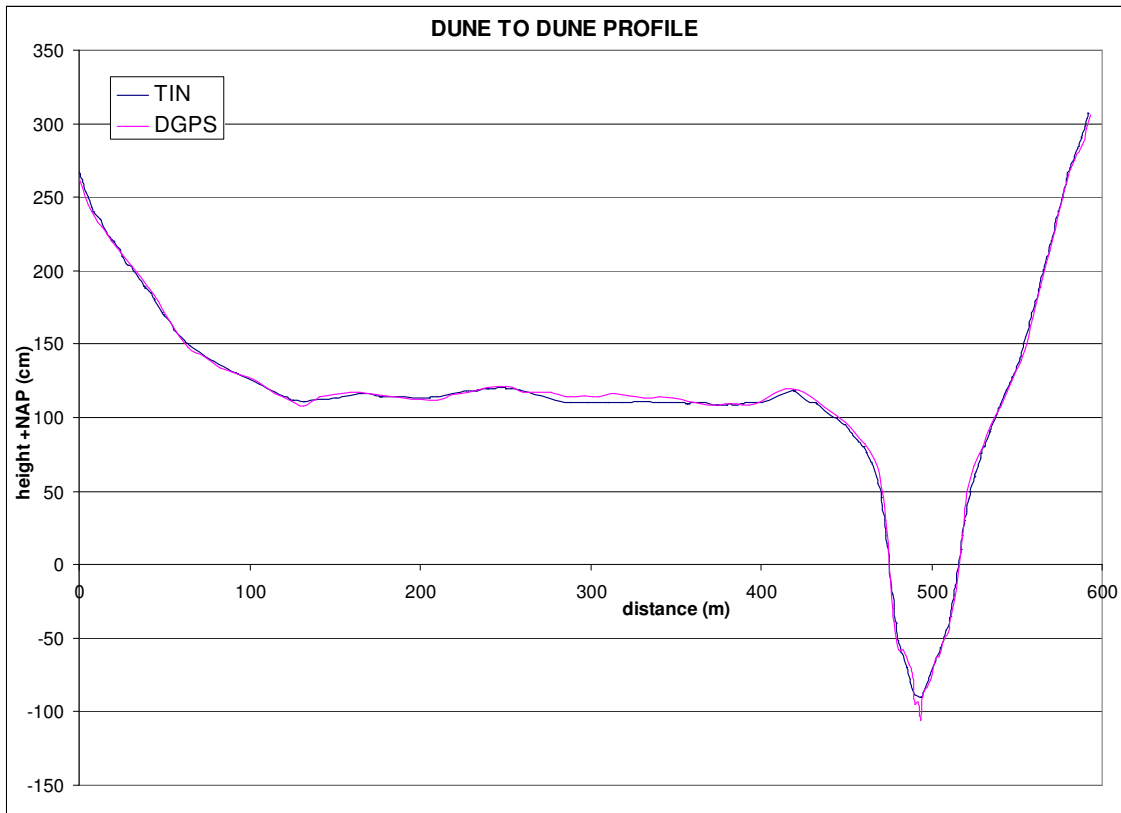
Figure 6.10: profiles for both the DGPS measurements and the TIN model, showing a large correspondence, with distance ranging from 0m at the dunes south of the Slufter mouth to 600m at at the dunes north of the mouth.

LiDAR is not able to measure correct bed heights underneath water surfaces. This results in an underestimation of the height at places where water was present during the LiDAR-measurements. Besides, there are several gaps in the data. These gaps probably appear at areas where water depths are too high to measure any bed height at all. Gaps were interpolated. A longitudinal profile of the channel bed near the transition of the DGPS data set to the AHN data set shows a large unrealistic increase in bed height. On average, the bed height measured by LiDAR increases between 0.4-0.6 metres compared to the DGPS measurements (figure 6.11). This will overestimate surface areas covered by water significantly, while volumes will be underestimated. The hypsometric curve will therefore deviate from reality at small water levels ranging up to approximately 0.4 m + NAP (depending on the water level present when LiDAR points were measured). Another large gap in the AHN data set appears due to an error in the overlap between the flight paths of the plane, further reducing the accuracy. Inaccuracies also arise, because the two data sets (AHN and DGPS) from which the DEM is created are not measured during the same year. The AHN originates from 2005, whereas DGPS measurements represent the situation in 2008. A merge does not reflect basin morphology entirely correct.

Figure 6.11: longitudinal profile of the deepest part of the channel of the DEM in metres. Transition from DGPS to LiDAR measurements occurs near point 80. LiDAR underestimates bed height by up to 60 cm.
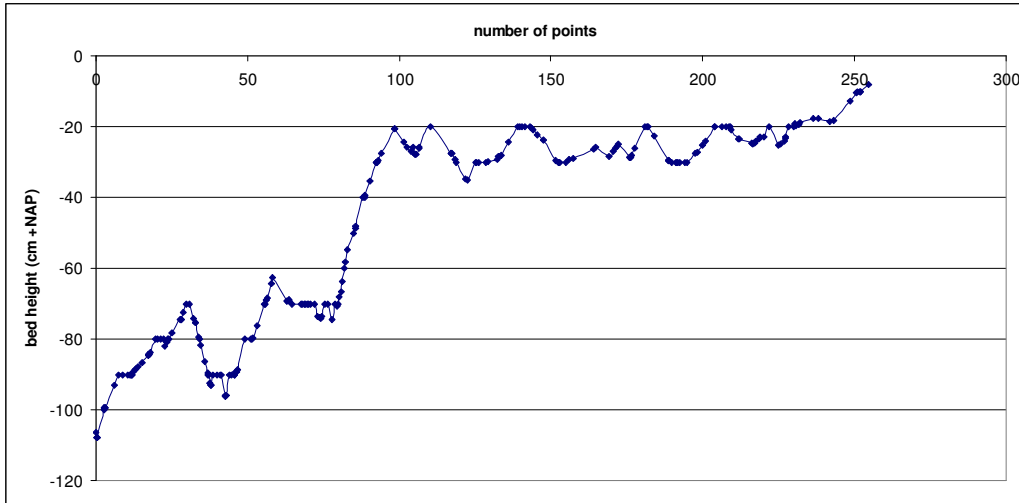
Accuracy of the hydrodynamical model

Deviations between results of the hydrodynamical model explained in paragraph 5.6 and measurements can be caused by several factors. Values for V_b and A_c, used in the model, are underestimated for small water levels (previous paragraph). This will result in modeled velocities, smaller than measurements. In most occasions velocities are however overestimated by the model. Partly these deviations are caused by the fact that measured velocities are often not representing the cross-sectionally averaged velocities. Assuming a logarithmic velocity profile, average velocities are found approximately at 0.4h. Because the measured velocities used in this analysis, come from an EMF meter at a height of 0.25 m above the bed, these values represent the average velocity when the water level is 0.625 m. When water levels are lower, measurements will overestimate the average velocity, because the EMF meter is located in the upper regions of the water column. In turn, with higher water levels the EMF meter is positioned below the area where average velocities are generally reached. Velocities will be underestimated. When peak velocities are reached during flood, water levels are, on average, smaller than during ebb. Measured flood velocities probably slightly overestimate the cross-sectionally averaged velocities, while ebb velocities would be slightly underestimated. As can be seen from figures 5.17 and 5.18, ebb velocities are predicted very well by the model. This can probably be explained by the fact that at the moment when maximum ebb velocities occur, the water levels are often close to the water level at which average velocities are expected (0.625 m). Figures 5.17 and 5.18 also indicate that peak flood velocities are underestimated with respect to modeled velocities. This is in contrast with what could be expected.

During storm conditions the opposite occurs. Flood velocities are modeled in a better way than ebb velocities, which are underestimated to a large degree. During storm

conditions, equation 5.3 is not valid for De Slufter. Water levels are not uniform throughout the basin. This is especially the case during the ebb phase. The circulation pattern mentioned in section 5.4.3 plays an important role in underestimating ebb velocities. During the flooding phase the imported water is spread over a larger cross-sectional area, because a large part enters the basin over the beach flat. Velocities can be modeled accurately. Export of this water during the ebb phase mainly occurs through the channel. Cross-sections will be significantly smaller, largely underestimating velocities.

Apart from these factors, deviations may arise due to the over-simplicity of the model. Processes like turbulence are not taken into account into the model.

7. Conclusions

This thesis gives an overview of the interactions between basin morphology and the hydrodynamics of De Slufter, and the implications for its long term evolution and stability. The final conclusions, in relation to the research questions, are presented below.

1) What is the morphology of De Slufter?

- The long-term morphological development of De Slufter is characterized by a cyclic pattern of channel migration in the Slufter mouth. In 3-7 years the channel migrates from its most southwestward location towards the northeast, strongly increasing its curvature during the cycle. At the end of the cycle the channel is relocated back to its initial position by man.

- Storm-induced (short-term) morphological development observed during the field work:
  - The coast line shows a landward retreat up to 15 meters.
  - An average accumulation of 5.5 cm was observed on the beach flat.
  - The seaward part of the channel (profiles 9-13) migrated, up to 10 meters at its most narrow location (profile 10) and the curvature of the channel slightly increased. The most seaward section of the channel (profiles 11-13) widened, became shallower and strongly migrated to the west.
  - Largest part of channel widened, increasing A_c up to 22.1% in the seaward section. This resulted in slightly smaller peak ebb- and flood velocities. During fair weather conditions afterwards A_c decreased again.
  - The circulation pattern observed during storm events - importing water and sediment over the beach flat and exporting it through the channel - combined with wave action and the longshore current is possibly the main mechanism driving channel migration. No indications were found pointing to a curvature induced circulation.

2) What is the influence of basin morphology on the hydrodynamics of De Slufter?

- Tidal deformation occurs when the tidal wave enters De Slufter. M_2- and M_4-amplitudes both decrease as does the M_4/M_2-ratio. While the tide is already asymmetric on the North Sea, further deformation occurs when the tidal wave enters the channel of De Slufter. Compared to the North Sea (D = -8.34%), ebb duration increases by 53.5 minutes   (D = -22.73%). $(2M_2-M_4)$ has an average value of 310°. This asymmetry is the

combined result of an external asymmetry, tidal truncation and a hypsometry effect:

- ○ Truncation: the tidal wave gets truncated when it propagates from the North Sea to the Slufter channel. Mean low water at sea (-0.89 m NAP) is much lower than the elevation of the channel bottom (-0.5 m NAP). Because the water depth in the channel never drops below 20 cm, a large gradient occurs between the channel and the North Sea. Because flow velocities during normal conditions are however small, differences between amounts of import and export of bed load are also small during a neap-spring tidal cycle. It appears that bed load transport is slightly dominant in the ebb direction, while suspended load appears to be dominant in the flood direction.

- ○ Hypsometry: due to the morphology of the basin there is a strong export of bed load during storm conditions. Nearly 50% of the surface area of De Slufter has an elevation between 1.1 m and 1.5 m +NAP. This has a large influence on flow velocities and net bed load transport directions during storm conditions. The flood phase is retarded when these flats get flooded, increasing flood duration and decreasing the ebb duration. While the beach flat plays an important role in the import of water during flood, export during ebb mainly occurs through the channel. Peak ebb velocities (~2 m/s) are twice as large as peak flood velocities (~1 m/s).

3) Based on a simple model, what will happen with the stability of De Slufter?

- Velocities were modeled using a simple hydrodynamical model. The simulations were compared with measurements. On a large scale the model is able to simulate velocities in a representative way, but due to several factors deviations may arise. Flood velocities are overestimated during normal conditions, while ebb velocities during storm conditions are underestimated. Factors resulting in deviations include measurements which do not measure average velocities and the over-simplicity of the model. Deviations during storm conditions are mainly caused by the fact that the water level is not uniform throughout the basin during storms.

- The fact that De Slufter exists for more than 150 years now in its present configuration, indicates an equilibrium situation. Several empirical relationships derived for stable inlets all over the world indicate that De Slufter is in equilibrium. These results however have to be analyzed with precaution because most relations are derived for larger inlet systems and human interference plays an important role by relocating the channel every 3-7 years.

8. Literature

Bagnold, R.A., 1966. An approach to the sediment transport problem from general physics. Geological Survey Professional Paper 422-I, U.S. Government Printing Office, Washington D.C., USA

Bailard, J.A., 1981. An energetics total load sediment transport model for a plane sloping beach. Journal of Geophysical Research 86, C11, p 10938-109954

Bailard, J.A., 1985. Simple models for surfzone sediment transport. Naval Civil Engineering Laboratory, Technical Note N 1740, Port Hueneme, CA.

Bayram, A., Larson, M., Miller, H.C., Kraus, N.C., 2001. Cross-shore distribution of longshore sediment transport: Comparison between predictive formulas and field measurements. Coastal Engineering 44, p 79–99

Boersema, M., 2004. Bekkenmorfologie en ebdominantie, De Slufter Texel. Msc Thesis Physical Geography, Utrecht University, 56 p

Boon, J.D., Byrne, R.J., 1981. On basin hypsometry and the morphodynamic response of coastal inlet systems. Marine Geology 40 (1981), p 27-48

Bruun, P., 1978. Stability of Tidal Inlets. Elsevier, Amsterdam. 506 p

Bruun, P., Gerritsen, F., 1960. Stability of Tidal Inlets. North-Holland, Amsterdam. 123 pp.

Doomen, M.C., 2003. Het Zwin, sedimenttransport in een klein zeegat. Msc Thesis Physical Geography, Utrecht University, 50 p

Dronkers, J, 1986. Tidal asymmetry and estuarine morphology. Netherlands Journal of Sea Research 20 (2/3) (1986), p 117-131

Dronkers J., 2005. Natural and human impacts on sedimentation in the Wadden Sea: an analysis of historical data. The Hague: Report National Institute for Coastal and Marine Management. 47 p

Durieux, M.X., 2005. De Stabiliteit van De Slufter op Texel. MSc Thesis Civil Engineering, Delft University, 91 p

Elias, E.P.L., Cleveringa, J., Buijsman, M.C., Roelvink, J.A. and Stive, M.J.F., 2006. Field and model data analysis of sand transport patterns in Texel Tidal inlet (the Netherlands). Coastal Engineering 53, p 505-529

Eysink, W.D., 1993. Impact of sea level rise on the morphology of the Wadden Sea in the scope of its ecological function. ISOS*2 Project, Phase 4. Delft Hydraulics

Escoffier, F.F., 1940. The Stability of tidal inlets. Shore and Beach 8 (4), p 111-114

Fagherazzi S., Hannion M., D'Odorico P., 2008. The Geomorphic Structure of Tidal Hydrodynamics in Salt Marsh Creeks. Water Resources Research 44, W02419

Friedrichs, C.T., Aubrey, D.G., 1988. Non-linear tidal distortion in shallow well-mixed estuaries: a synthesis. Estuarine, Coastal and Shelf Science 27 (1988), p 521-545

Gao, S., Collins, M., 1994a. Tidal inlet equilibrium in relation to cross-sectional area and sediment transport patterns. Estuarine, Coastal and Shelf Science 38 (1994), p 157–172

Gao, S., Collins, M., 1994b. Tidal inlet stability in response to hydrodynamic and sediment dynamic conditions. Coastal Engineering 23 (1994), p 61-80

Hayes, M.O., 1979. Barrier island morphology as a function of tidal and wave regime. In: S.P. Leatherman (Editor), Barrier Islands. Academic Press, New York, N.Y., p 1-27

Klein-Breteler, R., 2009. Wave-induced sediment transport at the small tidal inlet 'Slufter' of Texel, the Netherlands. Msc Thesis Physical Geography, Utrecht University, 104 p

Kramer, W.M., 2009. Sediment import and export in de Slufter under different tidal regimes. Msc Thesis Physical Geography, Utrecht University

Lam, N.T., Verhagen, H.J., van der Wegen, M., 2003. Hydrodynamic modeling of tidal inlets in Hue, Vietnam. COPEDEC VI (2003)

Lau, K.M., and H. Weng, 1995. Climate Signal Detection Using Wavelet Transform: How to Make a Time Series Sing. Bulletin of the American Meteorological Society 76, p 2391–2402

Lincoln, J.M., FitzGerald, D.M., 1988. Tidal distortions and flood tidal dominance at five small tidal inlets in southern Maine. Marine Geology 82 (1988), p 133-148

O'Brien, M.P., 1969. Equilibrium flow areas of inlets on sandy coasts. Journal of Waterways and Harbour Division, ASCE 95, p 43-52

Postma, H., 1954. Hydrography of the Dutch Wadden Sea. Archives Néerlandaises de Zoologie 10 (1954), p 405-511

Schoorl, H., 1999. De Convexe Kustboog: Texel - Vlieland - Terschelling

Speer P.E., Aubrey D.G., 1985. A study of non-linear propagation in shallow inlet/estuarine systems, Part II: Theory. Estuarine, Coastal and Shelf Science 21 (1985), p 207–224

Smith, N.P., 1979. Meteorological Forcing of Coastal Waters by the Inverse Barometer Effect. Estuaries and Coastal Marine Science 8, No 2, p 149-156

Stenvenson, J.C., Ward, L.G., Kearney, M.S., 1988. Sediment transport and trapping in marsh systems: implications of tidal flux studies. Marine Geology 80 (1988), p 37-59

Swart de, H.E., Zimmerman, J.T.F., 2009. Morphodynamics of tidal inlet systems. Annual Review of Fluid Mechanics

Torrence, C., and G.P. Compo, 1998. A Practical Guide to Wavelet Analysis. Bulletin of the American Meteorological Society 79, p 61–78

Townend, I.H., 2005. An examination of empirical stability relationships for UK estuaries. Journal of Coastal Research 21, p 1042–1053

Truitt, C., 1992. Tidal Inlet Dynamics. Sarasota Bay National Estuary Program MML, Project No. 310.419

Van de Kreeke, J., 1985. Stability of tidal inlets – Pass Cavallo, Texas. Estuarine, Coastal and Shelf Science 21 (1985), p 33-43

Van de Kreeke, J., 1990. Stability analysis of a two-inlet bay system. Coastal Engineering 14, p 481-497

Van de Kreeke, J., 1992. Stability of tidal inlet, Escoffier's Analysis. Division of Applied Marine Physics, Rosenstiel School of Marine and Atmospheric Science University of Miami

Van de Kreeke, J., 2006. An aggregate model for the adaptation of the morphology and sand bypassing after basin reduction of the Frisian Inlet, Coastal Engineering 53, p 255-263

Van de Kreeke, J., Robaczewska, K., 1993. Tide-induced residual transport of coarse sediment: application to the Ems Estuary. Netherlands Journal of Sea Research 31 (3), p 209-220

Van den Berg, J.H., van Gelder, A., and Mastbergen, D.R., 2002. The importance of breaching as a mechanism of subaqueous slope failure in fine sand. Sedimentology 49, 81–95

Van der Borg, M.J.H.M., van Dorsser, H.J., 1961. De Sluftermond op Texel. T.K.N.A.G. LXVIII, 57

Van der Vegt, M., Hoekstra, P., van Puijvelde, S.P., 2009. Channel migration in small tidal inlet. RCEM 2009

Van Goor, M.A., Stive, M.J.F., Wang, Z.B., Zitman, T.J., 2001. Influence of relative sea level rise on coastal inlets and tidal basins. Coastal Dynamics 2001, ASCE, Lund, Sweden

Van Straaten, L.M.J.U., Kuenen, P.H., 1957. Accumulation of fine grained sediments in the Dutch Wadden Sea. Geol. Mijnb. (N.S.) 19 (1957), p 329–354

Walton, T., 2002. Tidal Velocity Asymmetry at Inlets. ERDC/ CHL CHETN-IV-47. US Army Engineer Research and Development Center, Vicksburg.

Zuijderwijk, M., 2006. Cross-shore sediment transport and morphology of the Verdonken Zwarte Polder 'Slufter'. Msc Thesis Physical Geography, Utrecht University, 67 p

Appendix 1:

Date	Jul.	Main	Main	Beach Flat	Beach Flat
		Truc Vert	*frame 16*	*landward*	*seaward*
09-09-2008	253				
10-09-2008	254		11:00		
11-09-2008	255	11:00			
12-09-2008	256				
13-09-2008	257				
14-09-2008	258				
15-09-2008	259				
16-09-2008	260				
17-09-2008	261				
18-09-2008	262				
19-09-2008	263		12:00		
20-09-2008	264				
21-09-2008	265				
22-09-2008	266				
23-09-2008	267				
24-09-2008	268				
25-09-2008	269				
26-09-2008	270				
27-09-2008	271		15:00		
28-09-2008	272				
29-09-2008	273				
30-09-2008	274				
01-10-2008	275			16:00	18:00
02-10-2008	276				
03-10-2008	277			13:00/15:00	13:00
04-10-2008	278		16:00		22:30
05-10-2008	279				
06-10-2008	280	11:00/ 18:00		16:00	16:00
07-10-2008	281				
08-10-2008	282				
09-10-2008	283				
10-10-2008	284	8:30/ 11:00			
11-10-2008	285				
12-10-2008	286		13:30		
13-10-2008	287		13:30		
14-10-2008	288				
15-10-2008	289				
16-10-2008	290	17:00			
17-10-2008	291				

Appendix 1: overview of all hydrodynamical measurements done during the field work period indicated in blue, including date and Julian day number used in nearly all of the following graphs.